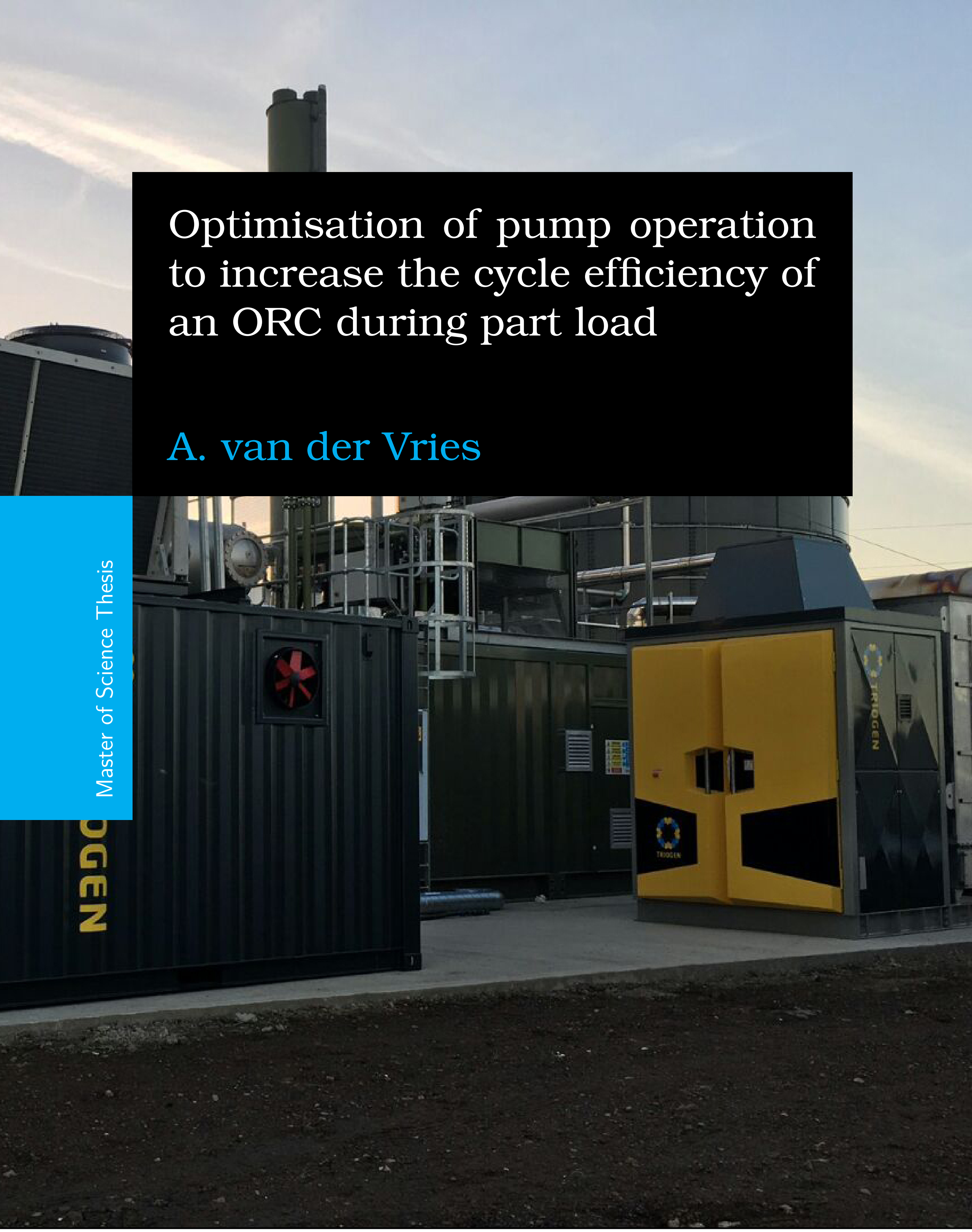

Optimisation of pump operation to increase the cycle efficiency of an ORC during part load

A. van der Vries

Master of Science Thesis

Energy, Flow and Process Technology

Optimisation of pump operation to increase the cycle efficiency of an ORC during part load

Master of Science Thesis

by A. van der Vries

in partial fulfillment of the requirements for the degree of Master of Science in Energy Technology at Delft University of Technology

to be defended publicly on Monday October 27, 2021 at 02:00 PM.

Student number:	4601580	
Project duration:	January 5th, 2021 – September 27th, 2021	
Thesis committee:	Dr. Ir. R. Pecnik,	TU Delft
	Prof. Dr. Ir. S.A. Klein,	TU Delft
	Ir. S.S.H.J. Smit,	TU Delft

Cover image from [1]. An electronic version of this thesis is available at

http://repository.tudelft.nl/.

Faculty of Mechanical, Maritime and Materials Engineering (3mE) · Delft University of Technology

---

[1] http://www.triogen.nl/references/reference-overview

The work in this thesis is based on the system of Triogen. Their time and efforts were a great help and their contributions are highly appreciated.

Copyright © Energy, Flow and Process Technology (EFPT)
All rights reserved.

Abstract

The global warming and increase in energy use demands the industry to come up with ideas to lower the CO_2 production and save valuable energy. Organic Rankine cycles have a great potential as low grade heat can be converted into electrical energy. In the last ten years, research in this particular field has increased together with the amount of installed systems. Triogen is a company which does a lot of research on how to increase the power output of their ORC systems. Their product involves a radial inflow cantilever turbine connected to a single shaft to the generator and the main pump which makes the system quite unique. Because of the fluctuating heat input the system scarcely runs on its design condition so research has to be done to ensure the turbine efficiency is as high as possible to extract as much power out of the heat source as possible. This study investigates whether the pump strategy can be modified in order to increase the system power output for part load situation. By means of elaborate turbine computational fluid dynamics (CFD) simulations, an optimal rotational speed op $n = 475\,\mathrm{Hz}$ is found for all turbine inlet pressures. A simple cycle model is made in MICROSOFT EXCEL in order to compute the increased power output, given the optimal rotational speed. The most cost effective and straight forward way to implement the fixed rotational speed in the system, a throttle valve is chosen. The amount of extra power gained using the optimal rotational speed is $\approx 7\,\mathrm{kW}$, which is an increase of 8%. For evaporator heat inputs higher than 900 kW, the operation with throttle valve is no longer beneficial and the operation on design condition is favoured.

Glossary

List of Acronyms

TU Delft	Delft University of Technology
ORC	Organic Rankine cycle
ICE	Internal combustion engine
OTEC	Ocean thermal energy conversion
CFD	Computational fluid dynamics
sCO2	Supercritical CO_2
WHR	Waste heat recovery
NPSHa	Net positive suction head available
BWR	Back work ratio
CHP	Combined heat and power plant
HTG	High-speed turbo generator
RANS	Reynolds averaged Navier Stokes
PI	Proportional and Integrating
NS	Navier Stokes
VBA	Visual basic for applications
VSD	Variable speed drive
PC	Pressure controller

List of Symbols

Greek symbols

α	Inlet angle
β	Outlet angle
Δ	Difference
η	Efficiency
γ	Heat capacity ratio
Λ	Degree of reaction
μ	Dynamic viscosity

ν	Kinetic viscosity
ω	Angular velocity
ϕ	Flow coefficient
ψ	Pressure coefficient
ρ	Density
τ	Shear stress

Latin symbols

$\dot{m}$	Mass flow
$\mathcal{A}$	Area
$\mathcal{H}$	Height
$\mathcal{O}$	Order of truncation error
$\mathcal{Q}$	Volumetric flow
$\mathcal{R}$	Proportion of variance
$\mathcal{W}$	Width
A	Constant
a	Speed of sound
B	Constant
c	Specific heat
D	Outlet diameter
d	Inlet diameter
E	Energy
h	Enthalpy
i	Count variable
K	Constant
M	Imbalance
N	Number of timesteps
n	Rotational speed
P	Power
Q	Heat
q	Heat transfer per unit mass
R	Residual
r	Radius
S	Absolute entropy
s	Specific entropy
T	Temperature

t	Time
U	Speed
u	Specific internal energy
V	Speed
v	Specific volume
W	Work
w	Relative velocity vector
x	Horizontal location variable
y	Vertical location variable
z	Dependent variable in depth direction
C	Velocity

Subscripts

θ	Tangential component
i	Count variable
p	At constant pressure
s	Entropy kept constant
0	Initial value
1	Inlet
2	Outlet
cold	Cold side of the heat exchanger
cond	Condenser
crit	critical
d	Diffuser
des	Design
evap	Evaporator
fg	Flue gasses
fluid	Part of the pump energy which is net added to the fluid
fric	Friction part
hot	Hot side of the heat exchanger
loss	Outflow losses
model	Associated to the simulation model
mp	Main pump
new	Value for new timestep
nozzle	At the nozzle
old	Value for old timestep

overh	Overheating
pf	pre-feed pump
r	Radial
rec	Cold side of the recuperator
ref	Reference value
rel	Relative
RMS	Root mean square
rot	Rotor
rp	REFPROP
sat	At saturation conditions
stag	Stagnation
stage	Over the stage
stat	Static
t	Turbine
th	Throttle
tip	Tip of the rotor
tol	Toluene
tot	total
ts	Total to static
tt	Total to total
underc	Undercooling
wf	Working fluid

Superscripts

$+$	Addition to indicate the dimensionless wall distance
$'$	Velocity part of the energy into the fluid

Vectors

$\boldsymbol{e}$	Unit vector
$\boldsymbol{u}$	Flow velocity vector

Non dimensional numbers

Ma	Mach number
Re	Reynolds number

Constants

$\bar{R}$	Universal gas constant	$8.314\,\mathrm{J \cdot K^{-1} \cdot mol^{-1}}$
g	Gravitational constant	$9.81\,\mathrm{m \cdot s^{-2}}$

Contents

List of Figures

List of Tables

Preface

It was such a pleasure to be involved in the world of ORCs and to be part of the team of Triogen for a short time. I have learned a lot during the graduation internship when it comes to planning, project work, meetings and feedback. The energy part of mechanical engineering have always had my interest during both my bachelors study at the Hanzehogeschool and my masters study at the Delft University of Technology (TU Delft). I am looking forward to begin my life as process engineer in this discipline.

I would greatly thank Stephan Smit for his enormous amount of patience, he paved the road of this thesis and without him I would have been lost many times. Also, I want to thank Quirijn, my fellow Groninger, who was a great source of information. An engineer who is also passionate about education, a great example for me and many others. In the end I would thank Rene for making this project possible and Jos van Buijtenen for his critical view on my work.

Delft, University of Technology
27/10/2021

A. van der Vries

Chapter 1

Introduction

Although the COVID-19 crisis caused a small decrease in energy consumption, the energy demand is growing in time [13]. Furthermore, the fossil fuel source depletion asks us for ways to use fossil fuel based cycles more efficient [33]. Also CO_2 emissions leading to global warming, demands us to change the way electricity is produced [45].

Until recent years, a large part of the heat used in industrial processes is rejected in the medium temperature range, as described by Pili et al. [43]. In order to both decrease energy costs and reduce CO_2 emissions, systems such as organic Rankine cycles (ORCs) can play a large role in waste heat recovery (WHR), creating electrical energy from ”waste” heat, which would have been thrown out in the environment before. That is why more efficient ORCs could lead to both a cleaner world and less depletion of fossil fuels.

In this chapter more information on the ORC is given: what is the history, what does the cycle look like, what are the advantages, in which field can they be used, how is the market on ORCs and what are currently hot research topics. Thereafter the reference cycle, which is applied in this study, is explained: the history of the company, information on their system, why their system is unique relative to other ORCs and which studies are already done on the cycle. The topics which are involved in this research are discussed, such as pump type and part load operation.

For the cycle of Triogen, the rotational speed of part load operation is not optimised to maximise the power output of the system. The research question *”How can the pump strategy be optimised in order to increase cycle efficiency of part load operation?”* will be answered throughout this thesis and is explained in more detailed in section 1-2. This section also explains the method.

1-1 Literature study

As discussed above, an ORC can help to achieve climate goals faster. In the first section, the ORC is thoroughly discussed, together with a market analysis and the current research opportunities. In the second section the company Triogen and their product will be introduced. It then explains the research done on their system and then shows the promising optimisation.

1-1-1 Organic Rankine Cycle

The Rankine cycle was invented in 1859 by William J.M. Rankine [2]. This system can be used to convert heat into mechanical energy. The cycle consists of a pump, an evaporator, a condenser and an expander. The working fluid is isentropically pumped to the evaporator where it is vaporised isobarically. An overview of this simplistic system is shown in figure 1-1. To extract energy from the system, a generator can be connected to the turbine. The cycle is similar to the Carnot cycle except for the fact that the evaporation and condensation happens isobaric instead of isothermally.

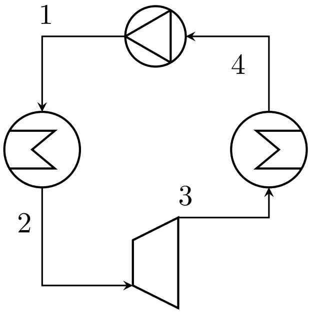

Figure 1-1: Simplistic overview of the Rankine cycle

The system can deliver net work when the working fluid undergoes pressure and temperature changes. This can be seen in the $\log(p) - h$ diagram as displayed in figure 1-2. The working fluid is pressurised from point four to one and expanded from point two to three. It is clear that the enthalpy difference between point four and one is smaller than the enthalpy difference between point two and three. If it is assumed that, as the mass flow remains the same, energy is extracted from the cycle and can be used to drive a generator. The cycle is thermodynamically possible because there is both energy consumed from point one to two and energy extracted from point three to four.

The advantages of the Rankine cycle over other cycles are that they are simple, easy to maintenance and have a high reliability, as mentioned by Dong et al. [17].

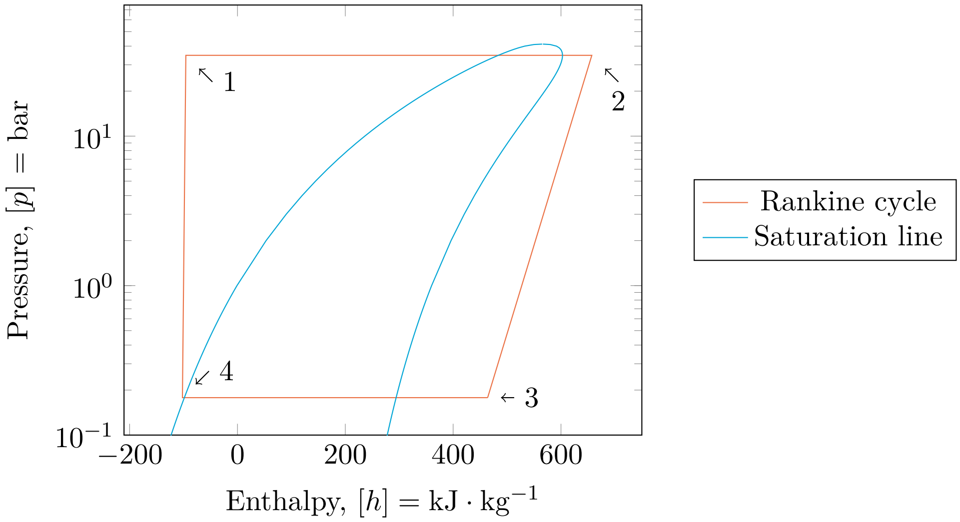

Figure 1-2: $\log(p)$ - h diagram of an ORC

The particular parts of the Rankine cycle are listed below.

System components

- The *pump* in the ORC system (path one to four in figure 1-1) pressurises the working fluid from condensation pressure to the evaporation pressure. Various pumps can be found in Rankine systems, Landelle et al. [29] grouped them as reciprocating (diaphragm, piston and plunger pumps), rotary (gear, rotary piston and rotary vane pumps) and centrifugal (mono or multistage pumps).
- In the *evaporator* (path one to two in figure 1-1) the working fluid is evaporated and superheated with the help of a hot external source. The superheating prevents the turbine from damage when droplets of working fluid would hit the turbine blades.
- The *expander* (two to three in figure 1-1) is a critical component in the Rankine cycle, it extracts energy from the working fluid and passes it on to the main shaft which in turn drives the pump. As found out by Imran et al. [25], a fair amount of research is done on expander design. Most ORC on the market uses axial or radial turbines with one stage but also other expanders such as scroll expanders, screw expanders, Tesla turbines and rotary vane expanders are used [12].
- In the *condenser* (path three to four in figure 1-1) the working fluid is condensed and undercooled. This undercooling prevents the pump from cavitation, which is also discussed in section 2-7.

Organic Rankine cycle

To increase the exergetic efficiency of the Rankine cycle, the temperature over the heat exchangers needs to be as small as possible. Different working fluids have different saturation temperatures at different pressures. A way to decrease the temperature differences over heat exchangers, is to find a certain fluid with a saturation temperature which is similar to the heat source temperature. It is found that organic molecules are particularly good for this purpose, and are extensively used as working fluid in Rankine cycles. In this case the system is called an organic Rankine cycle (ORC).

The first apparatus which used an ether or alcohol in a Rankine cycle, was invented by Thomas Howard in 1825-1826 [26]. Influenced by his idea, Ofeldt and Esher started building naphta engines. D'Amelio built the first modern ORC which used monochloroethane. This system was heated by solar power and used a single stage impulse turbine. In the 1960's Tabor and Bronicki started a leading study on potential working fluids which pointed out that the use of complex freons is more beneficial. They ignited the start of the use of the regenerative saturated cycle configuration which is still very commonly applied today.

Working fluids

The advantages of an organic compound as working fluid is that it enables one to apply the cycle on a large heat source temperature range [12]. The application of a specific working fluid can also decrease the exergy destruction by choosing a working fluid that has a vaporisation temperature (for a certain pressure) similar to the heat source (also described above). The selection of working fluid depends strongly on the temperature range of the hot source. Except for some materials which have a too high or low critical temperature, a lot of potentially working fluids are available according to Bao and Zhao [5]. Special attention has to be given to the thermal stability of the material. Working fluids which are commonly used come from the groups hydroflurocarbons(R-134a) and hydrochloroflurocarbons(R-123) [29]. A novel field of research is using supercritical CO_2 (sCO2) as working fluid regarding the high global warming potential of large organic molecules relative to CO_2 [3]. In some cases the working fluid can also be applied as lubrication or cooling of the shaft [55].

Application

The heat sources used for ORC can be divided into four groups: heat recovery, geothermal, biomass and solar, according to Tartière and Astolfi [52]. A promising application is ocean thermal energy conversion (OTEC) but this is in a very early stage of development [12]. It is a technology which generates electricity from the temperature differences between the surface and the bottom of the ocean.

Most of the heat input for installed capacity comes from geothermal wells. The groups biomass and heat recovery are almost equal in size and solar is the smallest source among those four. The main source of ”waste” heat recovery is Diesel or gas engines and turbines, which cover 65 % of the total installed capacity. The second largest market on waste heat recovery is waste to energy with a percentage of 8.8. Third comes the metal industry with 7.5 % On the fourth place the cement and lime industry which covers 6.6 %. Some smaller industry parts cover the rest. This application division is shown in figure 1-3.

Market growth

After the research carried out by Tabor and Bronicki, the companies ORMAT (1964) and Turboden (1970) started the design of several prototypes and are still one of the largest players on the market. ORMAT has the largest share, Turboden comes second. Other large companies active in the ORC systems market are Atlas Copco, Exergy, GE Energy and GE oil and gas, Triogen and GMK. A total overview from 2016 is shown in table 1-1, adapted from Tartière and Astolfi [52]. According to Tartière and Astolfi [52] the installed capacity increased very rapidly over the past twenty years, which makes the market very competitive.

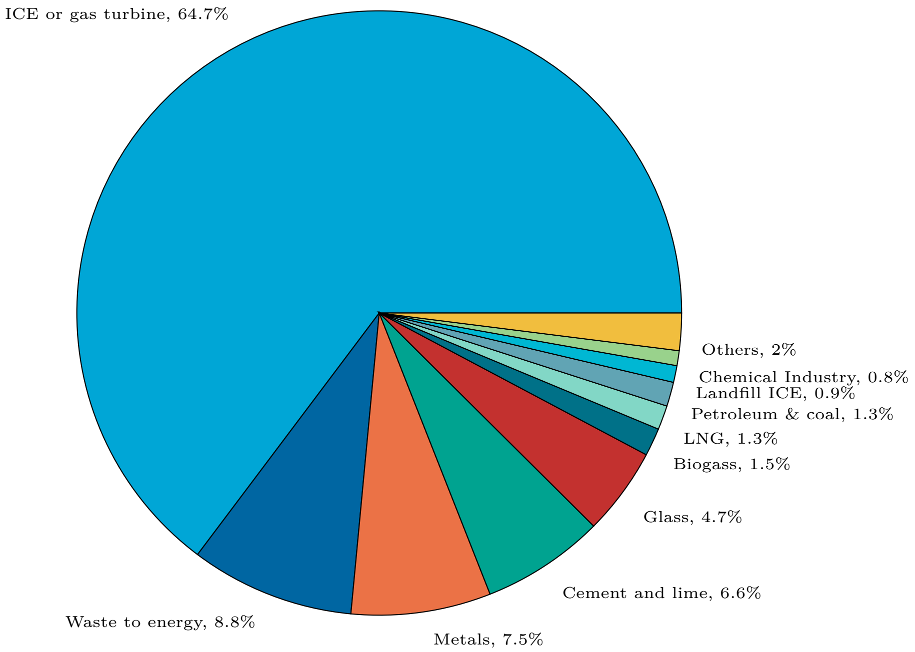

Figure 1-3: Application division of heat source group "heat recovery" according to Tartière and Astolfi [52].

Still a lot of projects are in construction, which increases the installed capacity even further in the coming years.

Manufacturer	ORC units	Total MW	Manufacturer	ORC units	Total MW	Manufacturer	ORC units	Total MW
ABB	2	3.8	Enogia	11	0.26	Orcan	16	0.3
Adoratec	23	16.4	Enreco	1	0.15	ORMAT	1102	1701
BEP - E-rational	20	3.6	Exergy	34	300	Rank	5	0.07
Calnetix / CETY	50	6.3	General Electric	6	101	TAS	17	143
DürrCyplan	6	1.2	GEM	18	5.3	TMEIC	1	1
Electratherm	55	3.14	gT - Energy Tech	2	0.7	Triogen	37	5.2
Enerbasque	3	0.13	Johnson Control	1	1.8	Turboden	267	363
Enertime	2	1.6	Kaishan	40	27.2	UTC Power	10	2.8
Enex	1	9.3	Opcon	3	2.0	Zuccato	2.1	1.7

Table 1-1: List with all companies which delivered commercial ORC units, adapted from [52]. Data from before Dec 31th, 2016

Research in this field

The amount of research on organic Rankine cycles has increased rapidly in the past 12 years according to Imran et al. [25]. Some hot research topics with examples are given below.

Research on application

The main focus in research is on the (domestic) application of the ORC. As already mentioned above, *geothermal* wells are one of the main heat sources for ORCs, so quite some research has been done on geothermal applications. In the article of Serafino et al. [49] a robust design optimisation is done in order to find the most efficient geothermal fed ORC configuration. The optimal design outperformed the one found with the standard deterministic approach. The expected power output increased with 1.5 % while the standard deviation is reduced by 8.5 %. A novel research field in the application of organic Rankine cycles is the usage of organic Rankine cycles in *(heavy) trucks* and light duty engines. In the study of Rijpkema et al. [47], an ORC is applied to improve the total efficiency of a car. The evaporator is placed at the exhaust pipe in an experimental setup. Control strategies were developed and a fuel consumption reduction of 5 % is found. A great number of articles cover ORC systems connected to a *biomass heat input*. For example, the study of Świerzewski and Kalina [65] focuses on the techno-economic optimisation of a biomass-fired cogeneration plant by means of an ORC. This study covers site-specific technical, economic, ecological and legal constraints. Thermal energy storage is taken into account to provide flexibility to the combined heat and power plant (CHP) system. The study reveals that the economic optima are relatively flat and the range of ORC unit size for this optimum is wide. A smaller amount of studies is about *solar powered ORC systems*. An article about an exergetic and economic analysis of a solar driven ORC is written by Roumpedakis et al. [48]. It describes a design optimisation and a performance assessment of a small-scale, low temperature solar driven ORC for usage in South-East Mediterranean. This included multiple scenarios with different working fluids, installation sites and solar collector types. The method used is a multi-objective genetic algorithm to optimise the payback period and the mean exergy efficiency.

The subject of most studies on component level is the expander in ORC. Research has been done on various types.

Research on expanders

The performance of a *rotary vane expander* is researched by Naseri et al. [37] in combination with a variety of working fluids. The results show the potential of revolving vane expanders for a small scale ORC. The characteristics of the expander at different operating conditions are observed, pointing out that the design is suitable for small scale units. An example of an article about a *Tesla turbine* is that of Talluri et al. [51], where a design approach is presented, which is applied to various working fluids. Three important geometric parameters were identified and their effect on the performance is analysed. It uses a 2-D code for viscous flow solution to measure the performance of the presented geometry of the turbine. Ultimately an efficiency higher than 60% is achieved. A *free piston linear expander* is modelled by Ng et al. [38] by means of the usage on a sea-going ship. A dynamic simulation with SIEMENS SIMCENTER AMESIM is used for the design and optimisation process. Results show that the expander is suitable for stable electricity generation. On the other hand, they found that the efficiency is low, for which the design might have to be improved. With MATLAB , a study is carried out to look at design operation and off-design operation of eight different *axial turbines* to eventually find efficiency correlations [44]. The correlations are tested on a benchmark case showing a coefficient of determination not lower than 90 %. Research on the preliminary design of a *radial inflow turbine*, by Meroni et al. [35] focused mainly on performance and manufacturability. A multidisciplinary approach is used to come up with a preliminary design. A mean-line model is coupled to a model for the generation of a preliminary 3-D turbine geometry. The results show that a trade-off can be made between turbine performance and manufacturability, proving that the manufacturability indicator improved to 14 % to 15 %

with the same efficiency. The way how the paper described manufacturability is by means of the design and how difficult it is to machine the wheel to the preferred design.

Research on part load operation

As described above, most ORCs uses heat sources which are fluctuating in time. Therefore special attention in research goes to part load or off-design operation of ORCs. Below are a couple of studies listed. By Wang et al. [59], four ORCs were studied in terms of the effects of evaporating pressure, condensing condition, working fluid and system architecture. This article takes considers the dynamics of the pump and expander are much faster than that of the heat exchangers. Quite some details of the evaporator and condenser designs are taken into account. The research heavily puts the emphasis on the thermal performance. The article by Petrollese et al. [42] studied the usage of an ORC connected to a solar field and a thermal storage system. Also a photovoltaic system is taken into account. The solar energy input does provide a fluctuating energy input upon the storage system and the ORC. Both optimisation of the ORC performance and optimisation of matching the delivery periods of the photovoltaic system and the ORC are studied. The study of Kalina et al. [27] simulated a biomass fired ORC by means of a mathematical model to predict the output when operated in part load. The ORC applied is a Turboden T6 of 606 kW. The simulation software used is EBSILON PROFESSIONAL . By Pili et al. [43], WHR of fluctuating industrial sources were used for powering an ORC. Different options were investigated to make a trade-off between reduced environmental impact and investment costs for WHR. The configurations were simulated using MATLAB and EBSILON PROFESSIONAL .

Research on pump design

Just quite a small amount of the studies covers pump design in ORCs [41].

Most studies on pumps in ORCs write about *diaphragm pumps*, which work similar to a leakage free reciprocating pump [32]. With a small test rig and varying working fluids, the isentropic efficiencies of a diaphragm pump were investigated by Xu et al. [62]. The outcome of this study is that the pressure difference and the volumetric flow have a large influence on the isentropic efficiency of the pump. D'Amico et al. [14] presents a semi-empirical model of a diagraphm pump integrated into an ORC experimental unit. In this paper, the mass flow rate trapped into the pump is used to compute pump characteristics and identify incipient cavitation. The study of Li et al. [32] studies the cavitation behaviour of a diaphragm pump based on experimental results and a 1-D model. The study by Yang et al. [63] focused on an experimental setup of a diaphragm pump and a performance analysis. They reached an efficiency of 88.3%, but because of the back work ratio (BWR) of 0.93, the power consumed by the pump is not negligible.

In a study of Cavazzini et al. [11] about a *multistage centrifugal pump*, an experimental setup with various working fluid is compared with computational fluid dynamics (CFD) computations which are rendered by ANSYS CFX . The paper highlights the needs of the general framework of the similarity theory in order to predict pump performance with fluids different from water. The study of Wu et al. [61] measured characteristic data such as temperature, pressure and flow rate in an experimental setup with a multistage centrifugal pump. A performance curve, the power output and the net positive suction head available (NPSHa) were studied. One of the outcomes is that the rotational speed has a significant influence on the NPSHa. Research by Meng et al. [34] focused on an experimental setup of a multistage centrifugal pump, considering the key parameters of the pump on the ORC, such as BWR, thermal efficiency of the ORC and specific work of the pump. It points out that pumping power should not be neglected for small scale ORC systems. Also the overall pump efficiency is investigated. By Yang et al. [64], an experimental setup is used to investigate the influence of the performance of the multistage centrifugal pump by the ORC. Amongst others, the mass flow rate, the outlet pressure, the mechanical efficiency, the rotational speed and the electric power consumption were taken into account.

By Borsukiewicz-Gozdur [9] *pumping work* is analysed of a list of 18 different working fluids. The study looked for a correlation between thermo-physical properties of the working fluid, specific work and power of the cycle. One of the results is that working fluids with relatively low critical temperature have a greater cycle pressure range for the specified cycle temperature range than those with higher critical temperatures. By Wang et al. [58], a *plunger pump* and a centrifugal pump were compared on experimental basis. The study concluded that the centrifugal pump has a higher mass flow rate and isentropic efficiency but also consumes more power. Richardson [46] looked at *thermofluid feed pumps*, a technology which is based on heat rather than mechanical or electrical power. This has some advantages such as low-cost and low-maintenance. A thermodynamic model is then presented and it is pointed out that this type of pump has potential for ORCs operating below a temperature of 100 °C. Lei et al. [30] investigated the application on small scale ORCs of a *high pressure pitot tube pump*, also called Roto-Jet. An experimental setup is used to investigate system parameters such as efficiency, ORC efficiency and the BWR for different rotational speeds. Also research is done on a small *gearpump* in order to fit into a truck design [1]. A test rig is used and pointed out that leakage paths are critical to maintain a good volumetric efficiency. The gearpump is found to be a good candidate for ORC in heavy trucks.

1-1-2 Triogen

Broad background information on ORC systems is given above, this study now focuses on the Triogen system. This system works similar to the simple ORC discussed above, the working fluid is pressurised in the pre-feed pump, the working is further pressurised in the main pump. The working fluid is preheated in the recuperator, evaporated in the evaporator, then expanded in the turbine. After the turbine, the working fluid is cooled down by the recuperator and condensated in the condenser. Between the condenser and the pre-feed pump a buffer tank is placed. An overview of the system is shown in figure 1-4.

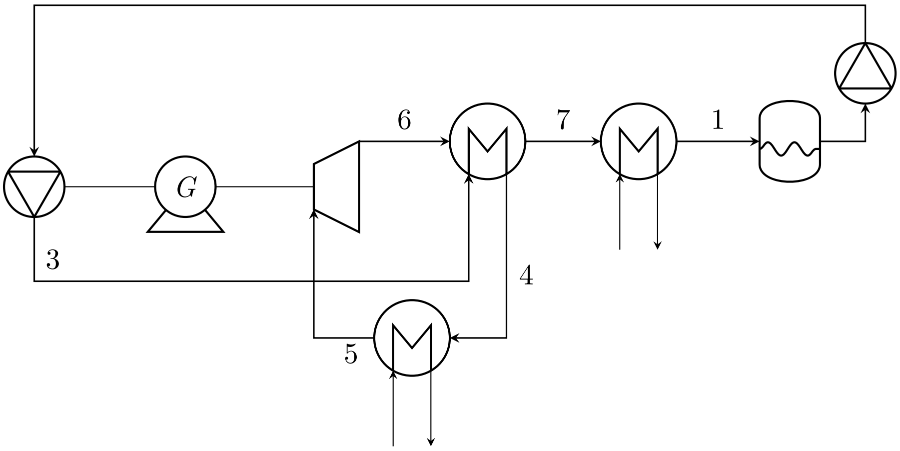

Figure 1-4: Adapted from [19] and [56]

Triogen produces ORC systems which provide 90 kW to 170 kW electric power. This system is able to ”boost” an industrial engine in the range of 1 MW to 2 MW with about 10%. Over 40 systems were sold worldwide [19]. The system can be easily shipped because of the system, without the hot and cold source equipment, is a sea container sized package. The components of the system are purchased from external companies and the machining of parts, which are designed by Triogen, is done by a third party. The system is assembled in their assembly hall near their office in Goor, a small city in the east of the Netherlands.

Triogen is found in 2001 by Delft University of Technology (TU Delft) professor Jos van Buijtenen [15] and they started developing their ORC systems from 2002 onwards [19] based on a concept from Lappeenranta University of Technology, Finland. Triogen already did a lot of research on their system, which is described later on in this subsection. It first explains how the Triogen system differs from the standard Rankine cycle mentioned earlier.

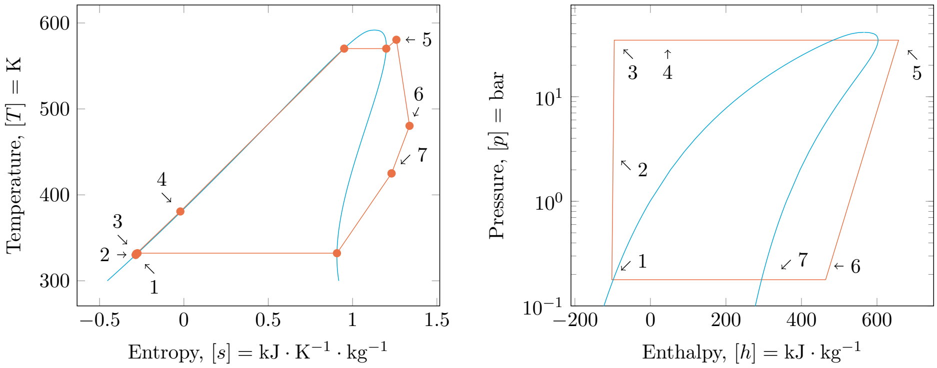

(a) $T - s$ diagram

(b) $\log{(p)} - h$ diagram

Figure 1-5: $T - s$ diagram and $\log{(p)} - h$ diagram of the Triogen cycle, constructed with data from Eppinga et al. [19] and fluid properties from Bell et al. [8]

System lay-out

The specific Triogen cycle is described below. Some major changes are made to the standard

Rankine cycle.

Barske pump (path two to three in figure 1-5b)

In order to reach the pressure difference which is necessary in the Triogen cycle and the low specific speed, a special pump type is chosen.

The Barske type pump which is used as main pump by Triogen is a partial emission pump invented by Willi U.M. Barske during World War II [19]. This pump is designed in order to reach a high pressure ratio with a low specific speed to supply propulsion systems of aircraft with fuel. The pressure difference in the disc is caused mainly by the centrifugal force [7]. Barske neglects other pressure buildups in the disc. An extra static pressure difference is realised with a diffuser, which turns dynamical head into static head.

Recuperator

The recuperator delivers an efficiency improvement to the basic ORC system explained in subsection 1-1-1. From the outlet of the main pump till the inlet of the evaporator, the stream is heated up (path three to four in figure 1-5a). From the outlet of the turbine to the inlet of the condenser, the stream is cooled down (path six to seven in figure 1-5a). The condenser is a shell-and-tube heat exchanger which is placed just in front of the condenser.

Evaporator (path four to five in figure 1-5b)

In the evaporator, the working fluid is heated up by a heat source. This can be an exhaust pipe of a combustion chamber for biomass or the the outlet of exhaust fumes of a internal combustion engine (ICE). In the evaporator the vapour is overheated by an extra 15 °C to prevent the turbine from severe damage due to droplet formation. The heat exchanger Triogen uses is a shell and tube type, a heat exchanger which can be easily cleaned from ashes which might come from the combustion chamber.

Turbine (path five to six in figure 1-5b)

The system uses a radial inflow single stage cantilever turbine to convert the energy from the working fluid into mechanical power. This cantilever turbine design is not very commonly used, mentioned by Valdimarsson [54], which makes the system a one of a kind. According to Weiß et al. [60] the isentropic efficiencies of these type of radial inflow turbines can be very high. The mass flow is governed by the supersonic flow in the stator of the turbine. More information on the control of the system can be found below.

Electrical generator

The high-speed turbo generator (HTG) which includes the turbine, electrical generator and the main pump converts the mechanical energy into electric energy. This HTG runs at a speed of 430 Hz [19] and uses one single casing, minimising the risk of leakage. The single shaft ensures that the pump and the turbine have the same rotational speed. The advantage of a single shaft is that the mechanical energy which is required for the pump, can be directly extracted from the turbine mechanical power. This puts an extra limitation on the system in terms of flexibility. According to Landelle et al. [29] 95 % of the pumps used in ORC are driven electrically, which makes the Triogen design quite unique. The HTG can not be operated below a rotational speed of 230 Hz otherwise the bearings lubrication is insufficient. The rotational speed is limited to 500 Hz. The electrical power which it can deliver is 90 kW to 170 kW [19]. The system uses a steady 6 kW to power the controls. Before the working fluid enters the main pump, part of the working fluid is split from the main flow, creating a secondary flow for the cooling of the HTG and as lubricant for the bearings. That is also a reason for Triogen to add a pre-feed pump. The secondary flow ends up in both the outlet of the turbine and the inlet of the condenser.

Condenser (path seven to one in figure 1-5b)

In the condenser the vapour is converted back into liquid and is undercooled about 2 °C to prevent the pump from cavitation. The condenser is a shell and tube type heat exchanger. The coolant can either be a liquid, like water from a canal or ocean, or a gas, like air, to cool the working fluid.

Now that all system parts are mentioned, some more information on important system characteristics is given. Below is mentioned which working fluid is used and how control of the system is managed.

Working fluid

The system can be applied to various heat sources but the main source of the installed systems (80%) is heat from ICE. The rest of the systems use biomass as heat source. The temperature range of the heating source is between 350 °C to 500 °C which is a high temperature range relative to the market [29, 12]. To be able to handle the high temperature the heat source supplies, the working fluid Triogen uses is toluene $C_6H_5CH_3$, a molecule from the group hydrocarbons [5]. Toluene is chosen because the critical temperature is, relative to other organic molecules, high. The working fluid is also chemically stable. The saturated liquid-vapour line of toluene is shown in figure 1-5a. Toluene is not used so often as working fluid according to Landelle et al. [29].

Control

The system is controlled by means of a variable speed drive (VSD). The temperature of the working fluid after the evaporator is measured and if the temperature is too high, the VSD increases the rotational speed of the HTG. This induces a higher pressure difference by the pump, which in turn increases the inlet pressure of the turbine. The choked flow is governed by the turbine inlet pressure and if this pressure increases, the mass flow increases. This higher mass flow decreases the inlet temperature of turbine, which is the trigger of the control loop in the first place.

Research on the Triogen system

Triogen already investigated quite some aspects of their cycle, in particular on the radial inflow cantilever turbine. E.J Beld did some research to the design of the Barske type pump which is applied in the ORC system of Triogen (confidential). Also research on the optimal working fluid is done by Vonk [56] with a fully worked out model of the cycle and a genetic algorithm for choosing the optimal working fluid, for both cost efficiency and technical limitations. Acetone is found to be a good replacement for toluene but also recommendations are given in case the working fluid is not changed. In the report of Diepeveen [16] an evaporator design optimisation is offered, which is necessary to replace the existing evaporator by a smaller one which is able to fit into a container space.

Application

Research for the usage of biomass combustion as heat input on the ORC system is done by van Buijtenen and Ganassin [55]. It describes how an innovative system is built to directly use the heat from the combustion into the evaporator of the ORC.

Expander

A 3-D Reynolds averaged Navier Stokes (RANS) steady state simulation of the turbine, including the flow passages, stator, rotor and diffuser is performed in order to indicate that the optimised stator increased the power output of the 5 kW electric energy and also improved the performance during off-design operation [23, 22]. A robust optimisation strategy to minimise entropy losses by optimising the radial stator vanes with a so called MoC-based method is carried out by Anand et al. [4]. This particular method reduces costs while CFD computations are not very cost-efficient. The study promises a 1.5% total-to-total turbine efficiency compared to the baseline design. By Otero R et al. [40], the unsteady, supersonic flow in several turbo expanders is simulated. 3-D and Quasi 3-D simulations were carried out in order to investigate the flow field of an old turbine rotor and an optimised rotor. Eventually a performance improvement is measured in the optimised rotor. The study of Smit et al. [50] focused on optimisation of the turbine using a genetic algorithm together with Q-3D RANS simulations. The total-to-static efficiency is increased by 4.3%.

Part load

A dynamic simulation of the Triogen cycle is performed with the software package MODELICA . The modelling is validated with measurements of transient responses. This method is valuable for inventing control strategies [10].

As mentioned above, Triogen already did research on the application of biomass on the cycle, they studied several aspects of the expander and they looked at how to dynamically simulate the cycle. No research is done on pump operation strategies to increase the system power output during part load operation. As discussed in subsection 1-1-1, not much research is done on pumps in ORCs and the studies found consider only other pump types and pumps which are not mechanically connected to the turbine.

The system will run mostly at off-design point as the (waste) heat source fluctuates in time [59]. While running the cycle in part load at a lower heat input, the mass flow, induced by the choked flow in the turbine, has to be lower. This change in mass flow induces the pump to run on another rotational speed than the design point which in turn causes the turbine to run on another working point. The mass flow can not be changed because it is necessary to cool down the heat input. If we can change the system to run the rotational speed which belongs to the best working point of the turbine and the mass flow can change as function of the heat input, the total power output of the ORC might increase.

1-2 Motivation, research goal and method

As discussed above, not much research is done on the application of a more efficient pump strategy. The turbine delivers the mechanical energy from the cycle to the generator. It is assumed that the power output of the system is mainly governed by the turbine efficiency. This can also be deduced from the explanation in section 1-1-1 and figure 1-2. The goal is to let the pump induce a rotational speed which fits best to the mass flow and the best working point of the turbine.

By changing the interaction between the rotational speed and the turbine inlet pressure (a different pump strategy) to induce a better fitting rotational speed to the turbine, the efficiency of the turbine can be maximised for the current mass flow.

Thus the goal of this research is *optimisation of the pump operation to increase the cycle efficiency of an ORC during part load.* Thus the research question is: *"How can the pump strategy be optimised in order to increase cycle efficiency of part load operation?"* Two basic sub questions might lead to this goal:

1. What is the optimal rotational speed of the HTG for the highest power output given a certain evaporator heat input?
2. How can this optimal rotational speed be provided?

The hypothesis on how this might be possible is to add a bypass or a throttle valve. Another possibility which is offered by Triogen is to design a conical valve in the diffuser of the pump. In this thesis, the most effective and cost efficient solution will be suggested.

From the cycle model, the gained power by adjusting the rotational speed of the HTG to the optimal one, will be shown. The cycle model is a simplified mathematical model in MICROSOFT EXCEL which will be explained in chapter 2.

For this cycle model, some in-depth analysis of the pump performance and the turbine map is necessary to implement the adjustments of the rotational speed for certain heat inputs. In the third and fourth chapter these respectively will be set out.

In the end the results of the simulations of the turbine and the outcomes of the cycle model are shown. Some insights in specific performance indicators are given. The optimal rotational speed will be mentioned and the way to implement this strategy is suggested

In the last chapter conclusions and recommendations are given.

Chapter 2

Cycle model

The optimal rotational speed for the system can be extracted from the results of a cycle model with a detailed turbine map. The outline of the cycle model is written down in this chapter

In the first section, the scope of the model is explained. After this, the elements of the system, and the mathematical structure are discussed. In section 2-3 is discussed how the energy balance is closed. Because the quality of the cycle model depends on the behaviour of the pump curve and the turbine map, the fourth and fifth section go in more depth about these topics. After that, the importance of the recuperator in the process will be explained in section 2-8. In section 2-9 the mass flow governed by the supersonic flow in the nozzle of the turbine is discussed. In section 2-10, the control mechanism of the model will be explained. The last section 2-11 discusses the solution method used in the model to reduce the necessary computational time.

2-1 Structure

The design of the cycle model begins with attaching the components in the right order and assign a correct mathematical framework to these components.

The cycle model consist of a MICROSOFT EXCEL file with a MICROSOFT EXCEL VISUAL BASIC FOR APPLICATIONS (VBA) addition but without any necessary add-ins. The REFPROP library [31] is used for the tabulated properties (which is later explained in section 2-11).

Because the input of the model is defined as evaporator heat input, the model is stable when used with a evaporator heat input from Q_{evap} =400 kW to 1200 kW.

The MICROSOFT EXCEL VBA script takes care of the control mechanism which is explained in further depth in section 2-10 but is also used for logging of data when the evaporator power input is changed.

2-2 Scope

2-2-1 Pressure convention

Throughout this report, pressures indicating conditions in different parts of the system are given. In this thesis all pressures given are absolute pressures unless mentioned otherwise.

2-2-2 Turbine inlet pressure

Due to the control mechanism on the system, the overheating at the pressure before the turbine inlet has to be known. Because above $p_{\text{tol,crit}} \approx 41.3\,\text{bar}$ the working fluid is in a supercritical state [31], no overheating value exists. The system model therefore can handle turbine inlet pressures up to $p_{\text{t,in}} = 41.3\,\text{bar}$. This pressure in combination with the stator height limits the maximum power input for the system. A higher stator height can lift up the power input of the system for an equal turbine inlet pressure.

2-2-3 Heat exchanger modelling

In reality, the pressure differences induced by the heat exchangers change as a function of the mass flow of the working fluid. However, for the cycle model in this report, fixed pressure differences induced by the heat exchangers are used. Vonk [56] explains the computation of the pressure drop by the heat exchangers in the Triogen system in depth. Because this research is focused on the interaction between the pump and the turbine, the emphasis is rather on the turbine wheel simulations and the pump model then on the heat exchanger modelling.

Heat exchanger part	**Symbol**	**Value**	**Unit**
Evaporator	Δp_{evap}	0.5	bar
Recuperator cold side	$\Delta p_{\text{rec,cold}}$	0.1	bar
Recuperator hot side	$\Delta p_{\text{rec,hot}}$	0.06	bar
Condenser	Δp_{cond}	0.005	bar

Table 2-1: Pressure drop inside heat exchanger parts for the working fluid

Not only the pressure difference induced by the heat exchangers is simplified, also the heat transfer inside the heat exchanger is assumed to be governed solely by enthalpy differences between inlet and outlet and mass flows. As a consequence, with changing evaporator heat input Q_{evap}, in principal, a totally new heat exchanger is designed to transfer the ”right” power. The same is done with the condenser and the recuperator. This is a very crude approach which fits the goal of this thesis, which focuses on the interaction between the pump and the turbine, but might be too inaccurate for other purposes. Vonk [56] made a full mathematical model to accurately approach the heat transfer inside the heat exchangers.

2-2-4 Turbine outlet pressure

The outlet pressure of the turbine in the simulations is independent of the inlet pressure of the recuperator in the cycle model. This is a known problem which has to be dealt with for the sake of simplicity of the model. The turbine simulations are further discussed in chapter 4.

2-2-5 Pre-feed pump

The pre-feed pump pressurises the working fluid at the outlet of the condenser $p_{\text{cond,out}} = 0.18\,\text{bar}$ to the fixed pressure of $p_{\text{pf,out}} = 3\,\text{bar}$. In reality, these in- and outlet pressures are not fixed but depend on the duty of the condenser and the power input of the pre-feed pump. Although the pump is controlled such that the output pressure approaches the used 3 bar, this control mechanism is not included in the cycle model, nor is the changing duty of the condenser. The condenser output pressure depends on the saturation temperature, which is assumed to be $T_{\text{cond,sat}} = 57\,°\text{C}$ and an undercooling of $\Delta T_{\text{cond,underc}} = 2\,°\text{C}$.

The efficiency of the pre-feed pump is assumed to be the same as the main pump. The complete efficiency analysis is given in section 3-3-1. In reality these efficiencies might not be the same (also mentioned in section 3-4). In the cycle model described in this chapter, the power consumption is assumed to be only mechanical power. In reality, the power consumed by the pre-feed pump includes the electrical efficiency of the pump.

2-2-6 Recuperator

The outlet of the recuperator is fixed as the overheating at the outlet of the evaporator is 20 °C at the condenser inlet pressure [18]. In reality the situation after the recuperator depends on the duty of the recuperator.

2-2-7 Lubrication and cooling

In the real system, after the pre-feed pump, part of the working fluid is tapped to feed into the housing of the high-speed turbo generator (HTG) to cool the shaft and lubricate the bearings. This part of the working fluid is fed back into the stream after the outlet of the turbine, back into the main flow. This secondary flow is not taken into the account in the model because it is considered negligibly small with respect to the rest of the flow.

2-3 Energy balance

To ensure the correct working principle of the model, an energy balance is set up. In this section a short explanation of this sum is worked out.

The working fluid is taken as the volume which is gaining and loosing energy. It is assumed that there is no working fluid entering or leaving the system. In reality, the working fluid is used for cooling the shaft and for lubrication of the bearings, but this is left out of the scope of this report as mentioned in subsection 2-2-7.

The energy used for the main pump and pre-feed pump are extracted from the turbine power because it is not leaving the system. This power is added as pressure difference and temperature increase of the fluid. If the secondary pump would have had an electrical efficiency, the heat would also be partly absorbed by the working fluid so this also is left out of the scope of this energy balance.

The working fluid only gains thermal energy in the evaporator. The energy leaving the system is the thermal energy of the condenser and the mechanical turbine power without the pumping power of both pre-feed and main pump.

The energy balance is closed as such:

$$E_{\text{tot}}{=}Q_{\text{evap}} - Q_{\text{cond}} - (W_{\text{turb}} - W_{\text{mp}} - W_{\text{pf}}) \tag{2-1}$$

Where E_{tot} the total energy crossing the boundaries of the system, which has to reach zero. Q_{evap} the heat input of the evaporator, Q_{cond} the heat output of the condenser, W_{turb} the work output of the turbine, W_{mp} the work input of the main pump and W_{sp} the work output of the secondary pump.

This balance E_{tot} has to be equal to zero, otherwise the model is not valid and the energy balance is not closed.

The quantities in equation 2-1 are computed as such:

$$Q_{\text{evap}}{=}\dot{m}_{\text{wf}}(h_{\text{evap,out}} - h_{\text{evap,in}}) \tag{2-2}$$

$$Q_{\text{cond}}{=}\dot{m}_{\text{wf}}(h_{\text{cond,in}} - h_{\text{cond,out}}) \tag{2-3}$$

$$W_{\text{turb}}{=}\dot{m}_{\text{wf}}(h_{\text{t,in}} - h_{\text{t,out}}) \tag{2-4}$$

$$W_{\text{mp}}{=}\dot{m}_{\text{wf}}(h_{\text{mp,out}} - h_{\text{mp,in}}) \tag{2-5}$$

$$W_{\text{sp}}{=}\dot{m}_{\text{wf}}(h_{\text{pf,out}} - h_{\text{pf,in}}) \tag{2-6}$$

In this section the energy balance is closed. Next section includes the turbine map implementation into the cycle model.

2-4 Turbine map

A fixed temperature as function of the evaporator heat input is assumed at the inlet of the turbine. Because the pressure after the pump is known combined with the fixed pressure drop in the heat exchangers (shown in table 2-1), the pressure before the turbine is known. By using the table, the corresponding vaporisation temperature can be calculated, which can consequently be used to determine the turbine inlet temperature. The turbine inlet pressure $p_{\text{t,in}}$ and the rotational speed n are used as the input for the turbine map.

The output of the turbine map consist of the entropy at the outlet of the turbine. Solely this, together with a recuperator inlet pressure (which can also be computed with the condenser pressure and the assumed pressure drop) can give all necessary turbine outlet conditions.

In section 4-5, the method of finding the outlet conditions at the turbine outlet is written down. With the equation 4-7 and the coefficients in table 4-4 the entropy can easily be computed. Together with the turbine outlet pressure $p_{\text{t,out}}$ which can be deduced from the condenser pressure and the pressure drops of table 2-1, this gives all thermodynamic properties at the outlet.

The outlet conditions of the turbine are necessary to compute the heat transfer in the recuperator.

2-5 Pump curve

The main pump induces a higher pressure to the flow out of the pre-feed pump. Because the pump governs the pressure before the inlet of the turbine $p_{\mathrm{t,in}}$, this basically controls the system and influences the turbine performance as discussed in section 2-4.

The pump in the model requires a rotational speed of the axis n. It also requires the properties $T_{\mathrm{pump,in}}$, $p_{\mathrm{pump,in}}$ of the working fluid at the inlet of the pump in order to compute a density of the fluid.

The output of the pump model consist of a pump outlet temperature $T_{\mathrm{pump,out}}$ and a pump outlet pressure $p_{\mathrm{pump,out}}$. Because the pump power for the Barske pump can be approached with analytical formulas, also the power used by the pump can be extracted from the pump model.

More information on the pump curve is given in chapter 3. In this chapter, more in-depth information is given on pump design, pump behaviour for different mass flows and efficiencies depending on mass flow and rotational speed.

2-6 Evaporator

Previous section explained the input of the pump model for the cycle model. This section mentions the calculations related to the evaporator.

As discussed in subsection 2-2-3, the cycle model puts the focus on the interaction between the pump and the turbine. The only mathematical expression defining the duty of the evaporator is the heat input $Q_{\mathrm{evap,in}}$. Together with the temperature assumed at the hot side of the evaporator, the heat exchanger is effectively ”redesigned” every simulation with a different heat input.

Because of the basis of this thesis, it is of interest to continuously change the evaporator heat input. Thus this is an input, together with the inlet temperature of the turbine $T_{\mathrm{t,in}}$. The pressures around the evaporator can be directly computed. The pressure after the main pump is computed according to the pump model discussed in the previous section. With the pressure differences in table 2-1, the pressures around the evaporator can be computed.

At the hot side of the evaporator, the temperatures are fixed and the mass flow is governed by the specific heat of flue gasses and the heat input $Q_{\mathrm{evap,in}}$. In reality the outlet condition of the hot side changes as the duty of the evaporator change. In the cycle model, the duty of the evaporator is an input value and the conditions of the flue gas side are not taken into account.

The output temperature of the evaporator is computed with the mass flow of the working fluid, the heat input and the enthalpy at the inlet of the evaporator. This calculation is shown in equation 2-11.

$$\sum E = 0 \tag{2-7}$$

$$\dot{m}_{\mathrm{fg}} c_{p,\mathrm{fg}} \Delta T_{\mathrm{fg}} = -\dot{m}_{\mathrm{wf}} \Delta h_{\mathrm{wf}} \tag{2-8}$$

$$Q_{\mathrm{evap}} = -\dot{m}_{\mathrm{wf}} (h_{\mathrm{wf,in}} - h_{\mathrm{wf,out}}) \tag{2-9}$$

$$Q_{\mathrm{evap}} = \dot{m}_{\mathrm{wf}} (h_{\mathrm{wf,out}} - h_{\mathrm{wf,in}}) \tag{2-10}$$

$$h_{\mathrm{wf,out}} = h_{\mathrm{wf,in}} + \frac{Q_{\mathrm{evap}}}{\dot{m}_{\mathrm{wf}}} \tag{2-11}$$

2-7 Condenser

Similar to the condenser calculations of the evaporator above, the condenser is simplified in this model.

The outlet pressure is fixed at the saturation pressure at $T_{\mathrm{cond,sat}} = 57\,^\circ\mathrm{C}$ and can be computed with REFPROP [31], $p_{\mathrm{cond,sat}} = 0.178\,\mathrm{bar}$. The outlet temperature is assumed to be governed by this saturation temperature minus the undercooling temperature $\Delta T_{\mathrm{underc,cond,out}} = 2\,^\circ\mathrm{C}$, $T_{\mathrm{cond,out}} = T_{\mathrm{cond,sat}} - \Delta T_{\mathrm{underc,cond,out}} = 57\,^\circ\mathrm{C} - 2\,^\circ\mathrm{C} = 55\,^\circ\mathrm{C}$. Undercooling at the outlet of the condenser is necessary. At the outlet of the condenser and in the buffer tank, the outlet pressure is $p_{\mathrm{cond,sat}} = 0.178\,\mathrm{bar}$. Before the pre-feed pump, the total pressure stays constant but the dynamic pressure increases. Therefore the static pressure decreases and when this static pressure reaches the saturation pressure of the working fluid, cavitation can cause destruction of the pump blades.

The inlet pressure is computed with the pressure drop in the condenser, which can be extracted from table 2-1. The model assumes an overheating of $\Delta T_{\mathrm{overh,rec,out}} = 20\,^\circ\mathrm{C}$ at the inlet of the condenser. All required enthalpies and entropies are calculated with REFPROP [31].

Thus all properties of the working fluid are known from the start, which makes the modelling of this component trivial. The duty of the condenser depends solely on the mass flow which is variable in the cycle model.

2-8 Recuperator

The function of the recuperator in the process is to increase the cycle efficiency by heating up the inlet of the evaporator by means of cooling the turbine outlet stream. The effect of the recuperator can be seen in figure 2-1.

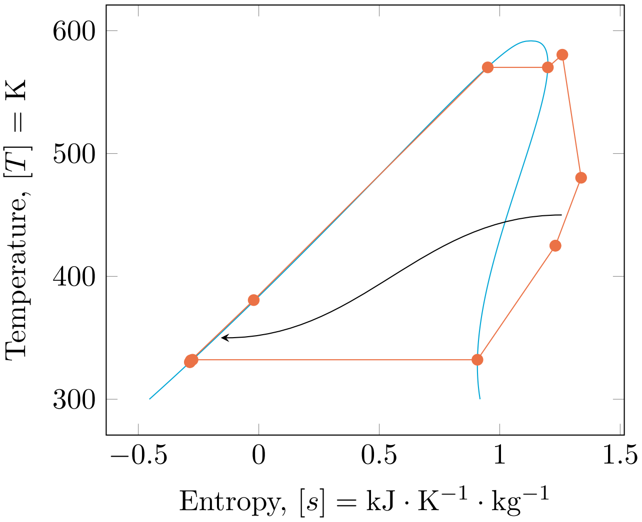

Figure 2-1: Heat recovered by the recuperator

The inlet pressure of the condenser is fixed and the model assumes an overheating of $\Delta T_{\text{overh,rec,out}} = 20\,°\mathrm{C}$ at the outlet of the hot side of the recuperator, as discussed above in section 2-7. The absolute temperature and static enthalpy can be found with REFPROP [31].

Because the properties at the outlet of the condenser are fixed and the pump model provides the situation after the pump, the properties of the working fluid before entering the cold side of the recuperator are known.

By the turbine map, the outlet conditions of the turbine are computed.

The model computes the outlet enthalpy of the recuperator cold side. This is done with a very simplistic energy balance.

$$\sum E = 0 \tag{2-12}$$
$$= E_{\text{cold}} + E_{\text{hot}} \tag{2-13}$$
$$E_{\text{cold}} = -E_{\text{hot}} \tag{2-14}$$
$$\dot{m}_{\text{wf}} \Delta h_{\text{cold}} = -\dot{m}_{\text{wf}} \Delta h_{\text{hot}} \tag{2-15}$$
$$\dot{m}_{\text{wf}} (h_{\text{rec,cold,out}} - h_{\text{rec,cold,in}}) = -\dot{m}_{\text{wf}} (h_{\text{rec,hot,out}} - h_{\text{rec,hot,in}}) \tag{2-16}$$
$$\dot{m}_{\text{wf}} (h_{\text{rec,cold,out}} - h_{\text{rec,cold,in}}) = \dot{m}_{\text{wf}} (h_{\text{rec,hot,in}} - h_{\text{rec,hot,out}}) \tag{2-17}$$

Because the mass flow exist on both sides, they cancel out and the unknown enthalpy can be found

$$h_{\text{rec,cold,out}} = (h_{\text{rec,hot,in}} - h_{\text{rec,hot,out}}) + h_{\text{rec,cold,in}} \tag{2-18}$$

2-9 Choked flow

The mass flow of the working fluid through the cycle is governed by the choked flow at the throat which is created by the stator. When it is assumed that the inlet pressure of the turbine stays almost constant before entering the diverging part of the throat, we can say that the enthalpy is a function of the static enthalpy and the speed of sound.

In appendix A, the equation for the speed of sound for an ideal gas is given. To verify if this simplistic formula can be used in this case when toluene as working fluid is used, the compressibility for different inlet pressures and temperatures is computed with [31]. As can be seen in figure 2-2, the compressibility is changing with fluid conditions so the function equation A-2 can not be used in this case.

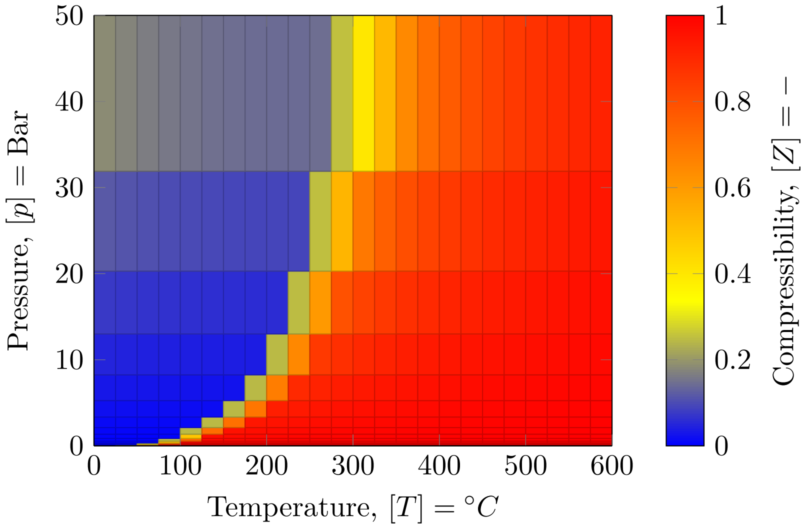

Figure 2-2: Compressibility of toluene according to [31]

We also assume that the inlet of the throat is perfectly insulated so the entropy does not change. Thus the variables are picked as displayed in figure 2-3. The static enthalpy $h_{\text{t},0}$ at the inlet of the turbine is derived from the pressure at the inlet of the turbine $p_{\text{t,in}}$ and the inlet temperature $T_{\text{t,in}}$. The entropy at the inlet is also derived from these two conditions.

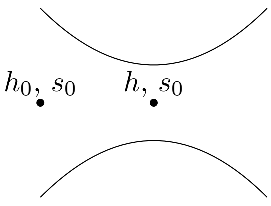

Figure 2-3: Schematic approach of the throat at the stator of the turbine

The stagnation enthalpy describes the enthalpy when the fluid stands still, so the velocity energy is added. The stagnation enthalpy is also called the total enthalpy. The static enthalpy in the throat is computed as such

$$h_{\text{stag}}{=}h_{\text{stat}} + \frac{1}{2}C^2 \tag{2-19}$$

$$h_{\text{stat}}{=}h_{\text{stag}} - \frac{1}{2}C^2 \tag{2-20}$$

with $[h] = \text{J} \cdot \text{kg}^{-1}$

Because we are not looking for the enthalpy but for the speed of sound, and because this $C = f(h_{\text{stat}}, s_0)$, we iterate this formula with an initial guessed C. The speed of sound as function of the enthalpy and the entropy can be found with CoolProp [8]. Because we used REFPROP for all other properties but the speed of sound cannot be verified with REFPROP , we used CoolProp instead and computed the relative difference between enthalpy model and entropy model with the following equations:

$$\frac{\Delta h}{h}{=}\frac{h_{\text{rp}} - h_{\text{cp}}}{h_{\text{rp}}} \tag{2-21}$$

$$\frac{\Delta s}{s}{=}\frac{s_{\text{rp}} - s_{\text{cp}}}{s_{\text{rp}}} \tag{2-22}$$

The outcomes are shown in figure 2-4. As can be seen in this figure, the difference of enthalpy models is small enough to be neglected.

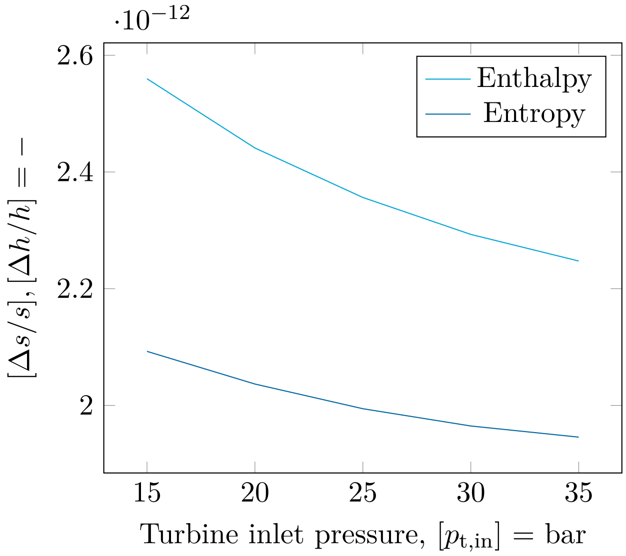

Figure 2-4: Relative difference between REFPROP and CoolProp

The mass flow $\dot{m}$ can be computed

$$\dot{m}{=}\rho\mathcal{Q} \tag{2-23}$$

$$={\rho}(\mathcal{A}a) \tag{2-24}$$

$$={\rho}(\mathcal{W}\mathcal{H}a) \tag{2-25}$$

The width of the channel in the turbine is $\mathcal{W}$ and the height of the original stator is $\mathcal{H}$. The height of the stator for different systems can be changed in order to change the mass flow through the whole system for certain turbine inlet pressures. The mass flow as function of the inlet pressure and the stator height can be found in figure 2-5.

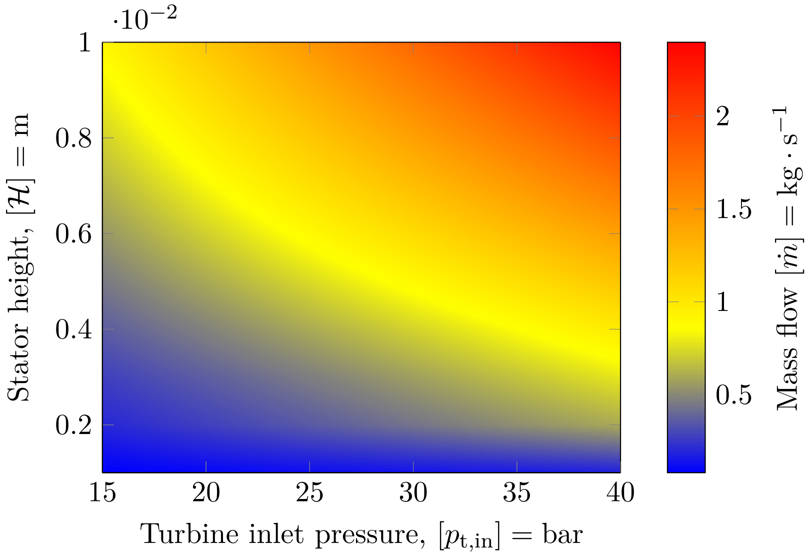

Figure 2-5: Choked flow depending on turbine inlet pressure and stator height

Given a certain stator height $\mathcal{H}$ and a turbine inlet temperature $T_{\mathrm{t,in}}$, the mass flow is directly related to the inlet pressure and is fit with MATLAB and the data from the computation above.

The mass flow for a certain inlet pressure (with $[p_{\mathrm{t,in}}] = \mathrm{bar}$ and $\dot{m}_{\mathrm{wf}} = \mathrm{kg} \cdot \mathrm{s}^{-1}$) is given in the following polynomial:

$$\dot{m}_{\mathrm{wf}} = \sum_{i=0}^{5} K_i p_{\mathrm{t,in}}^i \tag{2-26}$$

The constants which are used for this polynomial are shown in figure 2-2.

i	5	4	3	2	1	0
K	-7.3578×10^{-8}	9.6161×10^{-6}	-4.9077×10^{-4}	1.2281×10^{-2}	-1.0404×10^{-1}	7.5279×10^{-1}

Table 2-2: Parameters for the estimation of the mass flow of the working fluid as function of the turbine inlet pressure

The proportion of variance of this fit is $\mathcal{R}^2 = 0.9995$. The outcome of this function is shown in figure 2-6.

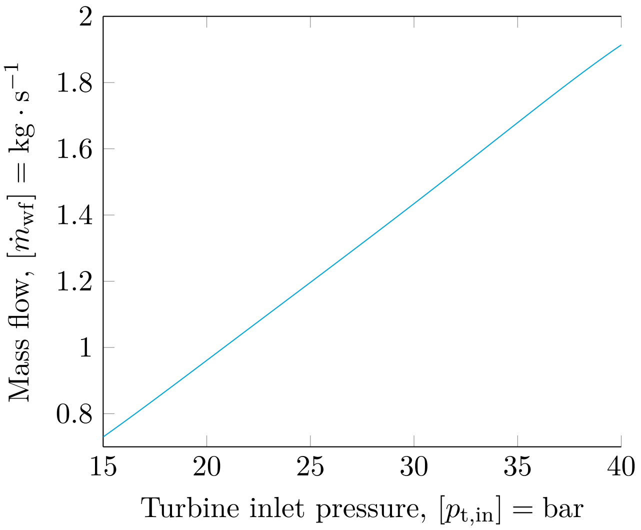

Figure 2-6: Mass flow as function of the turbine inlet pressure given a certain stator height

2-10 Control

Above is described how the turbine inlet pressure $p_{\mathrm{t,in}}$ defines the mass flow of the system $\dot{m}_{\mathrm{wf}}$. In this section, the control of the system is discussed.

The system is controlled by a variable speed drive (VSD) which can put a ”load” onto the HTG shaft in order to increase or decrease the rotational speed n. The evaporator inlet heat $Q_{\mathrm{evap,in}}$ defines the mass flow of the working fluid.

The sensor part of the control mechanism is confidential. For a great approach to identify the control behaviour, it can be assumed that the system is controlled on the inlet temperature of the turbine.

The control mechanism actuates the VSD which in turn changes the rotational speed of the HTG. Because the dynamics of the VSD are not covered in the model, the actuator directly changes the rotational speed.

The model converges to the solution by a custom written goal seek function. The MICROSOFT EXCEL VBA script compares the turbine inlet temperature to a reference value and then adjusts the rotational speed to the old value together with 0.1 times the error between the turbine inlet temperature and the reference value. This computation is shown in equation 2-27. When the temperature is too high, the rotational speed must increase and vice versa.

$$n_{\mathrm{new}}{=}n_{\mathrm{old}} + 0.1(T_{\mathrm{t,in}} - T_{\mathrm{ref}}) \tag{2-27}$$

After the rotational speed is changed, the mass flow and the efficiency of the pumps are updated and the control loop is repeated. This is necessary because there are actually two loops inside the model, displayed in figure 2-7.

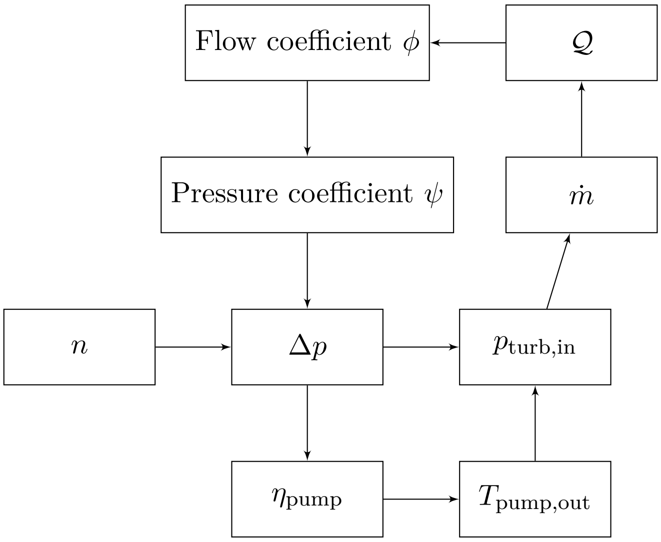

Figure 2-7: Schematic preview of the iteration cycle

2-11 Tabulated properties

For the cycle model, properties of the working fluid toluene are required for certain conditions. Because the model will be used to compute the system performance for a large number of evaporator heat inputs, it is required to run as fast as possible.

Property libraries such as REFPROP [31] and COOLPROP [8] can be used inside MICROSOFT EXCEL to verify fluid properties. The libraries are very precise but also make the model slow. In order to increase the speed of the model, properties can also be found in tables.

The tables have to be designed carefully because unsystematic work and wrong choice of value picking can lead to wrong results and can also influence the convergence of the model.

2-11-1 Range

To ensure the tables covers all fluid properties possible in the cycle model, the ranges of properties are listed in table 2-3.

Result	**Input 1**	**Input 2**	**First range**	**Second range**	**Purpose**
Saturation pressure	Temperature		40 °C to 70 °C		Condenser outlet pressure
Saturation temperature	Pressure		0.1 bar to 1 bar		Condenser overheating
Saturation temperature	Pressure		1 bar to 40 bar		Evaporator overheating
Enthalpy	Pressure	Temperature	0.1 bar to 1 bar	40 °C to 100 °C	Condensor in and outlet enthalpy
Entropy	Pressure	Temperature	0.1 bar to 4 bar	40 °C to 70 °C	Entropy at pump inlets
Temperature	Pressure	Enthalpy	0.1 bar to 40 bar	$-100\,\mathrm{kJ\cdot kg^{-1}}$ to $1700\,\mathrm{kJ\cdot kg^{-1}}$	Temperature at various points in the system
Enthalpy	Pressure	Entropy	0.1 bar to 40 bar	$1\,\mathrm{kJ\cdot kg^{-1}\cdot K^{-1}}$ to $2\,\mathrm{kJ\cdot kg^{-1}\cdot K^{-1}}$	Static enthalpy outlet turbine
Density	Pressure	Enthalpy	2 bar to 5 bar	40 °C to 100 °C	Density at the inlet of the main pump

Table 2-3: Thermodynamical functions necessary for the cycle model, tabulated to increase computational speed.

2-11-2 Logarithmic versus linear

To accurately describe the fluid properties as function of dependent properties with the constructed tables and also minimise computational time, a decision whether to use a linear or logarithmic scale for the dependant properties has to be made. In 2-3, the required fluid properties with the dependent variables are given. In appendix B, the logarithmic dependence of the pressure on the entropy is discussed. Thus the pressure scale which is used in the tables is chosen to be logarithmic.

2-11-3 Cubic interpolation

The properties are computed using linear interpolation within the domain of the points neighbouring the required points. This computation method is written down in equation 2-28 and visually displayed in figure 2-8.

$$f(x,y)=\frac{\frac{f(x_{i+1},y_n)-f(x_i,y_i)}{x_{i+1}-x_i}-\frac{f(x_{i+1},y_{i+1})-f(x_n,y_{i+1})}{x_{i+1}-x_i}}{y_{i+1}-y_n} \tag{2-28}$$

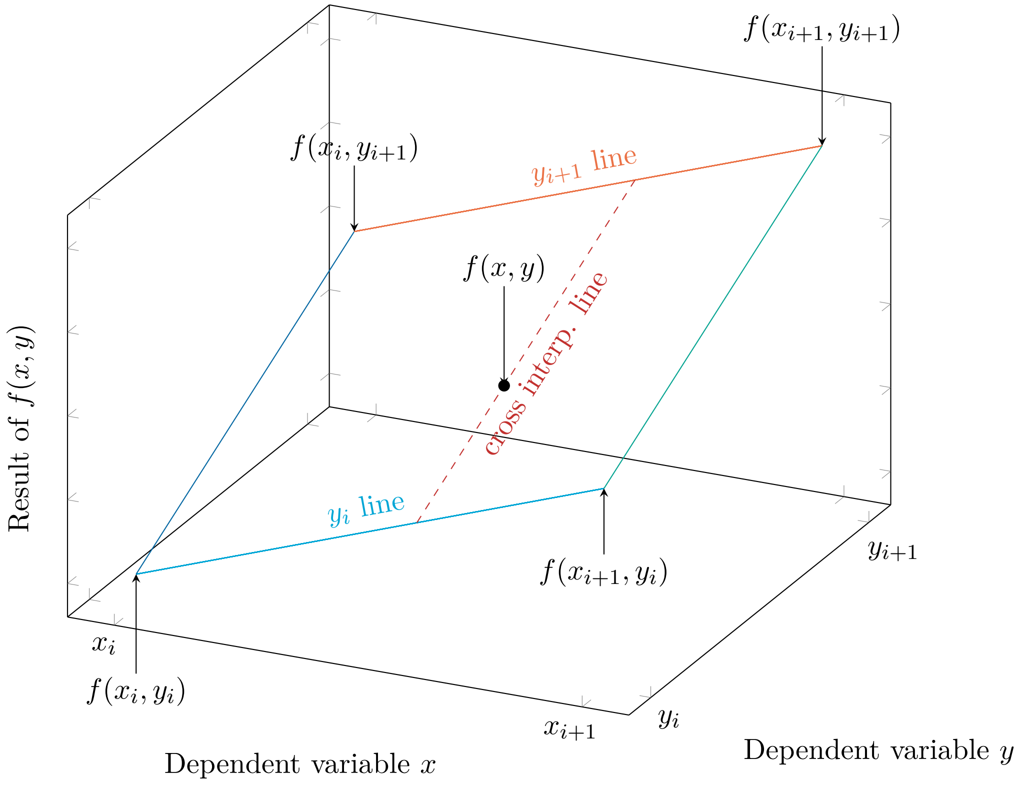

Figure 2-8: Interpolation method for tabulated properties, mathematical description in equation 2-28

2-11-4 Verification

To investigate whether the tabulated properties are accurately approaching the thermodynamic properties from REFPROP , a test model file was made which compared the REFPROP outcomes to the tabulated results. The entropy as function of temperature and pressure was verified with both the REFPROP software and the tabulated entropy. The relative entropy difference in figure 2-9 is computed as described in equation 2-29.

$$\frac{\Delta s}{s} = \frac{s(p,T)_{\mathrm{tab}} - s(p,T)_{\mathrm{rp}}}{s(p,T)_{\mathrm{rp}}} \tag{2-29}$$

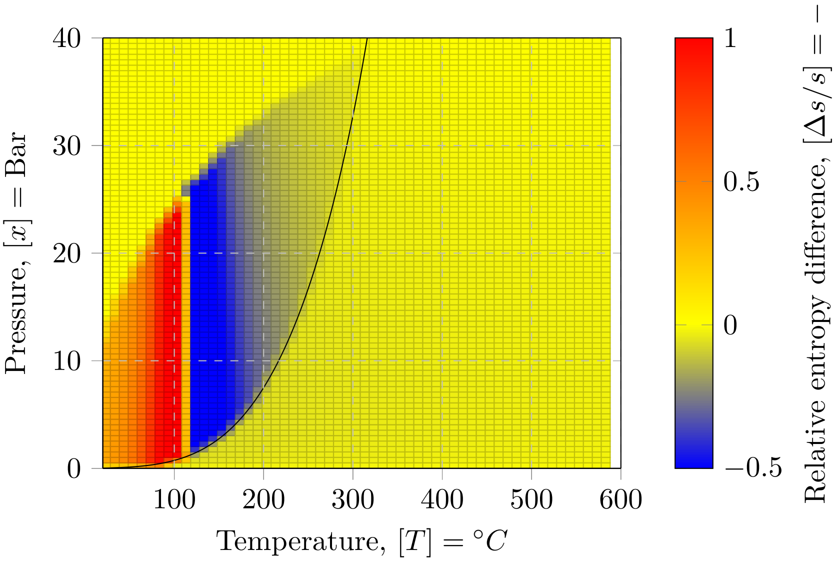

Figure 2-9: Relative entropy difference as function of pressure and temperature

It can be observed that the relative entropy difference is almost equal to zero in most of the domains but differs heavily from zero when reaching the coexistence area. To ensure the accurateness of the tables, the properties accessed by the model may not be inside this area. According to figure 1-1, the points for which properties will be calculated in the model are not inside this coexistence region, hence the tables are accurate.

2-11-5 Saturation temperature

Because of convergence issues, the tabulated saturation temperature as function of pressure was not precise enough. A polynomial is constructed with MICROSOFT EXCEL to realise a continuous function for the saturation temperature. The computation of the approach can be seen in equation 2-30. The units which hav to be used are $[p_{\mathrm{t,in}}]$ = bar and $[T_{\mathrm{sat}}(p)]$ = °C.

$$T_{\mathrm{sat}}(p) = \sum_{i=1}^{3} K_i p^{A_i} \tag{2-30}$$

With the associated constants:

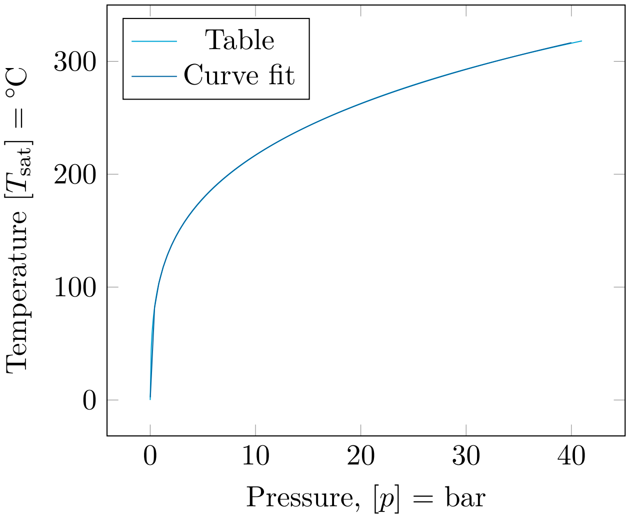

Figure 2-10: Caption

i	1	2	3
K	94.63402504	11210788996	-11210788981
A	0.28414228	7.50332E-10	0

Table 2-4: Coefficients necessary for equation 2-30

The proportion of variance of this fit is $\mathcal{R}^2 = 0.999998$, which is in fact very high. The function and the values from the property table is shown in figure 2-10.

Now that the overall method of the cycle method is described, more detailed information about both the pump performance and the turbine simulations are given respectively in the next chapters.

Chapter 3

Pump modelling

In this chapter the outline of the pump model will be further explained. Because this part of the cycle model is of much importance of a good functionality of the cycle model, more in-depth information will be provided.

First the current pump design will be discussed with some specific dimensions which are necessary for section 3-2. This section explains the characteristic performance of the pump. The third section will go further in depth about the power consumption and the efficiency of the pump. The last chapter explains something about the implementation of the pump model into the cycle model.

3-1 Design

The current pump design is based on a design optimisation by E.J. Beld, a confidential in-house report. Given that this must be the most optimal design of the pump for the design operation conditions, no further research will be done in this thesis to redesign the pump its dimensions.

The characteristic dimensions for the Barske pump is shown in figure 3-1.

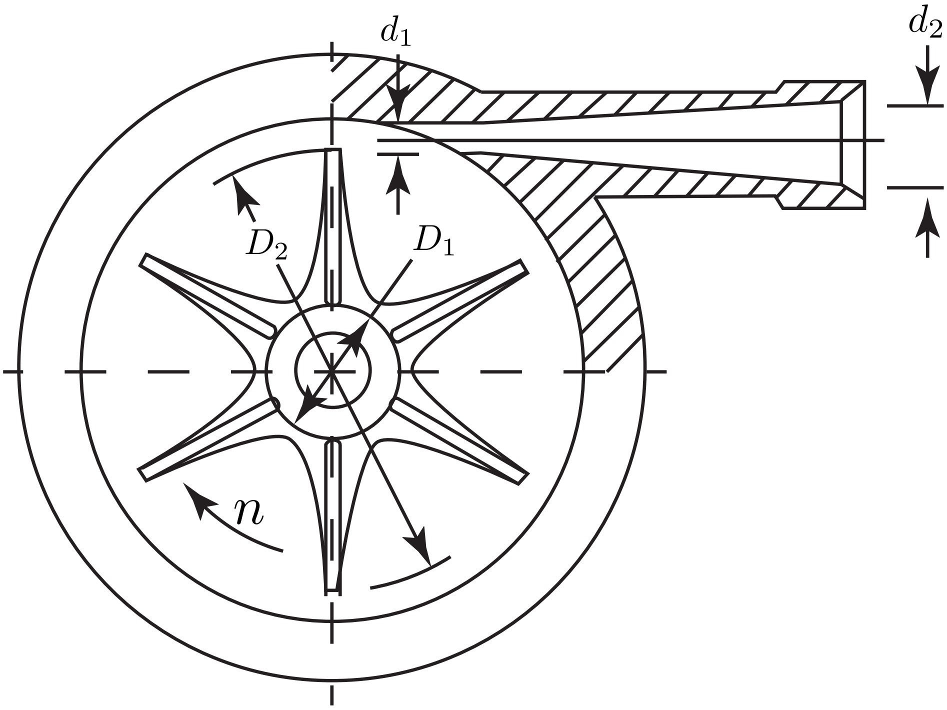

Figure 3-1: Schematic view of pump dimensions, adapted from Gravelle [20]

The dimensions of the current design matching the places in the scheme depicted in figure 3-1 can be found in table 3-1.

Description	Symbol	Value	Unit
Disc inner diameter	D_1	0.015	m
Disc outer diameter	D_2	0.054	m
Diffuser inlet diameter	d_1	0.0045	m
Number of diffusers	i_d	2	-

Table 3-1: Pump dimensions

These pump dimensions are necessary to use the performance equations in the next section.

3-2 Performance

Described above in section 3-1, when all properties of the pump are known, a performance analysis can be done.

The Barske pump provides a pressure difference for low specific speeds and high pressure ratios. The disc inside the pump housing (shown in figure 3-1) rotates at very high rotational speeds $n = 230\,\mathrm{Hz}$ to $500\,\mathrm{Hz}$. The pump generates pressure in two ways, namely a static pressure by means of the centrifugal force and a dynamic pressure because of the high rotational speed.

The dependence of the impeller tip speed on the static pressure difference induced by the pump is described in appendix C:

$$p_{\text{tot}}{=}\rho\left(\frac{U_2^2-U_1^2}{2}+\frac{U_2^2}{2}\right) \tag{3-1}$$

This definition is also used by Barske [7] and Gravelle [20].

Only a part of the dynamic head can be converted to static head. This is governed by the diffuser efficiency. As can be seen above, the pressure difference is mainly depending on the impeller tip speed U_2. The dependence of this speed on the pressure is given by the following equation of the pressure coefficient ψ:

$$\psi{=}\frac{\text{resultant pressure difference}}{\text{impeller tip speed}}=\frac{\Delta p_{\text{pump}}}{g\rho U_2^2}=\frac{\Delta p_{\text{pump}}}{g\rho(D_2\pi n)^2} \tag{3-2}$$

The speed of the flow in the diffuser is not equal to the speed of the impeller tip, this ratio is given in the equation of the flow coefficient ϕ:

$$\phi{=}\frac{\text{real velocity of the flow}}{\text{velocity of the impeller tip}}=\frac{v_{\text{throat}}}{U_2^2}=\frac{4Q}{\pi^2 i_d n D_2 d_1^2} \tag{3-3}$$

With Q the volumetric flow, i_d the number of diffusers, which is in the Triogen case $i_d = 2$. n the rotational speed, g the gravitational constant and the pump dimensions d_1 and D_2 which are given above in table 3-1.

Together equations 3-3 and 3-2 above can be used as a simple model to characterise the pump. The flow coefficient is computed with values which are present as input for this model. From Gravelle [20], the relation between flow and pressure coefficient of a Barske type pump can be deduced, which is shown in figure 3-2. Equation 3-2 is rewritten in order to compute the pressure difference.

$$\Delta p_{\text{pump}}{=}\psi g\rho(D_2\pi n)^2 \tag{3-4}$$

The $\phi-\psi$ relation is modelled with a linear estimation in MICROSOFT EXCEL and can be computed as such:

$$\psi{=}\sum_{i=1}^{6}K_i\phi^{A_i} \tag{3-5}$$

With the constants provided in table 3-2.

i	1	2	3	4	5	6
A	1.07339012	14.98944605	14.69170113	1.202267088	14.99436449	0
K	0.796868607	13288.71385	-216.1760893	-0.787185043	-13072.87237	0.713845525

Table 3-2: Constants for computation of pressure coefficient as function of flow coefficient

The polynomial of this relation is shown in figure 3-2.

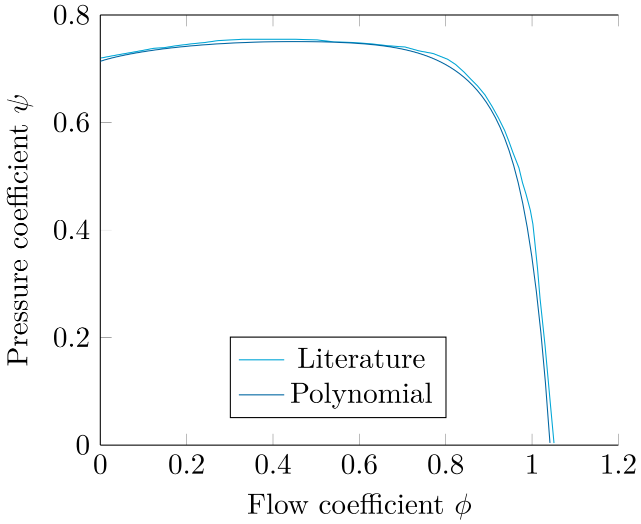

Figure 3-2: Head coefficient as function of the flow coefficient adapted from Gravelle [20]

The method of using the flow and head coefficient for characterisation of the pump is established by E.J. Beld, who redesigned the pump in order to get the optimal pump design for design conditions. Experimental findings from E.J. Beld during the optimisation of the pump design are available in-house but confidential. The dimensions of his second redesign are used in this thesis as reference.

With the dimensions above, an inlet pressure of the main pump of $p_{\text{mp,in}} = 3\,\text{bar}$ and a rotational speed of $n_{\text{des}} = 430\,\text{Hz}$, the pump curve of the Barske pump is shown in figure 3-3

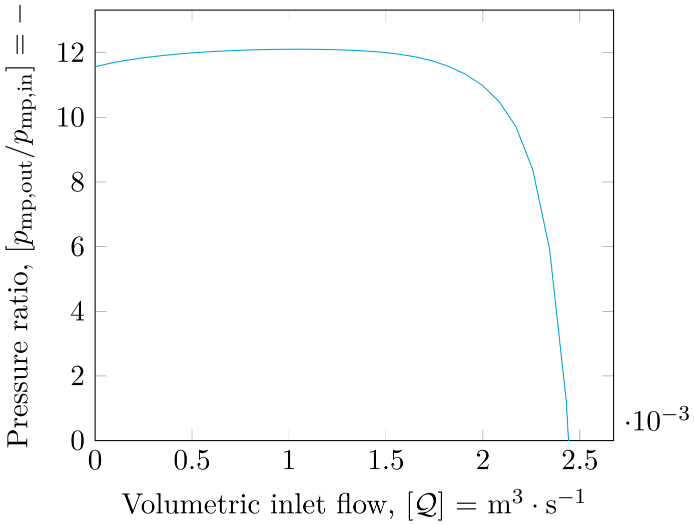

Figure 3-3: Pump curve for given dimensions with a rotational speed of $n_{\text{des}} = 430\,\text{Hz}$

As can be seen in this figure, the curve is similar to the curve of the coefficients in figure 3-2.

This characteristic curve of a Barske type pump has a steep drop of pressure after a certain maximum volumetric flow. Physically this means that when the volumetric flow is too large and the pump does not pressurise the fluid any more.

In figure 3-4, the pressure ratio for different rotational speeds and mass flows are given. The density which is used is $\rho \approx 832\,\mathrm{kg}\cdot\mathrm{m}^{-3}$. This density can be assumed constant because the inlet conditions of the main pump do not change very much in this cycle model. The fluctuation of density for various evaporator heat inputs is $1.2 \times 10^{-5}\%$. Equations 3-3, 3-4 and 3-5 are used to come up with figure 3-4.

In this figure 3-4, the pressure ratio tends to reach the same linear increase when the rotational speed is high. The pressure ratio depends very much on the mass flow for low rotational speeds. For low mass flow, the pressure ratio scales almost linearly with the rotational speed. This might be a consequence of the small dynamic pressure difference conversion of the diffuser.

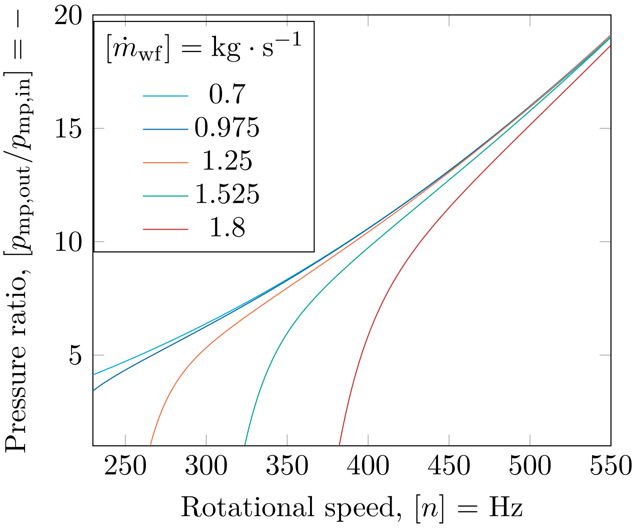

Figure 3-4: Pressure ratio for different mass flows

In the next section, power consumption of the pump for certain operation conditions are given.

3-3 Required power

As presented by Barske [7], the following formulas are used to equate the power put into the pump and the net power output.

The power which is actually transferred to the fluid, i.e. the power output:

$$P_{\mathrm{fluid}} = \frac{\Delta p \dot{m}}{\rho} \tag{3-6}$$

With $\dot{m}$ the mass flow of the working fluid, ρ the density of the working fluid and Δp the pressure difference computed in the previous section.

An empirical method to approach the frictional power input is stated by Barske [6]. The dimensions can be found in table 3-1.

$$P_{\text{fric}}{=}0.743\rho\nu^{0.2}n^{2.8}(D_2^{4.6}+1.38\cdot D_1^{4.6}) \tag{3-7}$$

With $\nu \approx 4.72 \times 10^{-7}\,\mathrm{m}^2 \cdot \mathrm{s}^{-1}$ the kinetic viscosity of the working fluid from REFPROP , ρ the density of the working fluid and n the rotational speed of the axle.

The power input to increase the velocity of the fluid:

$$P'{=}\frac{\dot{m}}{2}(2U_2^2-U_1^2) \tag{3-8}$$

With U_1 the speed of the flow at the inlet of the blade $U_1 = D_1\pi n$, U_2 the speed of the flow at the outlet of the blade $U_2 = D_2\pi n$ and $\dot{m}$ the mass flow of the working fluid.

These equations are required to compute the power needed to pump the fluid to a certain pressure. They are also used for the efficiency computations in the next section.

3-3-1 Efficiency

With the power consumption and power output to the fluid calculated in the previous subsection, the efficiency can be computed as:

$$\eta_{\text{pump}}{=}\frac{P_{\text{fluid}}}{P'+P_{\text{fric}}} \tag{3-9}$$

In figure 3-5, the efficiencies for different rotational speeds and mass flows are given. The equations 3-3, 3-4 and 3-5 are used and the density of $\rho = 832\,\mathrm{kg}\cdot\mathrm{m}^{-3}$ is used. Above is already stated that this is a valid assumption.

It is apparent that the efficiency fluctuates around $\eta_{\text{pump}} \approx 0.6$ and has a very sharp drop-off, similar to the pump curve shown in figure 3-3.

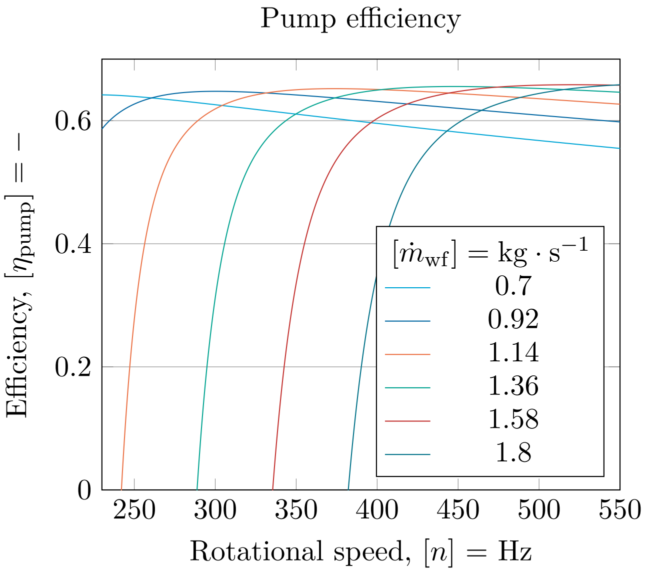

Figure 3-5: Pump efficiencies for different mass flow and rotational speed

3-4 Implementation in model

Now that above is described how the pump is modelled, what important performance characteristics are and how the efficiency can be computed, the model can be implemented into the cycle model.

The pump model depends solely on the rotational speed n and the density of the working fluid. These are the input parameters, the output parameters are the pressure difference and the efficiency. The density can be verified with the tabulated properties and is a function of the pressure and the temperature at the inlet of the pump.

It is assumed that the pre-feed pump has the same isentropic efficiency as the main pump but which is in reality not so. This assumption can be used because the energy demand of the pre-feed pump is relative to the main pump very small ($\approx 10\,\%$) and no actual data of the pre-feed pump is available. Furthermore, the efficiency (probably as function of mass flow working fluid) can be easily changed in the cycle model in the future.

Now that the pump model is explained in detail, the next chapter covers more information about the turbine simulations and the construction of the turbine map.

Chapter 4

Turbine

The cycle model uses an elaborate performance map to mimic the turbine response as function of inlet properties. From research done by Smit et al. [50] a mesh and initialised ANSYS CFX model is adapted in this research. The flow is modelled steady state. Some adjustments were made in place to optimise the setup files for the expected output of this thesis. In this chapter some further insights in how the simulations were setup and the validation of the simulation convergence.

4-1 Mesh

The turbine consist of 18 stator blades and 47 rotor blades. For the sake of computational time, only one stator stage and rotor blade are modelled. With periodicities, the flow through more stator and rotor blades is simulated. This is also mentioned in the next section. An overview of the mesh is shown in figure 4-1.

In this quasi 3-D model, only the flow of the mid line of the domain is solved in order to save computational time. Therefore the domain consist only of 2 elements in the z-direction. The boundary conditions is chosen as such that the follows the mid line and the walls are having the same speed as the flow in the mid line.

The height is chosen such that the path increases in height downstream to mimic the change in height in the real rotor.

Also the thickness of the rotor increases to account for fluid expansion in the rotor. This is shown in figure 4-2.

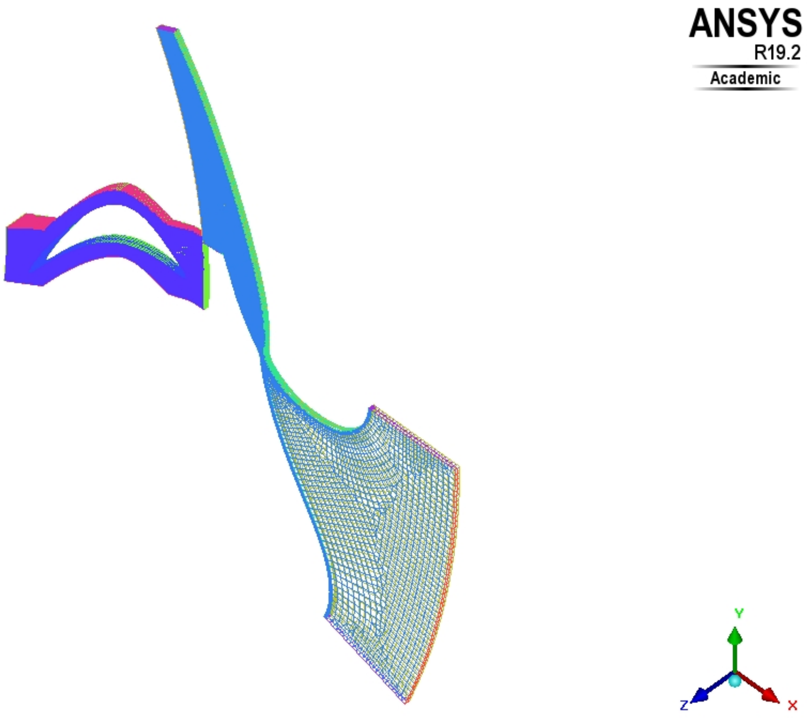

Figure 4-1: Isometric view of the mesh used for the turbine simulations

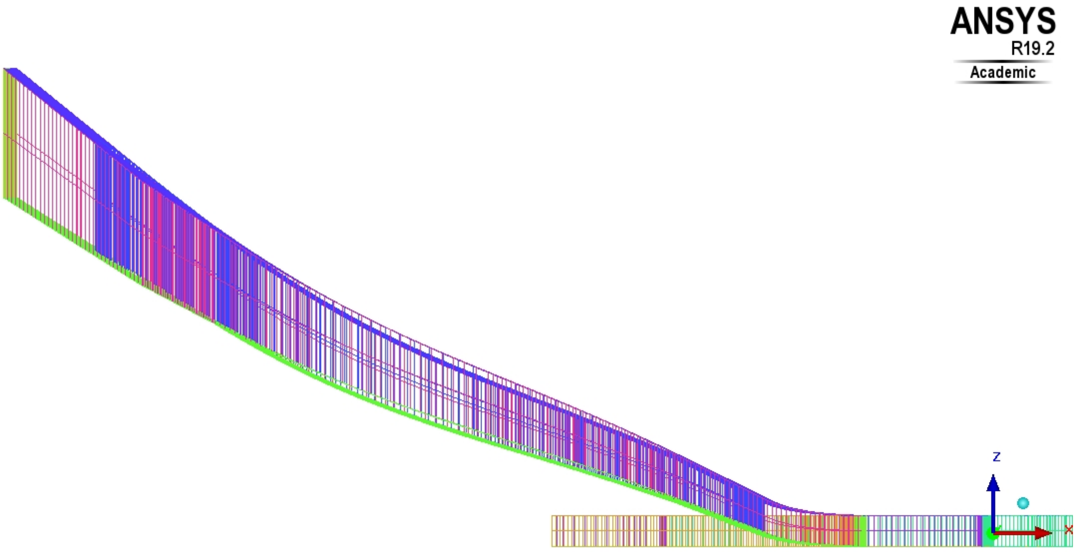

Figure 4-2: Zoomed in view of the mesh height used for the turbine simulations

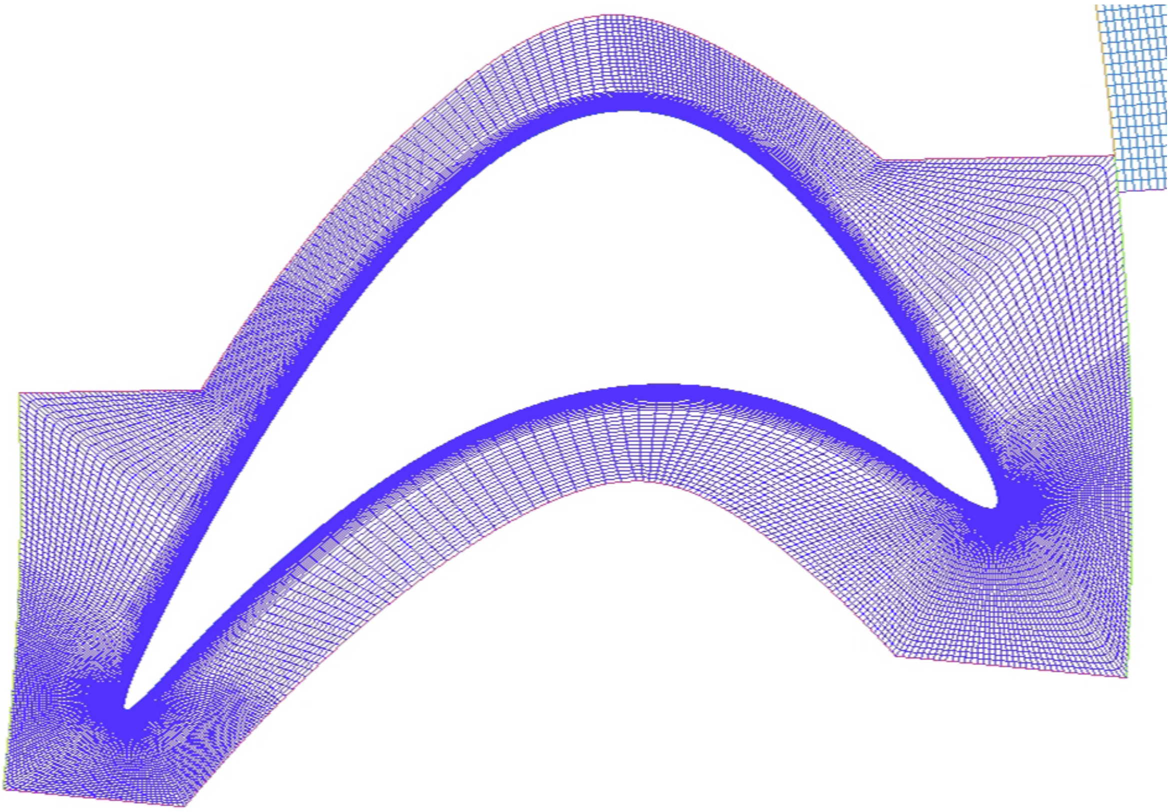

Figure 4-3: Zoomed in view on the mesh used for the turbine simulations

Location	Elements
Domain stator	38496
Blade stator	1138
Bottom stator	19248
Top stator	19248
Periodic stator side 1	162
Periodic stator side 2	162
Inlet stator	98
Mixing plane side 1	256
Rotor Domain	81840
Mixing plane side 2	202
Outlet rotor	206
Rotor blade	1240
Periodic rotor side 1	416
Periodic rotor side 2	416
Bottom rotor	40920
Top rotor	40920

Table 4-1: Number of elements per object

The total number of nodes in this mesh is 183468 and the mesh consist of several different element shapes, shown in table 4-2. The triangular and pentagonal shaped elements are solely from the stator because the rotor is a structured mesh which consist only of hexagonal and quadruple elements. A structured mesh has some advantages such as elements can be simply addressed by double indices. Also the connectivity of elements is straightforward. These advantages makes programming more easy [53].

Location	Elements
Hexagonal	119988
Triangle	348
Pentagonal	348
Quadrupal	124284

Table 4-2: Element type and amount

Now that the mesh is given and the geometry of the simulated domains are given, the next section will discuss initial settings of the simulations.

4-2 Initial values

The mesh discussed above is imported into ANSYS CFX PRE and some changes were made in order to achieve the best output for the cycle model as possible.

4-2-1 Boundary conditions

The geometry consist of 2 domains, one is the stator domain and the other is the rotor domain. Both domains have their assigned boundary conditions.

According to the theory solver guide of Ansys CFX , a no slip wall means that both the tangent component and the normal component to the wall is zero. For the free slip wall condition, the normal component is zero but the tangent velocity (the velocity along the direction of the flow) is the same as the flow velocity. This ensures that the fluid is not moving away from the mid line and that the wall imposes no friction as in reality it is another fluid flow.

The stator domain consist of an inlet where a total pressure and a total temperature is put. The total pressure can be computed similar to the total enthalpy (which is already discussed in 2-20);

$$p_{\text{tot}}{=}p_{\text{stat}} + \frac{\rho V^2}{2} \tag{4-1}$$

$$T_{\text{tot}}{=}T_{\text{stat}} + \frac{V^2}{2c_p} \tag{4-2}$$

There are four walls, one on the top, one on the bottom and two side walls which are in reality the stator blades. The top and bottom are free slip walls with no heat transfer (adiabatic). The stator blade walls are no slip walls also with no heat transfer. A part of the inlet and a part of the outlet of the stator consist of rotational periodic walls which mimics the next stator and rotor inlet and outlet. So the outlet of one side of the wall is the inlet of the other side of the wall. At the outlet of the stator, a mixing plane is placed where the condition of the flow is averaged of both stator outlet and rotor inlet. More information about the mixing plane is also given in subsection 4-2-5 and 4-2-3.

The rotor domain consist of a rotor blade, four walls and an inlet and outlet. The inlet of the rotor is the outlet of the stator and the flow is averaged there based on the both the outlet conditions of the stator and the inlet conditions of the rotor. The top and bottom of the rotor domain are free slip walls without heat transfer. These are free slip walls because the midline of the flow is studied. The boundary condition ensures that the flow is not leaving this midline. The two side walls are rotational periodic walls, the one outlet is the others inlet. The rotor blade is a no slip adiabatic wall. At the outlet of the rotor is a temperature of $T_{\text{t,out}} = 450\,\text{K} = 176.85\,°\text{C}$ applied.

4-2-2 Numerical order

The numerical order applied on the turbulence and advection scheme which is used is the second order method. In Ansys CFX it is also called ”High resolution”. This means that the local truncation error of numerical scheme to solve the integrations is $\leq \mathcal{O}(\Delta t^2)$ [57].

4-2-3 Frozen rotor

The frozen rotor option simply copies the solution of the outlet of the stator to the inlet of the rotor. The option is not used in the simulations, the goal of this research is to find the correct conditions at the outlet of the turbine, not to find the result at the mixing plane. The simulations used in this thesis average the profile at the outlet of the stator and the inlet of the rotor.

The change of this option made it more difficult to let the solution converge, especially at a high rotational speed. This is later on explained in section 4-3.

4-2-4 Viscous work

The simulations are done with the viscous work inside the flow taken into account. The viscous work is the energy which is added to the flow caused by viscous stresses.

4-2-5 Pressure profile decay

During the last simulations, as described above in sub section 4-2-3, the simulations were more difficult to converge because of the averaged solution at the mixing plane. A solution which solved the problem was to change the ”pressure profile decay” from 5% to 10%. This kind of relaxation technique means physically that a bigger part of the old solution is copied to the new situation.

4-2-6 Scalable wall function

To resolve the flow near the wall, a scalable wall function can be used in order to account for the shear stress as function of the distance from the wall and the flow velocity. The advantage of the scalable wall function is that it can also be used with fine meshes. This scalable wall function is not used in the simulations for this research because the y^+ values are small enough with respect to the mesh grid. The y^+ value is a dimensionless number which indicate the wall distance [39].

4-2-7 Initiating domains and stator inlet

The domains of the input values for the simulations have to be chosen very carefully. A too great distance between operating points can lead to unnecessary information and too small distance can mean there is not enough information in the domain.

A starting rotational speed of $n_{\text{start}} = 250\,\text{Hz}$ is chosen because the bearings can only work at a rotational speed of $n = 230\,\text{Hz}$ and the rotational speed has to keep away from this point. In the past is used $n = 500\,\text{Hz}$ as maximum rotational speed and to keep some overlap, a maximum of $n_{\text{max}} = 550\,\text{Hz}$ is chosen.

The question rose then which inlet pressures at the turbine fits belongs to these rotational speeds. This was difficult to assume without real turbine map and cycle at hand. From experiments done in the past by Stephan Smit, an educated guess was possible to compute the inlet pressures for different rotational speeds. These relations can be found in table 4-3.

Rotational speed, $[n] = \mathrm{Hz}$	**Inlet pressure,** $[p_{\mathrm{t,in}}] = \mathrm{bar}$
288	18.42
300	19.44
336	23.04
364	25.92
375	27

Table 4-3: Experimental data from Stephan Smit

A trend line was constructed by plotting the points of table 4-3 in MICROSOFT EXCEL . The formula which belongs to the trend line is displayed in equation 4-3. With $[n] = \mathrm{Hz}$ and $[p_{\mathrm{t,in}}] = \mathrm{bar}$.

$$p_{\mathrm{t,in}} = 0.1 \cdot n - 10.327 \tag{4-3}$$

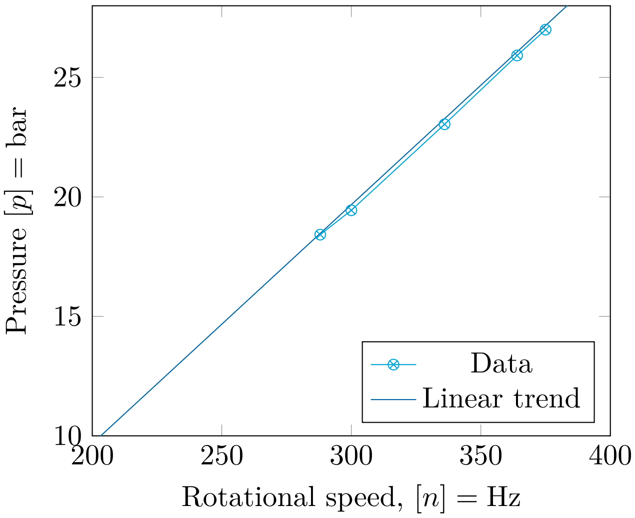

Figure 4-4: Data points from experiments of Stephan Smit to investigate the pressure / speed relation

Putting the rotational speed $n_{\mathrm{start}} = 250\,\mathrm{Hz}$ into the equation, the pressure which belongs to this rotational speed is $p_{\mathrm{start}} = 14.67\,\mathrm{bar} \approx 15\,\mathrm{bar}$. At the maximum rotational speed, this formula makes no sense, the critical pressure of toluene is $p_{\mathrm{crit,tol}} = 41.263\,\mathrm{bar}$ [31] so at the outcome of $p_{\mathrm{end}} = 45\,\mathrm{bar}$ the working fluid would be transcritical which is not the case in this system. An end pressure of $p_{\mathrm{end}} = 35\,\mathrm{bar}$ is chosen, which belongs to an evaporator heat input of $P_{\mathrm{evap,in}} = 1200\,\mathrm{kW}$ from one of the first versions of the cycle model.

An amount of 25 points for the simulations is chosen to get both enough data to build a turbine map of and not waste unnecessary computational time. The points were chosen even over both pressure and speed domains and are shown in figure 4-5.

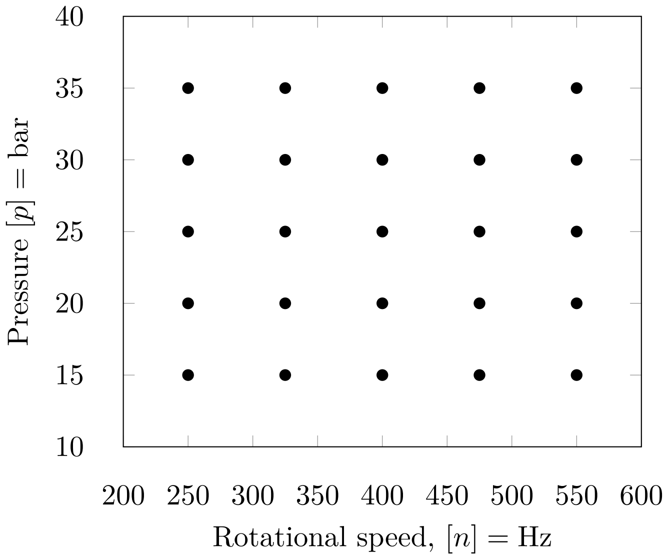

Figure 4-5: Suggestion of points to put into turbine simulation

The inlet temperatures necessary for the simulations were computed with the vaporisation temperature and the overheating of $\Delta T_{\text{overh,t,in}}$. The vaporisation data is found with COOLPROP [8].

$$T_{\text{t,in}} = T_{\text{t,in,sat}}(p_{\text{t,in}}) + \Delta T_{\text{overh,t,in}} \tag{4-4}$$

The turbine inlet temperatures as function of inlet pressures are shown in figure 4-6.

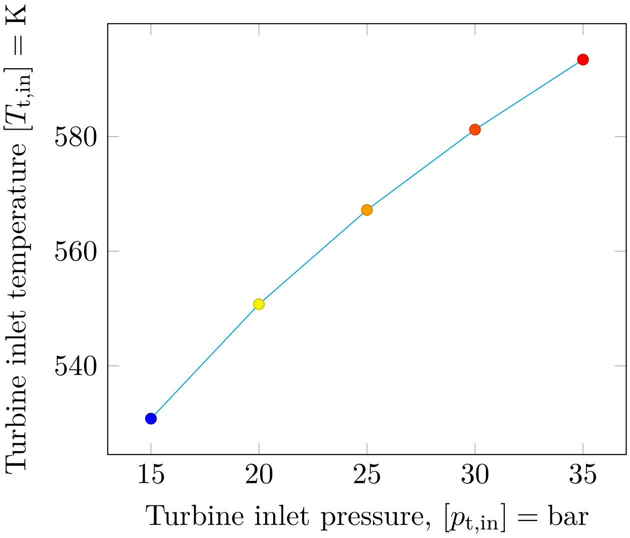

Figure 4-6: Turbine inlet temperatures which belongs to certain inlet pressures

This information, the rotational speeds, the inlet pressures with inlet temperatures serve as initial values for the rotor and the stator domains. These inputs are also used for the stator inlet boundary condition.

4-2-8 Turbulence model

The turbulence model which are used for the simulations is the Spalart Allmaras model. This model is chosen because it has the best convergence behaviour during the first runs of the simulation. It is a one equation model which is constructed for use in aerodynamics.

4-2-9 Time stepping

After all initial settings of the solver input file are defined, the first run of the simulations can be started. The physical time step used to let the solution converge is $\Delta t = 1 \times 10^{-6}\,\mathrm{s}$. More information on convergence will be given in the next section.

4-3 Convergence

During the simulations, statistics of the computations are given in order to act on specific simulation conditions and stop the simulations when the simulations are complete.

The convergence is the rate at which the simulation reaches a steady state and can be defined as finished. The ANSYS CFX solver guide recommends a residual value of $R_{\mathrm{RMS}} < 1 \times 10^{-4}\,\%$, it mentions $R_{\mathrm{RMS}} < 1 \times 10^{-5}\,\%$ sufficient for most engineering purposes and $R_{\mathrm{RMS}} < 1 \times 10^{-6}\,\%$ only necessary for particularly sensitive geometries. The simulations which use rotational speed $n = 250\,\mathrm{Hz}$ to $475\,\mathrm{Hz}$ converged well enough within the $R_{\mathrm{RMS}} < 1 \times 10^{-4}\,\%$ range. This can be seen in figure 4-7.

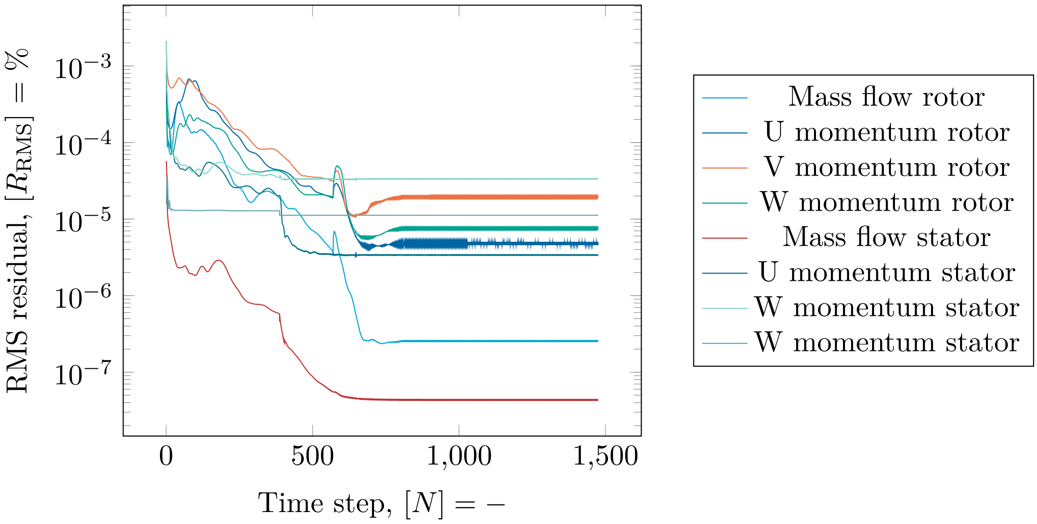

Figure 4-7: RMS residual

Another important variable to measure the convergence of the simulation is the imbalance of the mass flow and energy inside the domains M. When the imbalance is small, it means that the amount of energy or mass inside the control volume is not changing very much between the time steps. The ANSYS CFX solver guide assumes that if the imbalance $M < 0.01\,\%$, the simulation is converged. The imbalance during the simulation of the $p_{\mathrm{t,in}} = 15\,\mathrm{bar}$ and $n = 400\,\mathrm{Hz}$ case is shown in figure 4-8 and indeed shows that this convergence measure is reached.

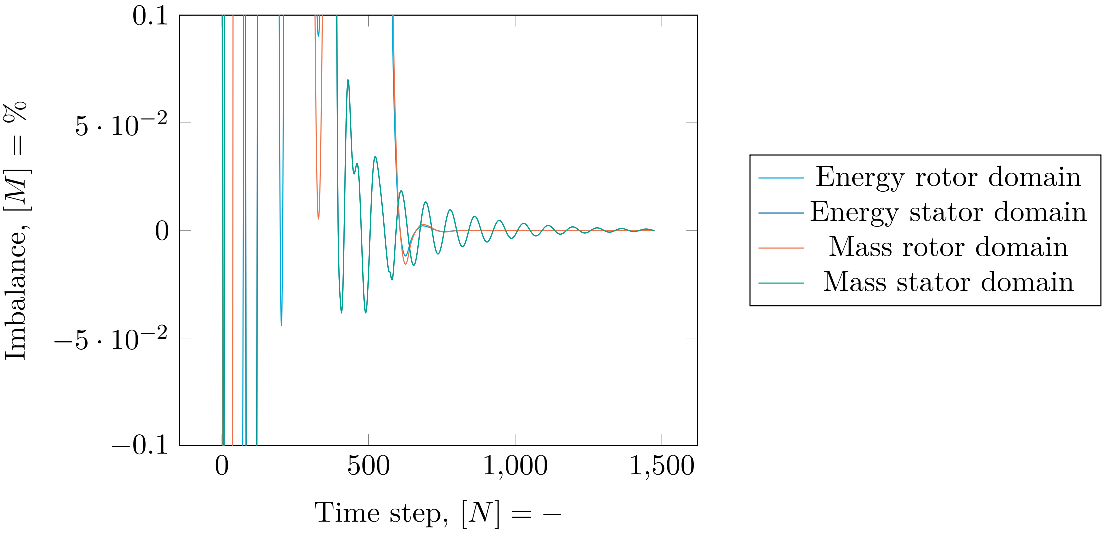

Figure 4-8: Imbalance for solving the simulation with boundary values $p_{\mathrm{t,in}} = 15\,\mathrm{bar}$ and $n = 400\,\mathrm{Hz}$

Another important measure to ensure a converged simulation is the mass flow of the control volume, which has to remain equal between the time steps in order to ensure the simulation is correct. In figure 4-9 the mass flow during the simulations for both rotor and stator domain is shown. Of course the stator inlet mass flow must be equal but opposite sign as the stator outlet and the same holds for the rotor domain.

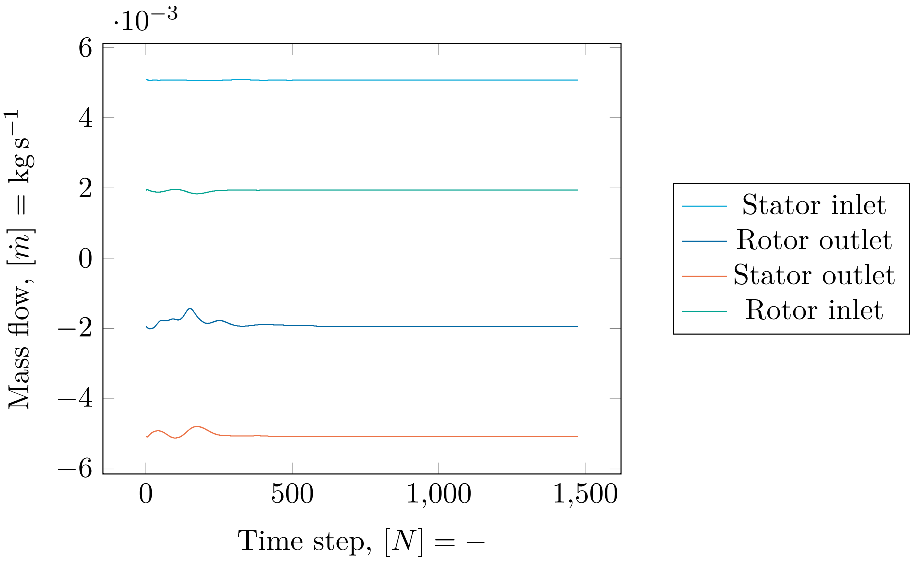

Figure 4-9: Mass flow for certain simulation time steps for the $n = 400\,\mathrm{Hz}$ case

The simulations at $n = 550\,\mathrm{Hz}$ are more difficult to converge. As can be seen in figure 4-10, the RMS residual is slightly above $R_{\mathrm{RMS}} = 1 \times 10^{-4}\,\%$. The variable is also oscillating in time, which is not the case for the $p_{\mathrm{t,in}} = 15\,\mathrm{bar}$ and $n = 400\,\mathrm{Hz}$ case.

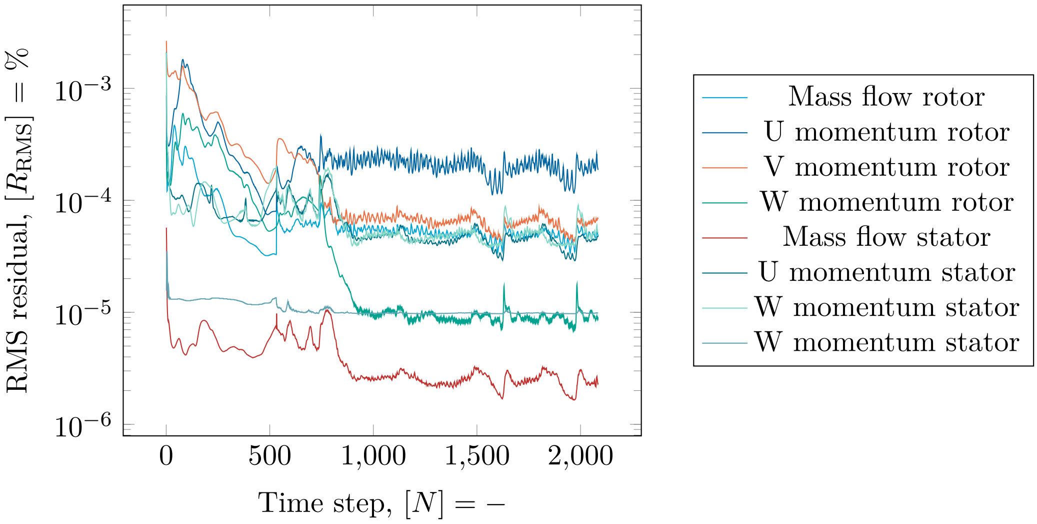

Figure 4-10: RMS residual for different time steps during the simulation of the $p_{\mathrm{t,in}} = 15\,\mathrm{bar}$ and $n = 550\,\mathrm{Hz}$ case

The convergence criteria which might be the most disturbed is the imbalance of the energy and the mass inside the control volume. The imbalance is oscillating between values of $M = 0.05\,\%$ to $0.1\,\%$ with maximum values of $M = 0.4\,\%$. The residual value and imbalance value oscillations are periodic.

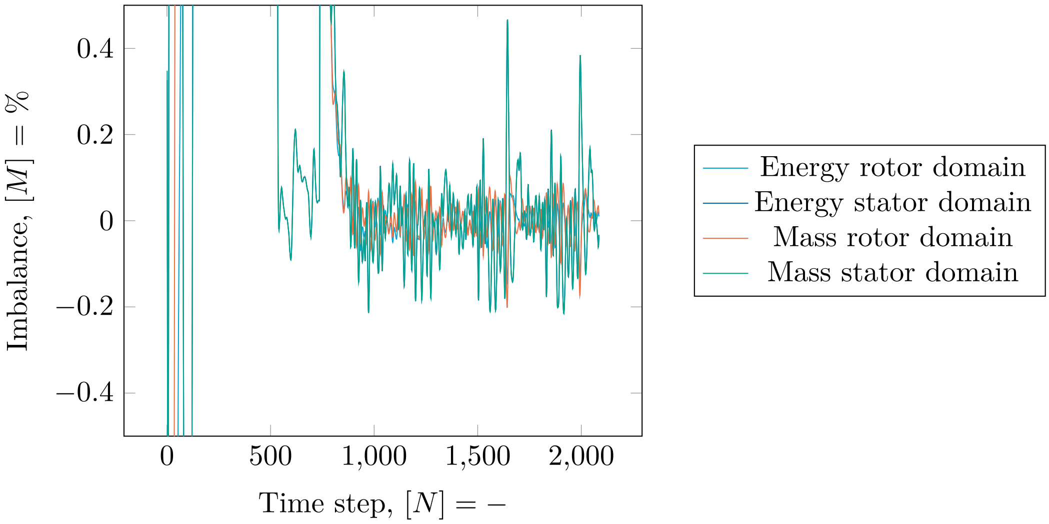

Figure 4-11: Imbalance for the solving of simulation with boundary values $p_{\mathrm{t,in}} = 15\,\mathrm{bar}$ and $n = 550\,\mathrm{Hz}$

The reason that the simulation is hard to converge might be that the flow at the rotor inlet is very turbulent due to a very different inlet angle than that of the rotor. The residuals of this simulation are too high to trust the solution of the flow field. Also the high imbalance is a reason to doubt this solution.

In order to be confident about the optimal rotational speed, an extra five simulations are done. The turbine inlet pressures were chosen the same as in section 4-2-7 described, but now with rotational speed $n = 500\,\mathrm{Hz}$. These simulations converge similar to those with low rotational speeds with $R_{\mathrm{RMS}} < 1 \times 10^{-4}\,\%$, $R < 0.001\,\%$ and the flow stable during the time steps. The results of the extra simulations are taken into account later in chapter 5 in order to have a good estimation of the flow field.

4-4 Enthalpy model

The enthalpy model of simulation software can differ from the enthalpy model which is used for fluid property packages such as REFPROP [31] or CoolProp [8]. For the fluid properties which are used in the simulations in this thesis, CoolProp data is converted to a RPG file. Enthalpies and entropies are both verified with in the simulation software (the inlet entropy and enthalpy are based in the inlet pressure and temperature) and with the fluid property software REFPROP and are compared as described in the equation below:

$$\frac{\Delta h}{h} = \frac{h_{\mathrm{rp}} - h_{\mathrm{model}}}{h_{\mathrm{model}}} \tag{4-5}$$

$$\frac{\Delta s}{s} = \frac{s_{\mathrm{rp}} - s_{\mathrm{model}}}{s_{\mathrm{model}}} \tag{4-6}$$

The outcomes of the comparison are shown in figure 4-12. As can be seen in this figure, the difference of the model is less than 0.01 % which is assumed to be small enough. This difference is higher than the comparison between REFPROP and CoolProp enthalpy model in section A. This can be explained either by round-off errors or interpolation differences.

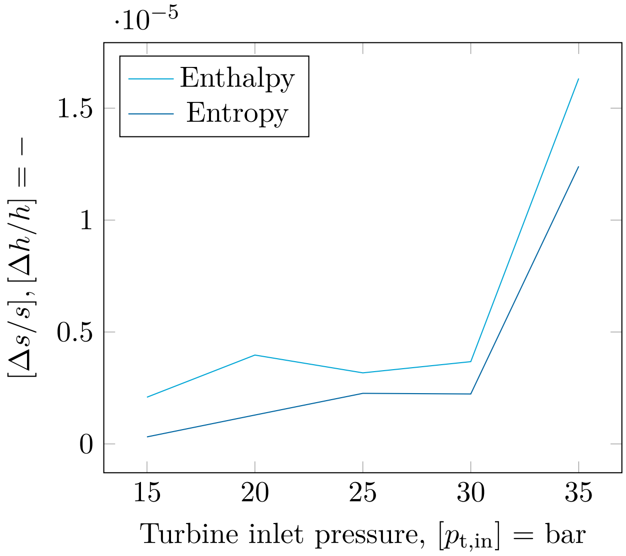

Figure 4-12: Relative difference between simulation software enthalpy and entropy model and the REFPROP enthalpy and entropy model

4-5 Diffuser

We assumed at the outlet of the turbine, that the diffuser is ideal so that the entropy over the diffuser stays constant. Usually the diffuser converts some part of the kinetic energy of the working fluid into static pressure so that static pressure before the recuperator and condenser is higher. This is necessary to overcome the frictional pressure losses in the recuperator and the condenser. In the Triogen cycle, the outlet of the turbine is directly placed above the recuperator heat exchanger. Thus the diffuser consist of a fast change in geometry, rapidly decreasing the velocity of the gas when entering the recuperator.

The entropy at the outlet of the turbine can be extracted from the simulations and is approached by the following formula ($s_{\mathrm{t,out}}(p_{\mathrm{t,in}}, n)$ instead of $z(x, y)$ with $[s_{\mathrm{t,out}}] = \mathrm{kJ} \cdot \mathrm{kg}^{-1} \cdot \mathrm{K}^{-1}$, $[n] = \mathrm{Hz}$ and $[p_{\mathrm{t,in}}] = \mathrm{bar}$):

$$z(x, y) = K_1 + K_2 x + K_3 y + K_4 x^2 + K_5 xy + K_6 y^2 + K_7 x^2 y + K_8 xy^2 + K_9 y^3 \qquad (4\text{-}7)$$

with the following parameters:

i	1	2	3	4	5	6	7	8	9
K	1.0641	6.1119×10^{-3}	1.5743×10^{-3}	-1.2286×10^{-4}	2.2934×10^{-5}	-6.6616×10^{-6}	-4.9898e-08	-2.3165e-08	7.2346e-09

Table 4-4: Parameters for the estimation of the turbine outlet entropy from the simulations

The linear estimation is done by MATLAB with the function ”Poly23” of a linear curve fitting function. The proportion of variance $\mathcal{R}^2 = 0.99741$ which makes the estimation accurate. The results compared with the outcomes of the simulations can be seen in figure 4-13. This results are used as input data for the cycle model. A small deviation in the turbine outlet

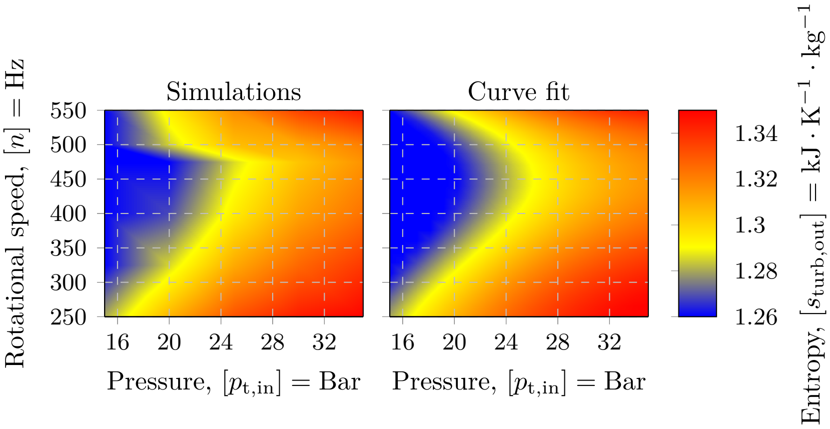

Figure 4-13: Entropy at turbine outlet from simulations and given by equation 4-7

entropy can mean a big difference in the estimated throttle behaviour hence precision and quality of the entropy estimation is necessary. A too coarse estimation of the entropy can ultimately lead to a diverging model. Diverging means that the model is iterating away from the solution and that the solution will explode.

Important is how reliable this method is. We assumed an ideal diffuser and the outlet pressure of the diffuser is assumed as the pressure inside the condenser and the pressure difference between the condenser and the turbine.

In table 2-1 the pressure drops per part are presented as they are used in the cycle model. The pressure at the inlet of the hot side of the recuperator can be computed as such: $p_{\mathrm{rec,in}} = p_{\mathrm{cond,in}} + \Delta p_{\mathrm{rec,hot}}$.

With this pressure and the entropy at the outlet of the turbine, the static enthalpy can be verified with the properties from [31], which are put into tables for computation efficiency. So $h_{\mathrm{rec,in,stat}} = f(s_{\mathrm{t,out}}, p_{\mathrm{rec,in}})$.

The total enthalpy at the outlet of the turbine ($h_{\mathrm{t,out,tot}}$) can also be extracted from the turbine simulations. For convenience, the formula 4-7 can be used to estimate the total outlet enthalpy as function of rotational speed and turbine inlet pressure, with $z(x, y)$ as $h_{\mathrm{t,out,tot}}(p_{\mathrm{t,in}}, n)$. The proportion of variance $\mathcal{R}^2 = 0.99959$ and the output unit is $[h_{\mathrm{t,out,tot}}] = \mathrm{kJ \cdot kg^{-1}}$, the input units $[p_{\mathrm{t,in}}] = \mathrm{bar}$ and $[n] = \mathrm{Hz}$.

with parameters

i	1	2	3	4	5	6	7	8	9
K	3.5260×10^{2}	8.9018	5.6040×10^{-1}	-1.0129×10^{-1}	-6.7873×10^{-3}	-2.7210×10^{-3}	1.3233×10^{-4}	-1.8719×10^{-6}	3.2533×10^{-6}

Table 4-5: Parameters for the estimation of the turbine total outlet enthalpy from the simulations

The stagnation or total enthalpy is the static enthalpy plus the energy which will be released when the fluid would be put at rest (already discussed in section 2-9, equation 2-20):

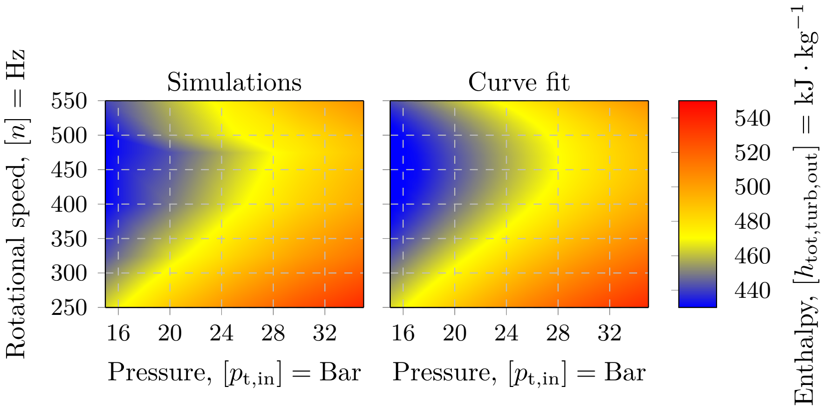

Figure 4-14: Enthalpy at turbine outlet from simulations and given by equation 4-7

$$h_{\mathrm{tot}} = h_{\mathrm{stat}} + \frac{V^2}{2} \tag{4-8}$$

$$V = \sqrt{2(h_{\mathrm{tot}} - h_{\mathrm{stat}})} \tag{4-9}$$

With $[h] = \mathrm{J} \cdot \mathrm{kg}^{-1}$

Now that we found the theoretical velocity of the working fluid when entering the recuperator, the method can be validated. If the velocity would be too high, the method described above would not be valid. Triogen was not able to give a certain velocity but assumed $20\,\mathrm{m} \cdot \mathrm{s}^{-1}$ to $35\,\mathrm{m} \cdot \mathrm{s}^{-1}$. In figure 4-15 the velocities for different inlet powers are displayed.

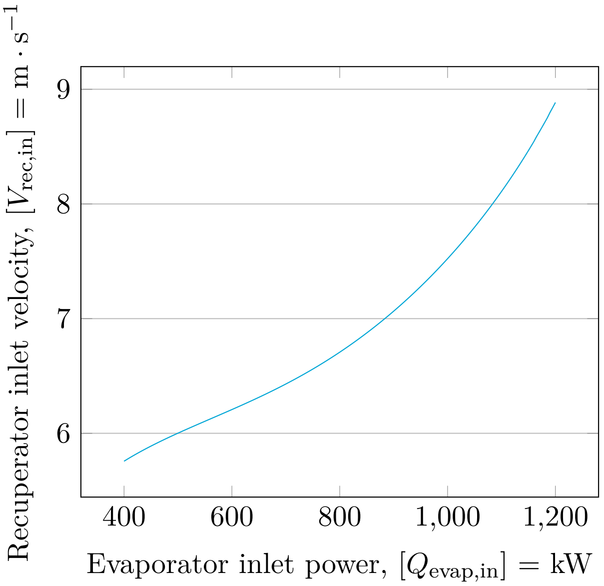

Figure 4-15: Recuperator inlet velocity based in turbine outlet total enthalpy, entropy and model recuperator inlet pressure

As can be seen in figure 4-15, the velocity is below the range discussed above, thus it is clear that this method is valid.

4-6 Cycle implementation

The input for the turbine map from the cycle model is a rotational speed n and the turbine inlet pressure $p_{\mathrm{t,in}}$. As mentioned in the previous section 4-5, the outlet of the turbine map is solely an outlet entropy. Because the outlet pressure is defined in the cycle model, all conditions at the turbine outlet are known.

A detailed explanation of the cycle model is given in chapter 2, more information about the input of the pump model and the turbine map is given in respectively chapter 3 and chapter 4. This is the basis of the method of this research project. In the next chapter the results of the pump model, the turbine map is given. These results serve as input for the cycle model. After these results an elaborate review on the cycle model results is given.

Chapter 5

Results

This chapter includes the outcomes of the pump model, the results of the turbine simulations, a detailed qualitative analysis of the turbine simulations and eventually the results of the cycle model, given an optimal rotational speed.

5-1 Pump

In this section some results of the pump model, which is used as input for the cycle model, are shown. The pressure ratio increases as the rotational speed increases. This is as expected because a higher rotational speed means a higher pressure difference. This is also shown in section 3-2.

In figure 5-1 the pressure ratio as function of the rotational speeds is shown.

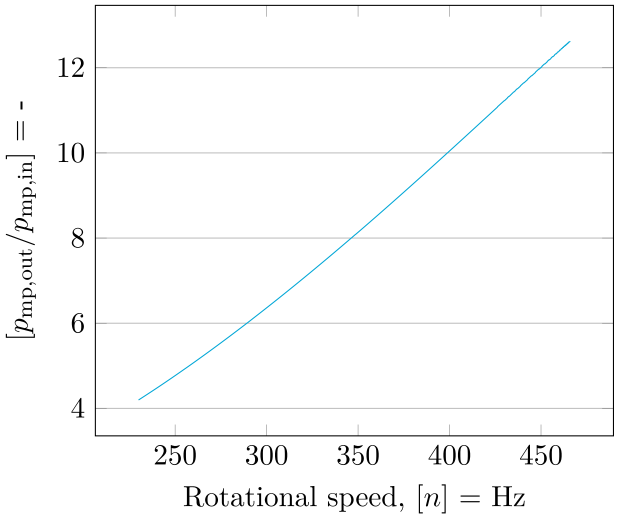

Figure 5-1: Pressure ratio induced by the main pump as function of the rotational speed

The power consumption and power output of the main pump operating in design conditions is shown in figure 5-2. The power input is given both as total and in separate parts of a friction part and a velocity part. From the figure it is apparent that the friction part is only a small fraction of the total power consumption.

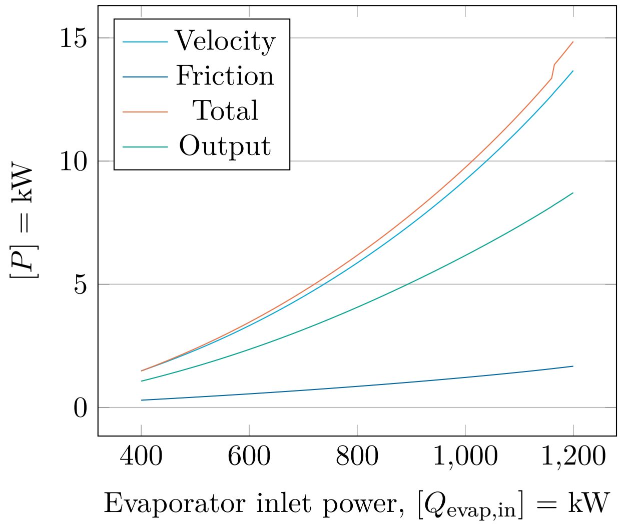

Figure 5-2: Power consumption and power output of the main pump

The power consumption and power output increase with the third power of the evaporator heat input $Q_{\mathrm{evap,in}}$ as can be seen in the figure above 5-2. This is because the power consumption of velocity and the power output are both a function of the mass flow and the square of the rotational speed. These increase both linearly.

5-2 Turbine

In this chapter the results of the turbine simulations will be shown and some qualitative analysis is given in order to verify the results of the simulations.

The first section shows the velocity plots and streamline plots, the second displays the temperature along the flow profile, the third section discusses the eddy viscosity, the fourth shows the enthalpy difference, the fifth section looks at efficiencies and the last section shows the outflow losses.

5-3 Velocity fields

From the simulations of the turbine wheel in Ansys CFX , some qualitative analysis can be done in order to check the results on correctness and have some idea of the fluid properties throughout the turbine.

Directly after the simulations are completed, the velocity plots of the flow can be extracted. This section shows the first impressions of the simulations.

5-3-1 Velocity plots

The relative velocity of the flow is shown in figure 5-3. As can be seen in this figure, a step in relative velocity at the mixing plane is visible. The wheel has a velocity of $nD\pi$. At a high rotational speed, the relative flow velocity is small because the velocity of the turbine wheel is higher. This difference can be seen between figure 5-3a and figure 5-3c.

When the rotational speed of the wheel is low, $n = 250\,\mathrm{Hz}$, the relative velocity behind the rotor is locally very low. This can be caused by the high inlet angle hitting the rotor blade. The flow definitely can not follow the blade correctly. Also a large wake at the trailing edge of the rotor blade is visible.

At high rotational speeds, $n = 550\,\mathrm{Hz}$, the relative flow velocity at the front of the rotor blade is locally lower. This can mean that the flow follows the back of the blade correctly but the inlet angle is too low and the flow separates from the blade at the front.

As can be seen in figure 5-3e, there is only a small area at the leading edge of the rotor where the flow hits the blade and the relative velocity is low. But the flow can follow the blade correctly and does not show wakes in front or at the back of the rotor.

5-3-2 Streamlines and pressure

To have a clear and first impression of the inlet angle of the flow, the streamlines of the flow are visible in figures 5-4 and 5-5. The absolute pressure of the flow is also displayed.

The streamline is defined by Kundu [28] as follows:

> ”A streamline is a curve that is instantaneously tangent to the fluid velocity throughout the flow field. In unsteady flows the streamline pattern changes with time.”

The flow is steady as stated in 4, thus the streamlines are fixed in time. The fluid velocity is a vector, a quantity with both a magnitude and a direction. The direction of this vector defines the curve of the streamline.

As can be seen in figure 5-4d there is a pressure build up at the back of the stator blade, which might be a result of the shockwaves induced by the previous stator blade. This is better visible at large inlet pressure $p_{\mathrm{t,in}}$ as the velocity and the mass flow are higher (due to the choked flow condition).

An artificial reflection of shockwaves can be identified on figure 5-4d. The shockwaves induced by the trailing edge of the stator blades is reflected at the wall of the stator blade but also reflected at the mixing plane. In reality, the shockwaves can not be reflected by the mixing plane. This numerically introduced reflection is unwanted but unavoidable with the simulation software used in this thesis. The non-reflective boundary condition is not available in ANSYS CFX .

For the rotor blades, the same as stated in subsection 5-3-1 is visible. At low rotational speed n, the flow cannot follow the blade at the back of the rotor due to a too high inlet angle. There is a wake visible and because the flow is ”pressed” against the next blade, the pressure is increased locally at the front of the blade.

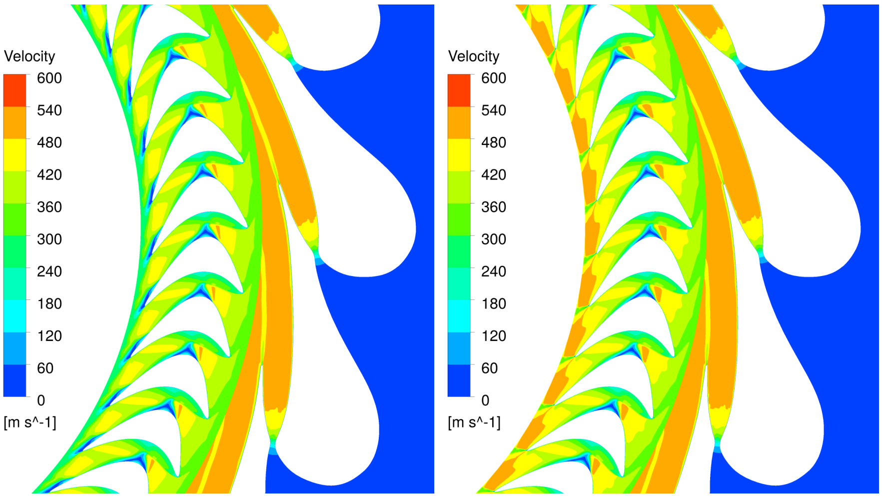

(a) $p_{\mathrm{t,in}} = 15\,\mathrm{bar},\ n = 250\,\mathrm{Hz}$ **(b)** $p_{\mathrm{t,in}} = 35\,\mathrm{bar},\ n = 250\,\mathrm{Hz}$

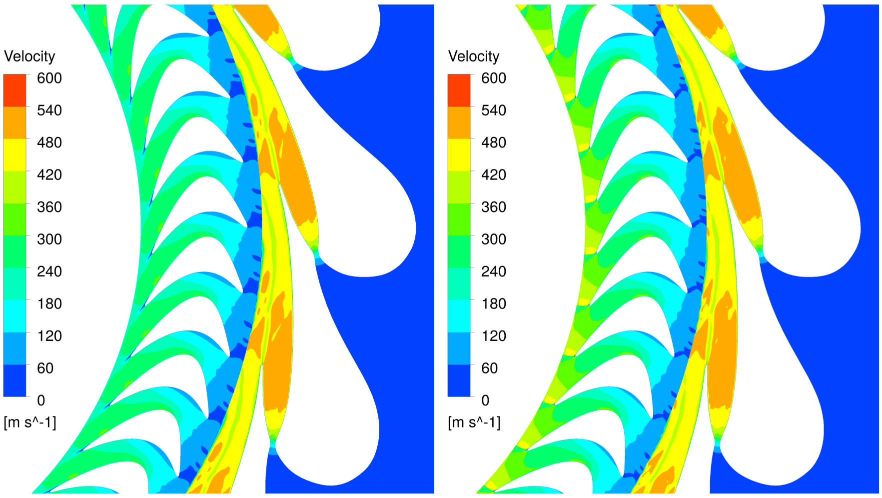

(c) $p_{\mathrm{t,in}} = 15\,\mathrm{bar},\ n = 550\,\mathrm{Hz}$ **(d)** $p_{\mathrm{t,in}} = 35\,\mathrm{bar},\ n = 550\,\mathrm{Hz}$

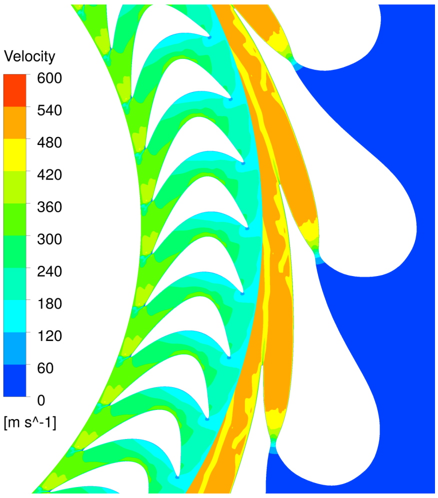

(e) $p_{\mathrm{t,in}} = 25\,\mathrm{bar},\ n = 475\,\mathrm{Hz}$

Figure 5-3: Relative velocity plots

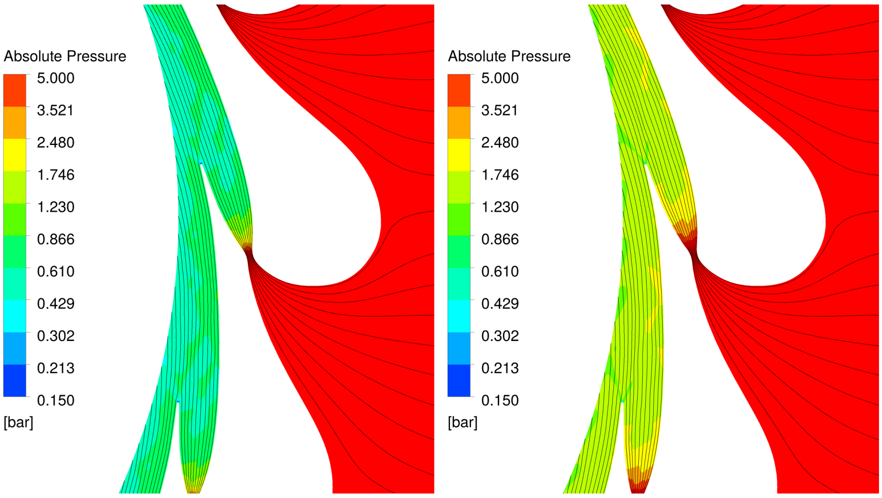

(a) $p_{\mathrm{t,in}} = 15\,\mathrm{bar},\ n = 250\,\mathrm{Hz}$ **(b)** $p_{\mathrm{t,in}} = 35\,\mathrm{bar},\ n = 250\,\mathrm{Hz}$

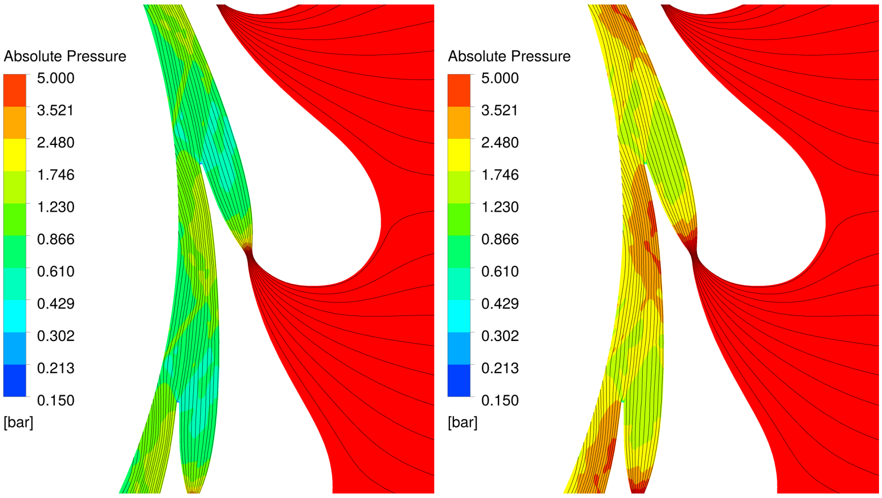

(c) $p_{\mathrm{t,in}} = 15\,\mathrm{bar},\ n = 550\,\mathrm{Hz}$ **(d)** $p_{\mathrm{t,in}} = 35\,\mathrm{bar},\ n = 550\,\mathrm{Hz}$

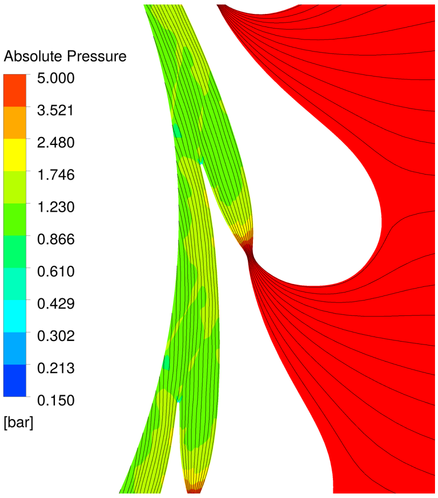

(e) $p_{\mathrm{t,in}} = 25\,\mathrm{bar},\ n = 475\,\mathrm{Hz}$

Figure 5-4: Streamlines stator

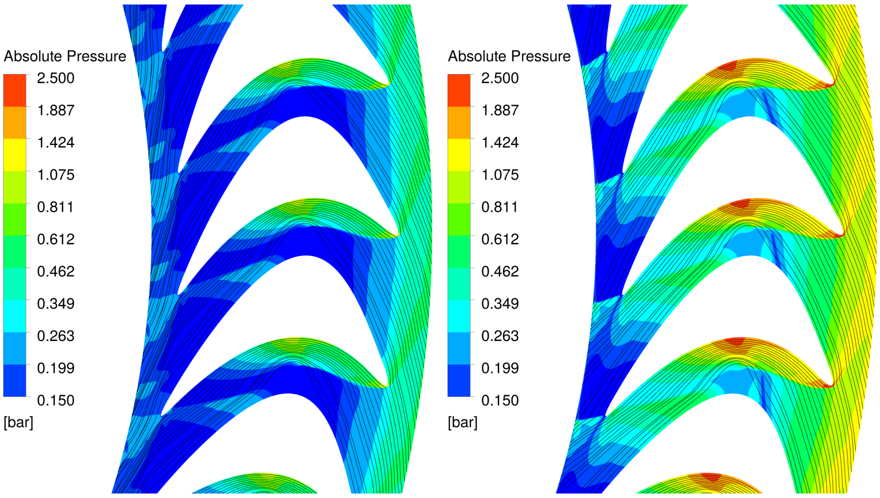

(a) $p_{\mathrm{t,in}} = 15\,\mathrm{bar},\ n = 250\,\mathrm{Hz}$ **(b)** $p_{\mathrm{t,in}} = 35\,\mathrm{bar},\ n = 250\,\mathrm{Hz}$

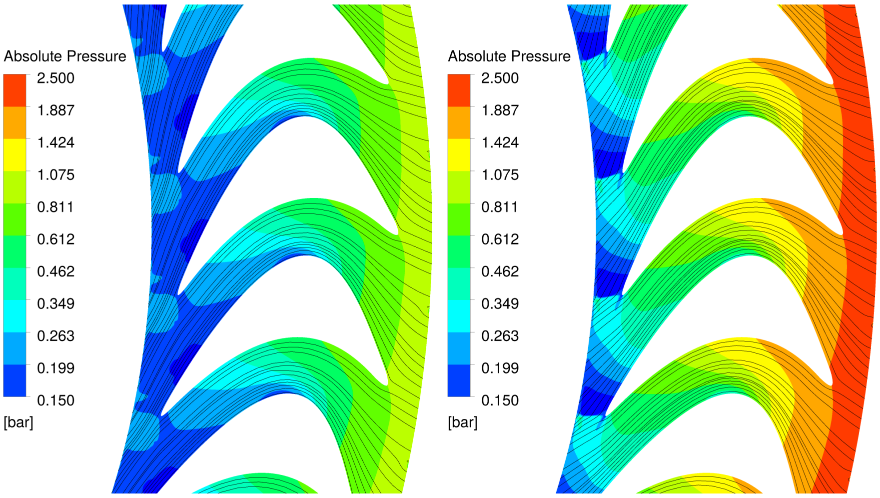

(c) $p_{\mathrm{t,in}} = 15\,\mathrm{bar},\ n = 550\,\mathrm{Hz}$ **(d)** $p_{\mathrm{t,in}} = 35\,\mathrm{bar},\ n = 550\,\mathrm{Hz}$

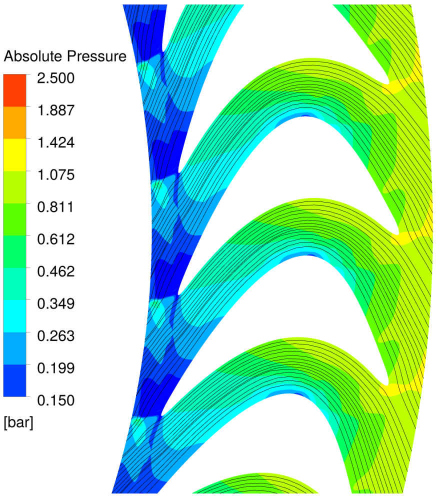

(e) $p_{\mathrm{t,in}} = 25\,\mathrm{bar},\ n = 475\,\mathrm{Hz}$

Figure 5-5: Streamlines rotor

Next subsection will give some more details from graphs which are also directly available from the Ansys CFX Post software.

5-3-3 Temperature

Previous subsection briefly touched the first output of the turbine simulations. This section also uses graphs straight from the Ansys CFX Post software and displays the temperature at different places in the domains.

In figure 5-6, for the lowest and the highest boundary values, the temperature along the stator and rotor are given. As described in 4-2, the walls of the stator, the bottom, the top and the walls of the rotor are adiabatic. In other words, they are ideally insulated thus not cooling or heating the working fluid as it travels through the turbine.

The fluid mainly cools down during its travel through the turbine. At the inlet, before the stator nozzle, the working fluid is at a high pressure. During the expansion after the nozzle, the temperature rapidly decreases because the adiabatic expansion process.

Heat is generated at walls where friction heats up the fluid particles. This is a cause of the viscous stresses introduced by the viscous work (discussed in 4-2-4). This is best visible in figures 5-6b and 5-6d. At higher turbine inlet pressures $p_{\mathrm{t,in}}$, the flow speed is higher thus the friction near the walls is higher.

Next subsection discusses the eddy viscosity in the flow field.

5-3-4 Eddy viscosity

Above, the temperature field in the turbine wheel is displayed and analysed. In this subsection another graph, which comes straight from the simulation software, is discussed.

The eddy viscosity mimics the interaction between the bulk flow and the small eddies which are caused by turbulence in the fluid. An extra momentum is added with a property that is similar to the viscosity of the flow: the eddy viscosity.

In figure 5-7, the eddy viscosity is plotted along the flow in the turbine wheel. At places with relative a large number of eddies, a high degree of turbulent flow is present.

As can be seen in the figures in 5-7, a high eddy viscosity is present after the flow is is released from the blades. A turbulent wake is causing major turbulent eddies after the flow has left the rotor and stator blades.

From the next section onwards, results which are derived from the data of the simulations are shown. These will include some minor calculation steps.

5-3-5 Velocity triangles

Previous subsections elaborated on some graphs which came straight from Ansys CFX Post . In this subsection the results are used to give an in-depth explanation of the verification of the results and the optimal rotational speed.

In order to verify the total enthalpy difference for the optimal rotational speed, velocity triangles are constructed. These triangles give some insight in the behaviour of the flow when

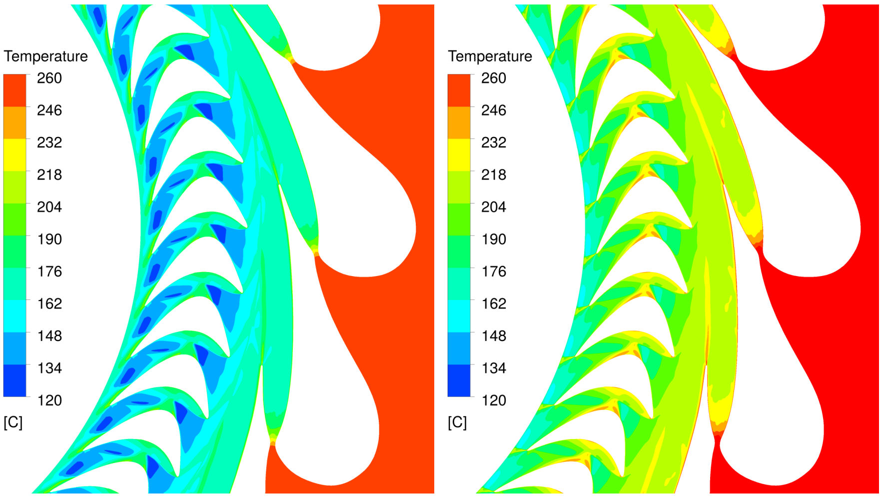

(a) $p_{\mathrm{t,in}} = 15\,\mathrm{bar},\ n = 250\,\mathrm{Hz}$ **(b)** $p_{\mathrm{t,in}} = 35\,\mathrm{bar},\ n = 250\,\mathrm{Hz}$

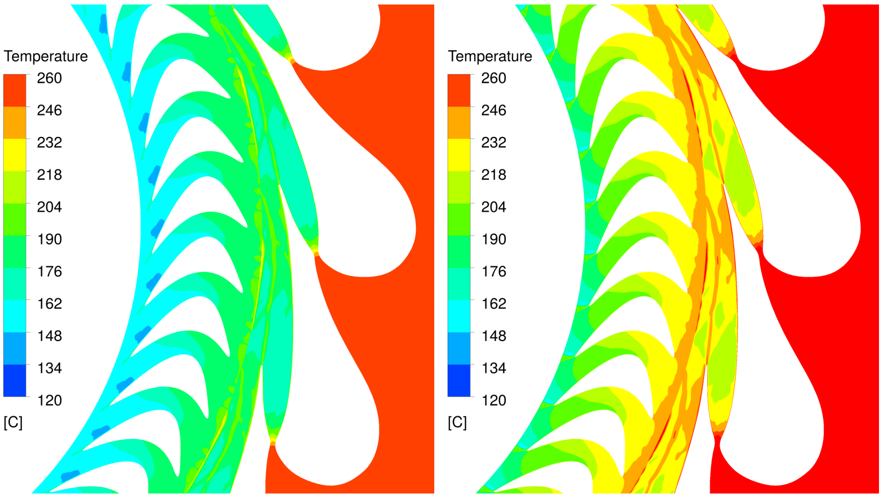

(c) $p_{\mathrm{t,in}} = 15\,\mathrm{bar},\ n = 550\,\mathrm{Hz}$ **(d)** $p_{\mathrm{t,in}} = 35\,\mathrm{bar},\ n = 550\,\mathrm{Hz}$

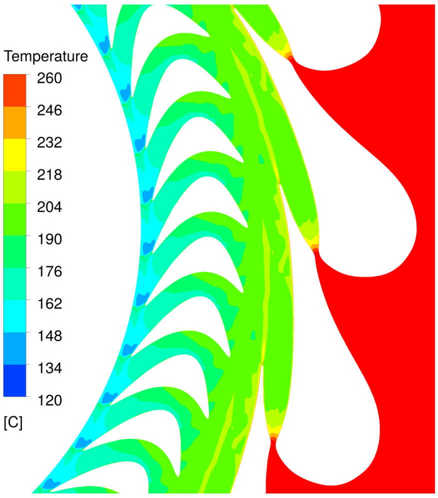

(e) $p_{\mathrm{t,in}} = 25\,\mathrm{bar},\ n = 475\,\mathrm{Hz}$

Figure 5-6: Temperature

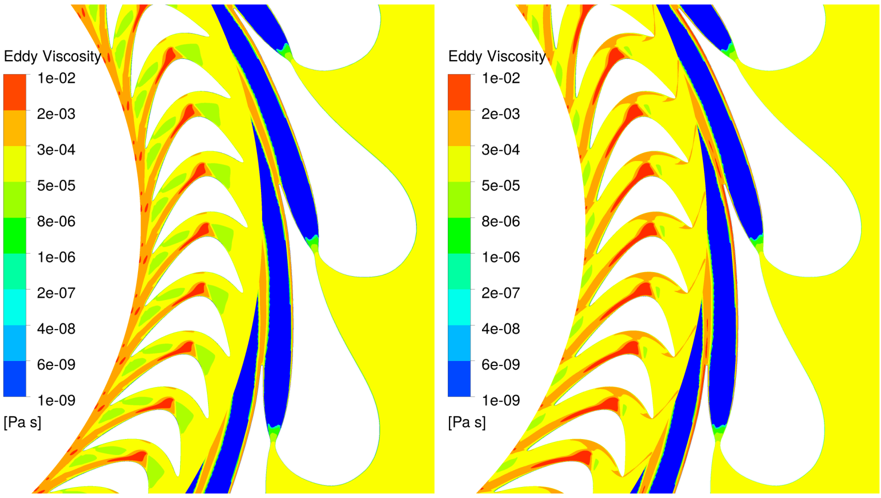

(a) $p_{\mathrm{t,in}} = 15\,\mathrm{bar},\ n = 250\,\mathrm{Hz}$ **(b)** $p_{\mathrm{t,in}} = 35\,\mathrm{bar},\ n = 250\,\mathrm{Hz}$

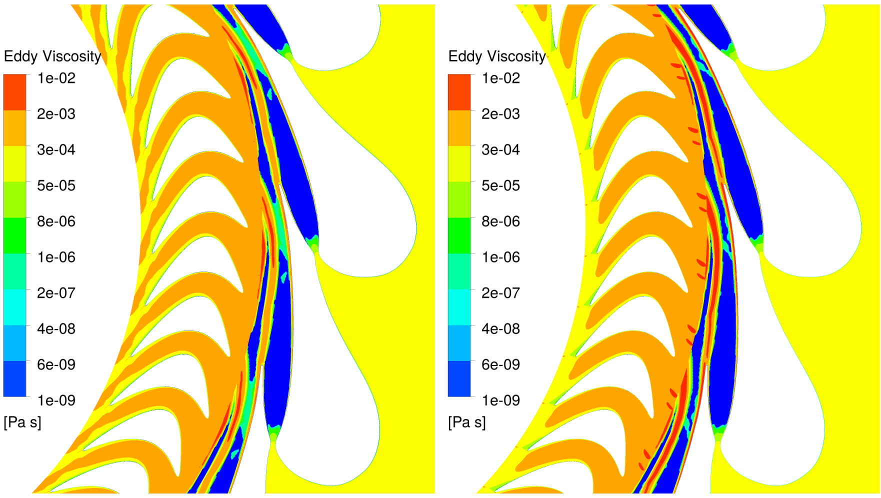

(c) $p_{\mathrm{t,in}} = 15\,\mathrm{bar},\ n = 550\,\mathrm{Hz}$ **(d)** $p_{\mathrm{t,in}} = 35\,\mathrm{bar},\ n = 550\,\mathrm{Hz}$

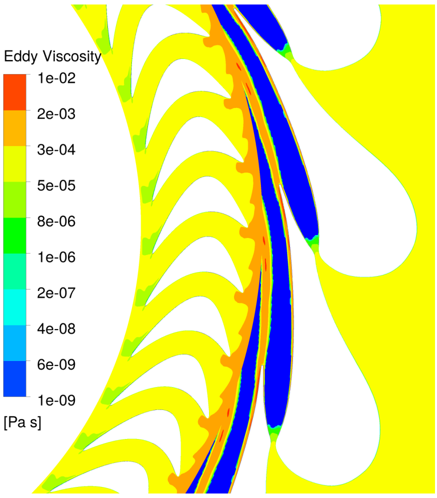

(e) $p_{\mathrm{t,in}} = 25\,\mathrm{bar},\ n = 475\,\mathrm{Hz}$

Figure 5-7: Eddy viscosity

it enters the rotor blade.

In ANSYS CFX both absolute velocities u_x and u_y from the vector $\boldsymbol{u}$ and the unit vector components $\hat{e}_{\boldsymbol{u}_x,\theta}$, $\hat{e}_{\boldsymbol{u}_y,\theta}$, $\hat{e}_{\boldsymbol{u}_x,r}$ and $\hat{e}_{\boldsymbol{u}_y,r}$ are defined. These unit vectors represent the part of the velocity component in a certain direction. For example, $\hat{e}_{\boldsymbol{u}_x,\theta}$ gives the part of x velocity component in the tangential direction.

The stator outlet angle, rotor inlet angle is defined as such

$$\alpha_2 = \arctan\left(\frac{(\boldsymbol{u}_x\hat{e}_{u_x,\theta} + \boldsymbol{u}_y\hat{e}_{\boldsymbol{u}_y,\theta})}{(\boldsymbol{u}_x\hat{e}_{\boldsymbol{u}_x,r} + \boldsymbol{u}_y\hat{e}_{\boldsymbol{u}_y,r})}\right) \tag{5-1}$$

These angles are displayed in figure 5-8.

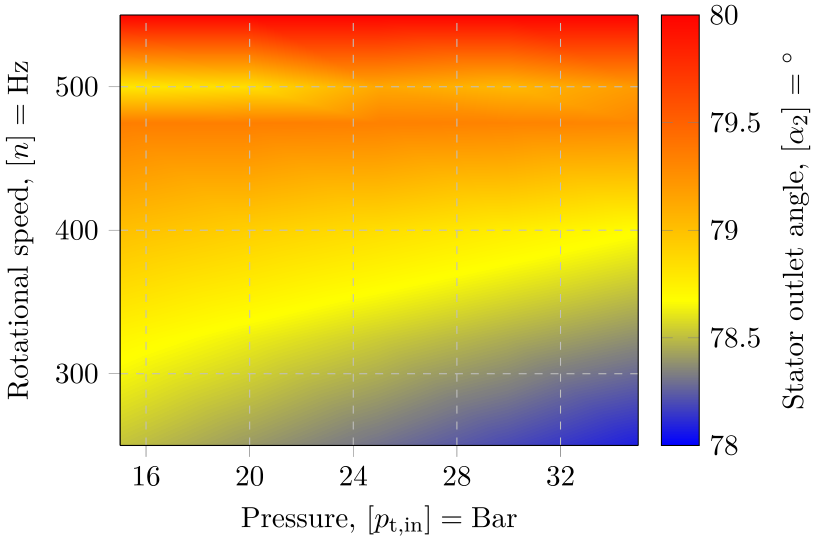

Figure 5-8: Absolute angles of the flow at the mixing plane

Together with the absolute magnitude of the flow shown in figure 5-9, the velocity vectors of the flow can be constructed.

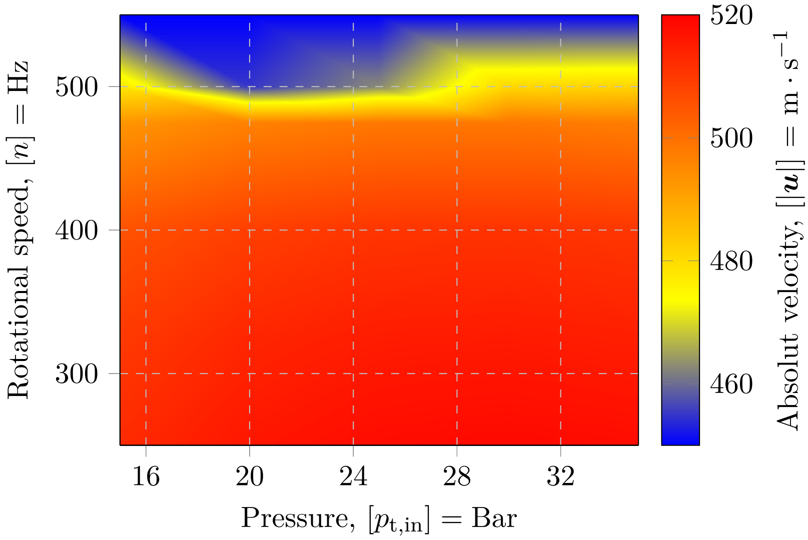

Figure 5-9: Absolute velocity of the flow at the mixing plane

From the geometry in ANSYS CFX , a radius of the turbine rotortip of $r_{\mathrm{rot,tip}} = 0.111\,662\,\mathrm{m}$ is deduced. The rotational speed of the tip can then be computed as such:

$$U_{\mathrm{rot,tip}} = n r_{\mathrm{rot,tip}} \cdot 2 \cdot \pi \tag{5-2}$$

The tangential velocity of the flow relative to the rotor blade velocity can be computed:

$$U_{\mathrm{r,rel}} = |\boldsymbol{u}| \sin \alpha_2 - U_{\mathrm{rot,tip}} \tag{5-3}$$

The vector to this point is called w_2 while the absolute vector is called C_2. The angle between the vertical and the relative velocity vector is called β_2 and is identified as the angle relative to the rotor. The construction of the velocity triangles for different rotational speeds is shown in figures 5-10, 5-11 and 5-12. The rotor inlet angle is available in-house and approaches the relative velocity angle best at $n_{\mathrm{opt}} = 475\,\mathrm{Hz}$.

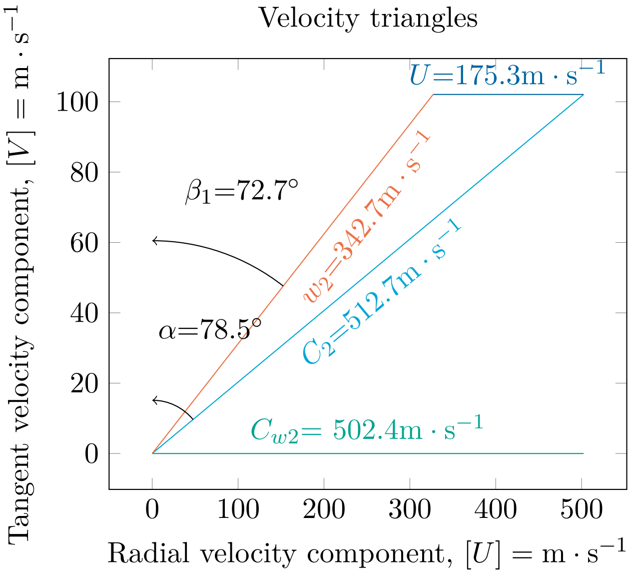

Figure 5-10: Velocity triangle for $p_{\mathrm{t,in}} = 15\,\mathrm{bar}$ and $n = 250\,\mathrm{Hz}$

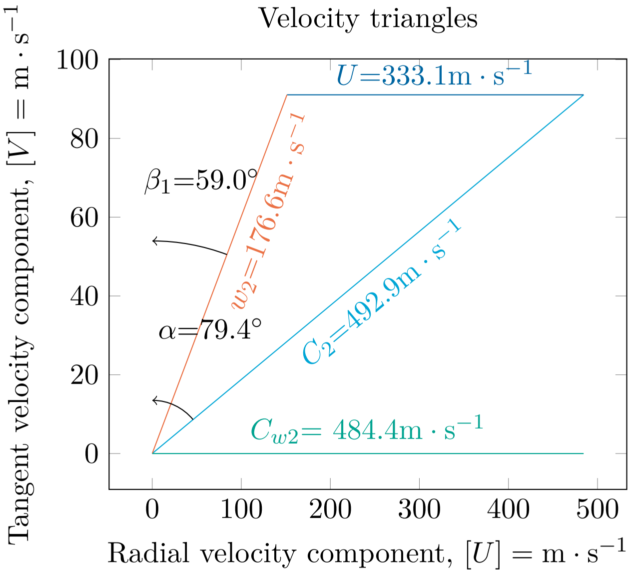

Figure 5-11: Velocity triangle for $p_{\mathrm{t,in}} = 15\,\mathrm{bar}$ and $n = 475\,\mathrm{Hz}$

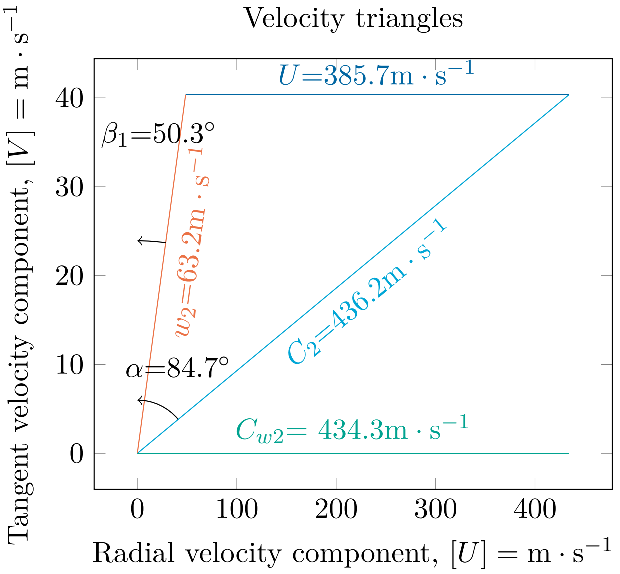

Figure 5-12: Velocity triangle for $p_{\text{t,in}} = 15\,\text{bar}$ and $n = 550\,\text{Hz}$

In figure 5-13, all relative angles are given for different turbine inlet pressures $p_{\text{t,in}}$ and rotational speeds n. As can be seen in this figure, the relative angle shows an optimum for all rotational speeds around $n_{\text{opt}} = 475\,\text{Hz}$.

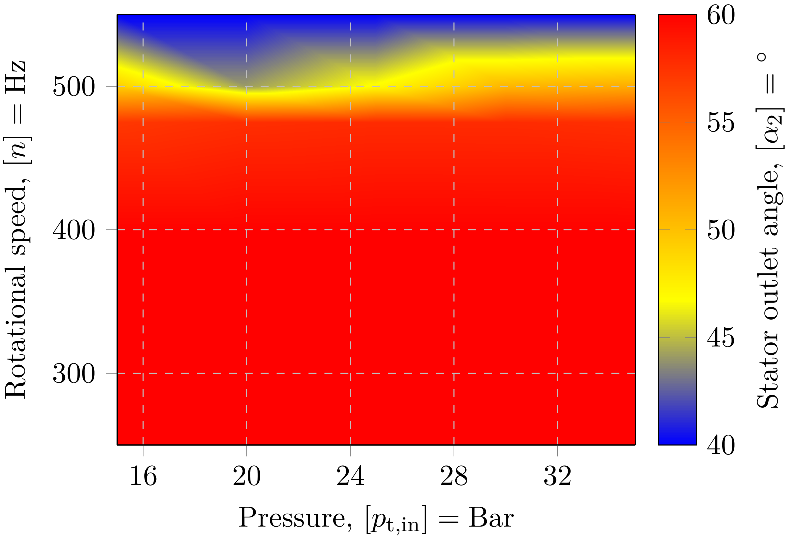

Figure 5-13: Relative flow angles of the working fluid at the mixing plane

When looking at the energy balance over the nozzle (with $[h] = \text{J} \cdot \text{kg}^{-1}$):

$$E_{\text{in}} = E_{\text{out}} \tag{5-4}$$

$$\Delta h_{\text{nozzle}} = \frac{1}{2}\Delta V_{\text{nozzle}}^2 \tag{5-5}$$

And the initial velocity is neglected as this is very small compared to the velocity after the nozzle, the enthalpy difference over the turbine can be approached as such

$$\Delta h_{\text{nozzle}}=\frac{1}{2}V_2^2 \tag{5-6}$$

So the greater the velocity C_2, the greater the enthalpy drop over the stator, hence a higher power output out of the turbine for a certain mass flow.

Next subsection goes in to more depth about the enthalpy difference over the turbine.

5-3-6 Enthalpy difference

In this subsection, simulation data is processed in order to get a quantitative view on work output of the turbine. The work output of the turbine is defined as such

$$W_{\text{t,out}}=\dot{m}(h_{\text{t,in}} - h_{\text{t,out}}) \tag{5-7}$$

In section 2-9, figure 2-6, it is stated that the mass flow is a linear proportional to the turbine inlet pressure (which is in turn linear to the evaporator heat input). This means that the turbine power output, together with the static enthalpy difference, can be computed.

The static enthalpy difference can be seen in figure 5-14. It is apparent that an optimum is visible and that, from the statement made above, this is also the optimum for the power output of the turbine. For a low pressure this optimum is a little less clear than for turbine inlet pressures $p_{\text{t,in}} = 20\,\text{bar}$ to $25\,\text{bar}$.

From previous subsection and from figure 5-14, it is apparent that the optimal rotational speeds is constant for all turbine inlet pressures $p_{\text{turb,in}}$. It is not completely clear why this is the case because operation conditions change over different inlet pressures. It might be the result of a changing mass flow (figure 5-23) and a changing degree of reaction Λ which is shown in figure 5-16.

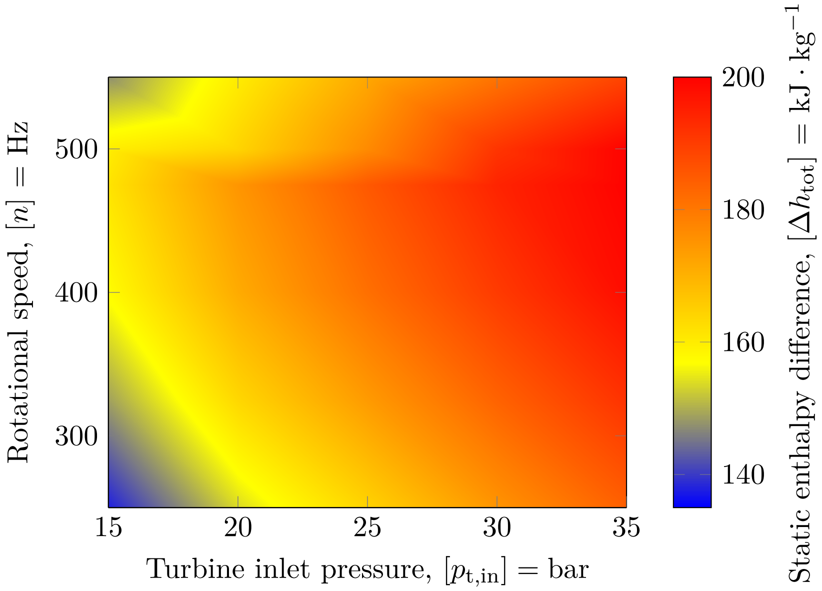

Figure 5-14: Static enthalpy difference for certain turbine inlet pressures and rotational speeds

The definition of static and total enthalpy is already given in section 4-5, equation 4-9.

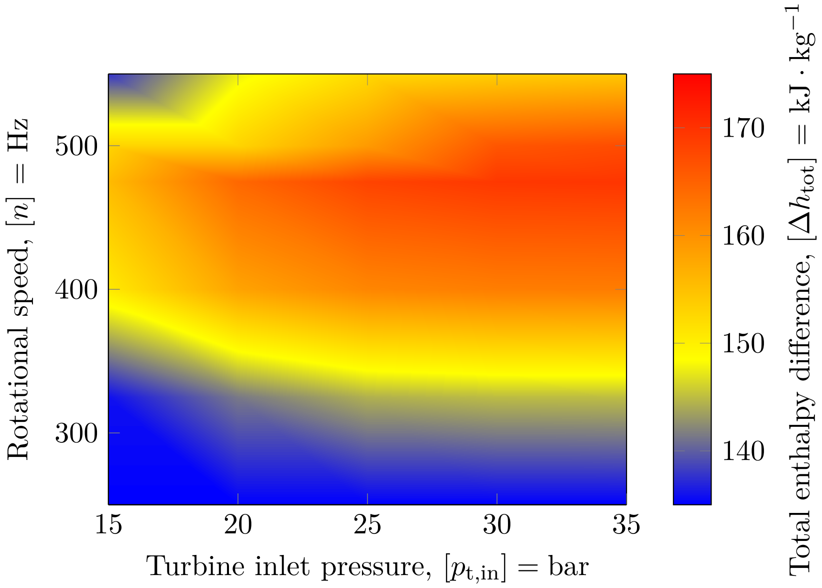

Figure 5-15: Total enthalpy difference

The degree of reaction says something about the fraction of energy extracted by the rotor with respect to the total extracted energy. This is implemented in the following formula:

$$\Lambda = \frac{\Delta h_{\mathrm{stat,rot}}}{\Delta h_{\mathrm{stat,stage}}} \tag{5-8}$$

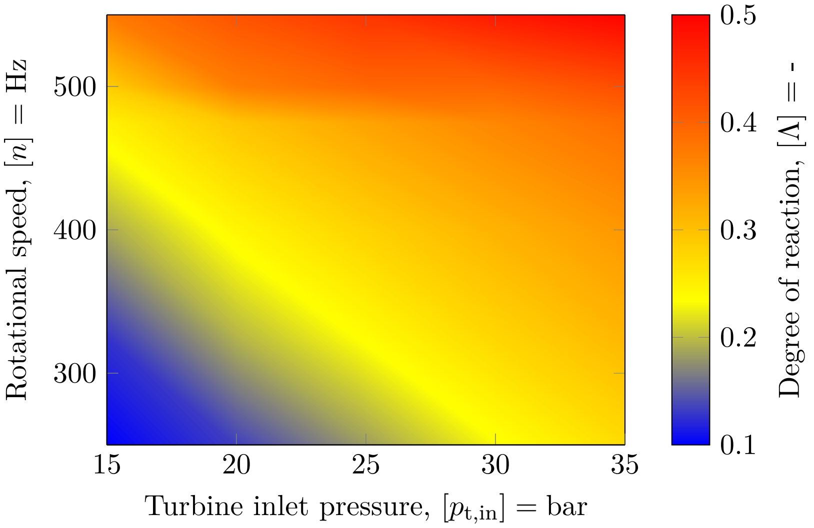

Figure 5-16: Degree of reaction

Now enthalpy differences and the degree of reaction are discussed, a further look into efficiencies can be given. This is shown in the next subsection.

5-3-7 Efficiency

Important performance indicators of a turbine are efficiencies, which are shown in this subsection.

The total to total efficiency of a turbine stage is computed as such:

$$\eta_{\mathrm{tt}}=\frac{h_0-h_2}{h_0-h_2'} \tag{5-9}$$

and the total to static efficiency is defined as

$$\eta_{\mathrm{ts}}=\frac{h_{0,\mathrm{s}}-h_{2,\mathrm{s}}}{h_{0,\mathrm{s}}-h_2'} \tag{5-10}$$

.

The total to total efficiency of the turbine for different turbine inlet pressures $p_{\mathrm{t,in}}$ and rotational speeds n are displayed in figure 5-17. The optimal rotational speed is apparent and lies around $n \approx 475\,\mathrm{Hz}$.

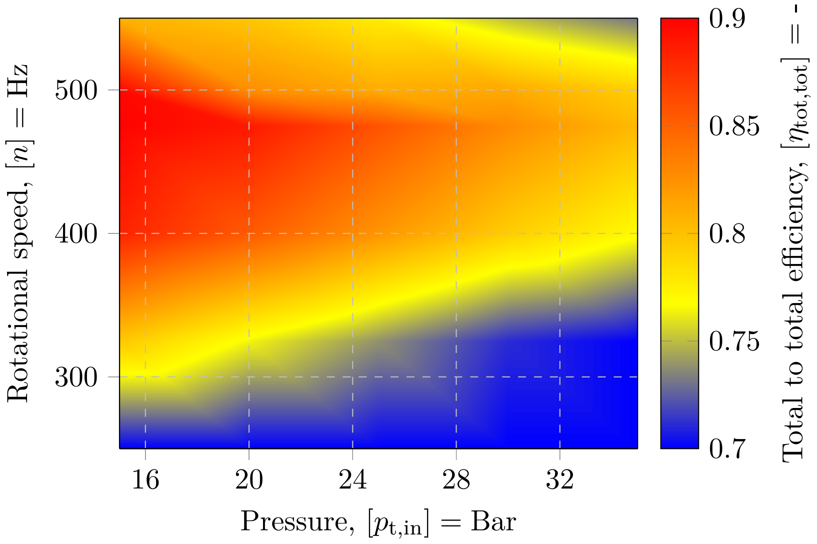

Figure 5-17: Total to total efficiency of the turbine simulated with ANSYS CFX

The total to static efficiency is shown in figure 5-18. There is a broad range of rotational speeds which have the highest total to static efficiencies.

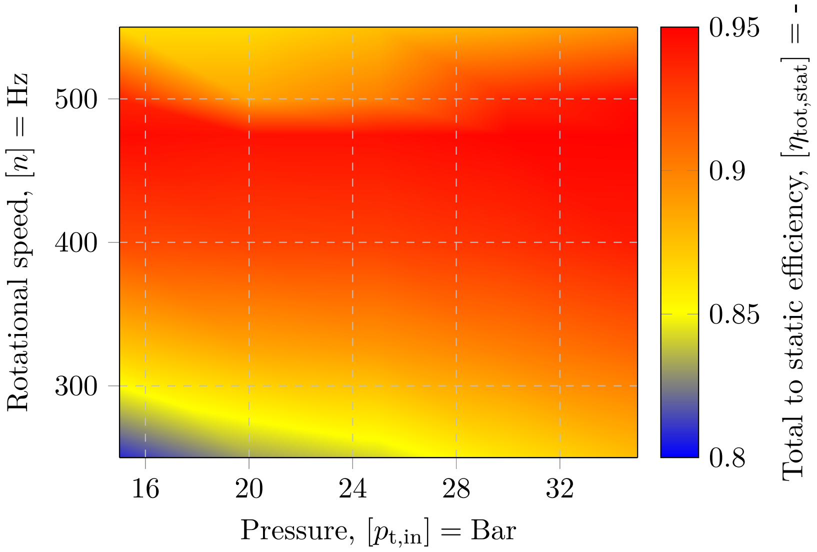

Figure 5-18: Total to static efficiency of the turbine simulated with ANSYS CFX

The total to static efficiency of the stator can also be computed:

$$\eta_{\mathrm{ts}} = \frac{h_{0,\mathrm{s}} - h_{1,\mathrm{s}}}{h_{0,\mathrm{s}} - h'_1} \tag{5-11}$$

The results are given in figure 5-19.

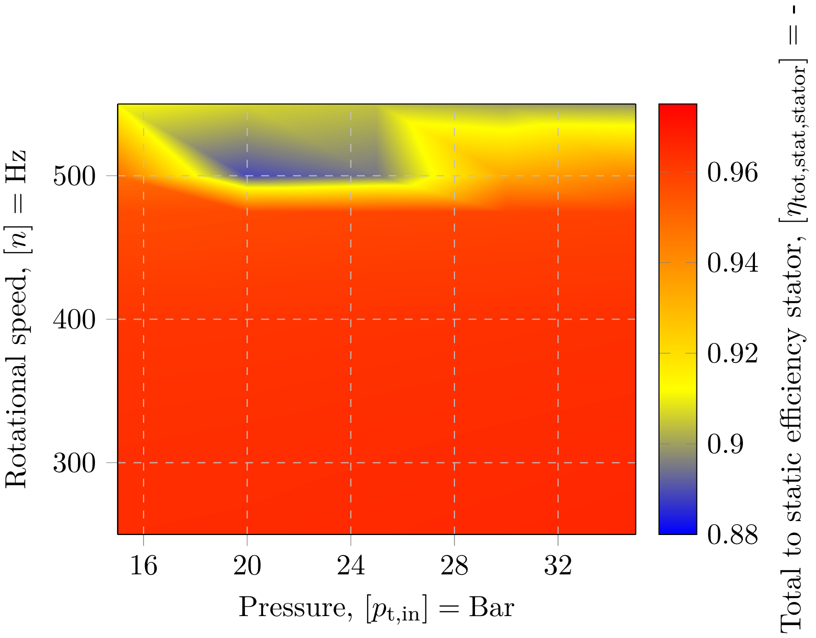

Figure 5-19: Total to static efficiency of the stator

This efficiency drops significantly after the rotational speed passes the $n = 475\,\mathrm{Hz}$. Thus the amount of energy extracted from the working fluid is high for rotational speeds below $n \approx 475\,\mathrm{Hz}$ independent of turbine inlet pressure but drops significantly for higher rotational speeds.

5-3-8 Outflow losses

One of the losses of a turbine is a high speed at the outlet of the turbine. When the turbine has extracted a large amount of energy from the flow, the outlet velocity tends to be low. From the simulations in ANSYS CFX , the Mach number Ma can be deduced for different turbine inlet pressures $p_{\mathrm{t,in}}$ and rotational speeds, given in figure 5-20. The mach number is the ratio of the speed and the speed of sound:

$$Ma = \frac{V}{a} \tag{5-12}$$

In the figure 5-20, the transition to a supersonic flow in the nozzle is greatly visible.

The energy loss can also be computed with the following equation. Assumed is that the outlet velocity of the recuperator is negligible compared with the outlet velocity of the turbine. This is also discussed in section 4-5.

$$E_{\mathrm{loss}} = \frac{V^2}{2} \tag{5-13}$$

With V the outlet velocity of the turbine and with $[E] = \mathrm{J} \cdot \mathrm{kg}^{-1}$

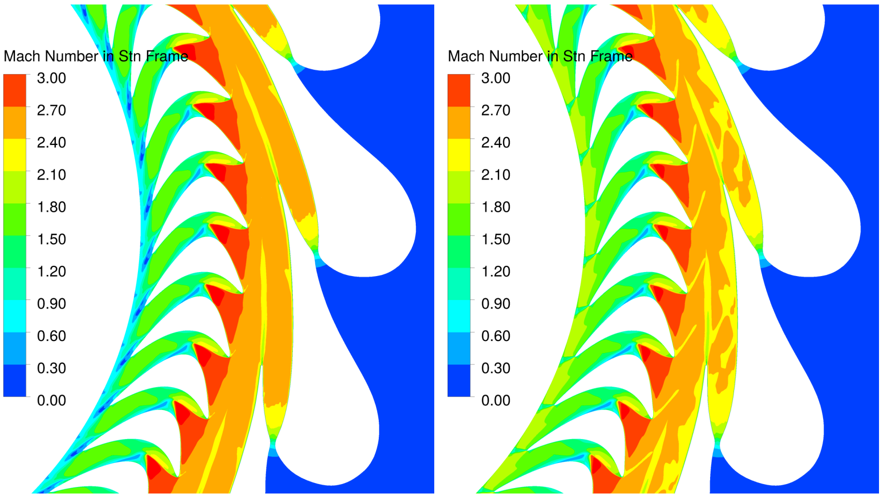

(a) $p_{\mathrm{t,in}} = 15\,\mathrm{bar},\ n = 250\,\mathrm{Hz}$ **(b)** $p_{\mathrm{t,in}} = 35\,\mathrm{bar},\ n = 250\,\mathrm{Hz}$

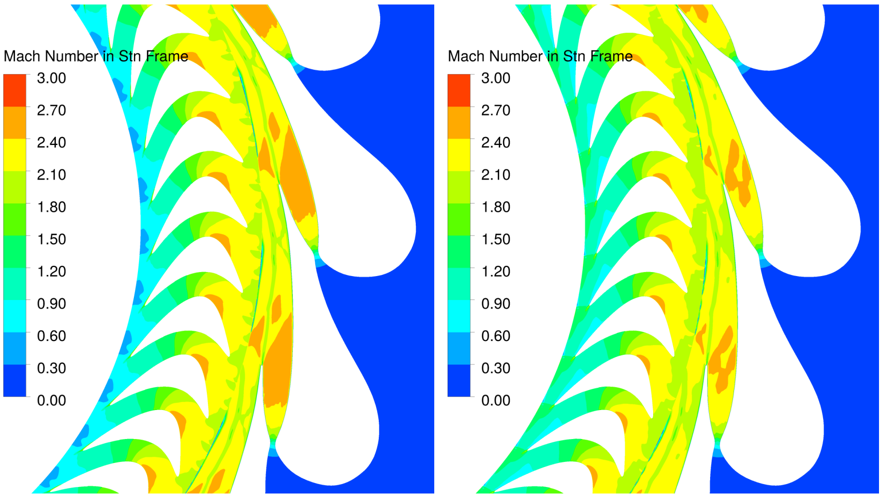

(c) $p_{\mathrm{t,in}} = 15\,\mathrm{bar},\ n = 550\,\mathrm{Hz}$ **(d)** $p_{\mathrm{t,in}} = 35\,\mathrm{bar},\ n = 550\,\mathrm{Hz}$

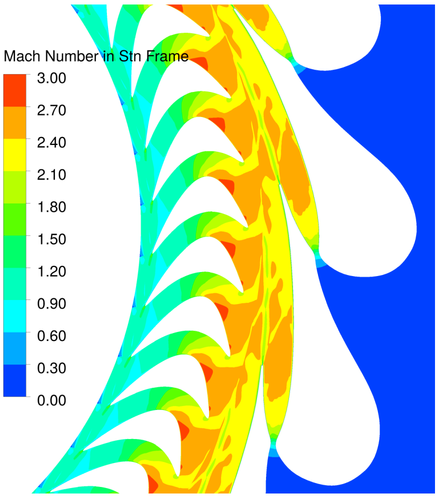

(e) $p_{\mathrm{t,in}} = 25\,\mathrm{bar},\ n = 475\,\mathrm{Hz}$

Figure 5-20: Mach number for different inlet properties

The outcome of this equation is shown in figure 5-21.

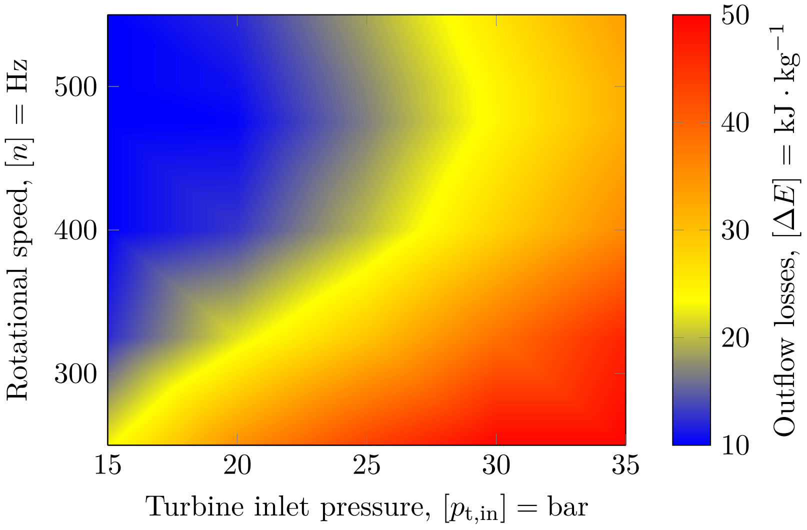

Figure 5-21: Outflow losses

As can be seen in figure 5-21, the losses are at a maximum for high turbine inlet pressures $p_{\mathrm{urb,in}}$ and low rotational speeds n. At an optimal rotational speed of $n_{\mathrm{opt}} = 475\,\mathrm{Hz}$, the outflow losses are at a minimum for all turbine inlet pressures $p_{\mathrm{t,in}}$.

The outlet pressure of the turbine is given in figure 5-22 for different turbine input pressures and rotational speeds. The graph looks similar to figure 5-21.

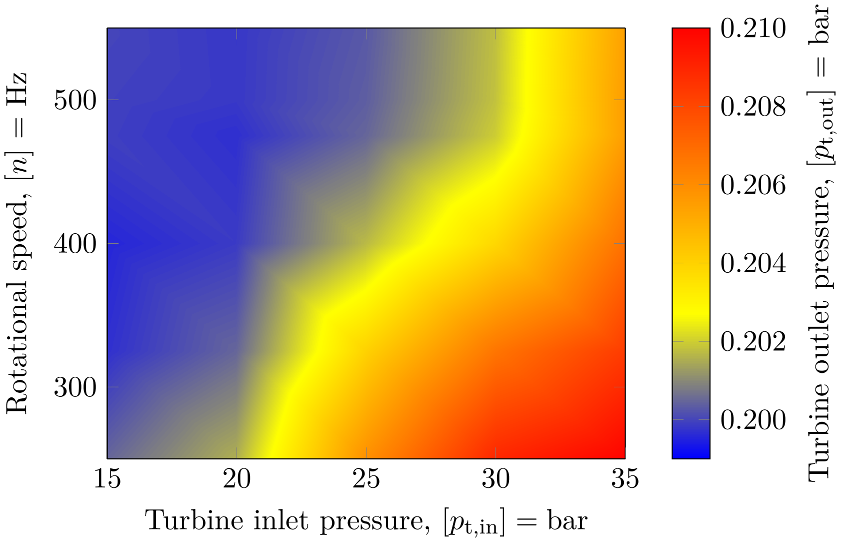

Figure 5-22: Absolute turbine outlet pressure as function of inlet pressure and rotational speed

In this section, the results of the turbine simulations are shown and a qualitative analysis is done. Next section shows the outcome of the cycle model.

5-4 Cycle

In previous sections, the results of the pump model and the turbine map are presented. This input data is pivotal for the outcomes of the cycle model which is discussed in chapter 2. In this section, the first results of the cycle model are shown and some analysis is done.

The mass flow of the working fluid is one of the important outcomes of the model and is both depending on the choked flow relation, the pump characteristic and the turbine map. The mass flow depends on the turbine inlet pressure which in turn depends on the pump characteristic. Because of the changing turbine inlet conditions, the turbine map is also necessary. A certain mass flow belongs to a turbine inlet condition. The system is controlled using the turbine inlet temperature as reference.

The mass flow as function of the evaporator heat input is shown in figure 5-23.

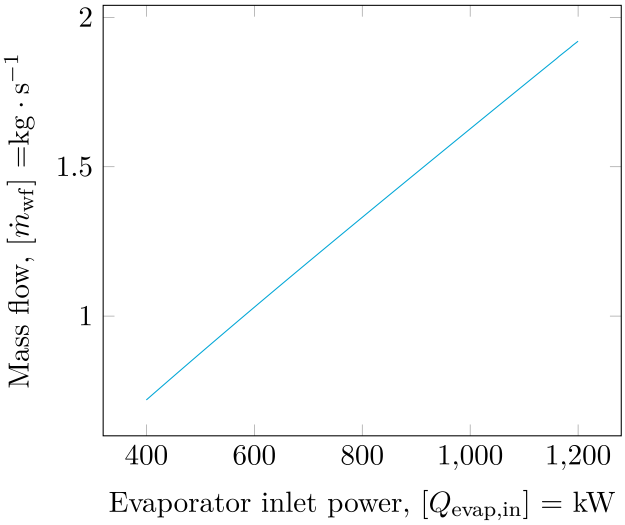

Figure 5-23: Mass flow of the working fluid as function of the evaporator heat input

5-5 Pump adjustments

In the previous section, the outcomes of the cycle model according to design specifications are presented. In section 5-2, the outcomes of the turbine wheel simulations are shown and discussed. From the inlet angle as function of the pressure $p_{\mathrm{t,in}}$ and the rotational speed n shown in figure 5-13 and the total to total efficiency as function of the pressure and the rotational speed shown in figure 5-17, it is apparent that the optimal rotational speed is $n_{\mathrm{opt}} = 475\,\mathrm{Hz}$.

5-5-1 Adjustments to the current system

From the beginning of this research project, some changes to the system are suggested:

- Throttling of the flow after the main pump
- Bypassing the flow around the pump

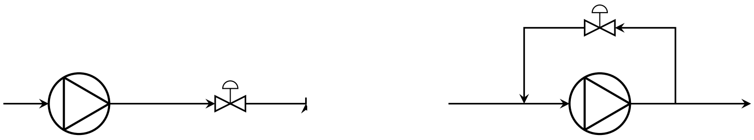

(a) Throttle **(b)** Bypass

Figure 5-24: Pump configurations

- Conical valve into the diffuser

The last option might be a good and valuable option but it is hard to implement such complex adjustment and the behaviour of a new designed valve is something out of the scope of this research.

Throttling can be achieved by adding a valve to the system in order to change the system characteristics. It is good practice that the valve is placed at the outlet of the pump. If it would be placed at the inlet, cavitation will most likely occur due to the low pressure at the pump inlet. Throttling will increase the outlet pressure of the pump. Throttling is suggested for pumps with a low specific speed and where a high pressure is required [21]. A scheme of a pump with a throttle valve is shown in figure 5-24a.

Bypassing a pump is frequently done to cause a minimal flow. This is not required in this case. Bypassing the pump increases the volumetric flow through the pump without changing outlet pressure of the pump. A simplistic scheme of a bypass is shown 5-24b.

Because the Barske pump in the system requires a high static pressure and the specific speed is low, the throttling adjustment is most likely to be chosen. It is also not favourable that the volumetric flow increases because of the steep pump characteristic (figure 3-3). The mass flow is governed by the choked flow inside the turbine stator so another actuator to control the mass flow is not required (and it might even make the system unstable).

The throttle valve can be placed in different places in the original design. It can either be implemented between the main pump and the recuperator or the recuperator and the evaporator. The valve must be placed before the turbine in order to reach the correct turbine inlet pressure $p_{\mathrm{t,in}}$. To prevent the evaporator from malfunctioning, the valve cannot be placed after the evaporator. Because the fluid before and after the throttle valve is in ideal situation isenthalpic and the pressure decreases, the temperature has to increase. This can be used in order to increase the efficiency of the new situation. The valve can also extract heat from the system because is it larger than the piping and the conductive heat transfer to the surroundings will be higher. So in order to use the heat input by the valve and to diminish the heat transfer after the heated up working fluid after the recuperator, the valve is placed just right behind the main pump. The new system configuration can be found in figure 5-25.

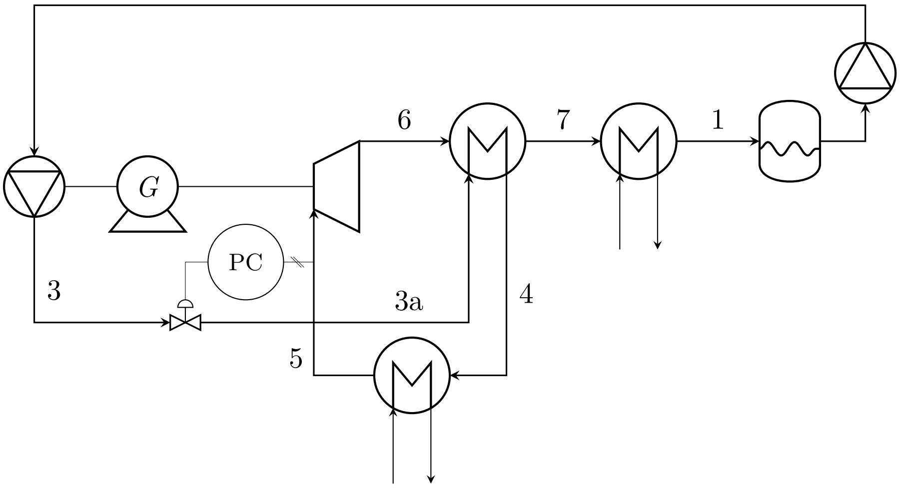

Figure 5-25: Triogen system with implementation of the throttle valve and additional control system

5-5-2 Model comparison

Now that a optimal rotational speed is found $n_{\text{opt}} = 475\,\text{Hz}$ together with an approach on how to reach this optimal rotational speed with the system, a comparison of the results of both the original design and the system with the throttle valve implemented is necessary. A copy of the cycle model for the original design is duplicated into the same MICROSOFT EXCEL file and a throttle valve is added to this cycle. The rotational speed of the turbine and the pump is set at a constant rotational speed. The control mechanism introduced in section 2-10 can no longer be used. The turbine inlet temperature is controlled by means of the outlet pressure of the throttle valve. This means physically that the valve is closed when the pressure is too high and vice versa.

The most interesting result is the power output of the system with the throttle valve compared with the power output of the original design situation. The mechanical power output of the system as function of the thermal power input is shown in figure 5-26.

$$W_{\text{t,out}} = \dot{m}_{\text{wf}}(h_{\text{t,in}} - h_{\text{t,out}}) \tag{5-14}$$

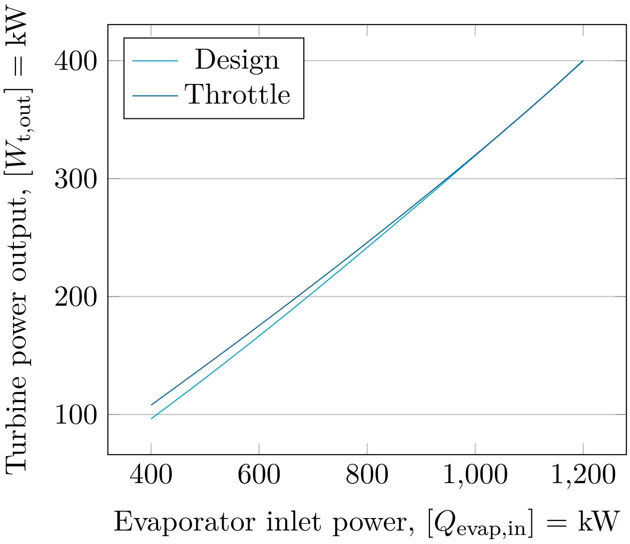

Figure 5-26: Mechanical turbine power output for both original design situation and new throttle implementation

The implementation of the throttle valve will come at a cost because the working fluid is pumped. The mechanical power which is consumed by the pump is displayed in figure 5-27. The steps which are apparent at $Q_{\mathrm{evap,in}} \approx 500\,\mathrm{kW}$ and $Q_{\mathrm{evap,in}} \approx 1150\,\mathrm{kW}$ might be numerical induced. This has no further physical meaning.

$$W_{\mathrm{pump,in}} = \dot{m}_{\mathrm{wf}}(h_{\mathrm{pump,out}} - h_{\mathrm{pump,in}}) \tag{5-15}$$

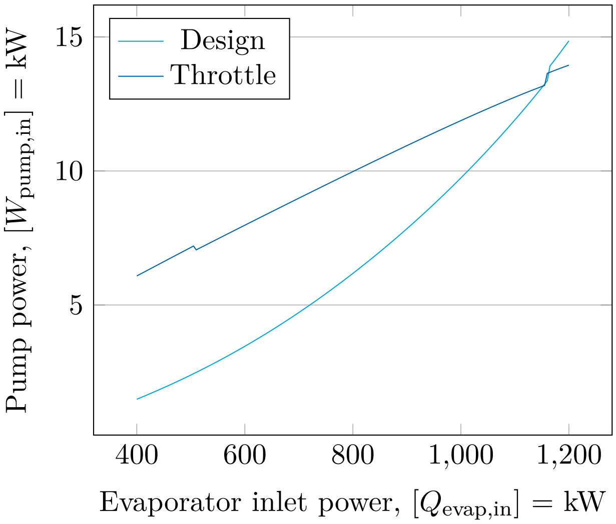

Figure 5-27: Mechanical pumping power necessary

Finally, the question rises what the gained power output is after the system is modified. The net power output of the shaft is computed in equation 5-16. One important note, the pre-feed pump in the original design is driven electrically. In reality, the power consumed of the pre-feed pump is different than computed in this research. The efficiency is taken the same as that of the main pump (as discussed in section 2-2) and the electrical efficiency of the pump is also not taken into account.

$$W_{\text{net,out}} \approx W_{\text{t,out}} - W_{\text{mp,in}} - W_{\text{pf,in}} \tag{5-16}$$

This net power output tells us something about the power which is extra gained when the system would be adjusted with the throttle valve. The graph which compares the design conditions with the throttle conditions is shown in figure 5-28. As can be seen in the figure, the maximum power output gained by modify the system is $\approx 7\,\%$ of the old net power output. According to the power output displayed in figure 5-26, the maximum power gained is $\Delta W_{\text{gain}} \approx 7\,\text{kW}$.

At $Q_{\text{evap,in}} \approx 800\,\text{kW}$, there is no power extra gained by the throttle model compared with the original design. This is not due to the fact that the model has reached $n_{\text{opt}} = 475\,\text{Hz}$ but because the extra pumping power is higher than the net gained turbine power. At $Q_{\text{evap,in}} \approx 1150\,\text{kW}$, the model of the original design reaches the rotational speed $n_{\text{opt}} = 475\,\text{Hz}$. This is also shown in figure 5-34.

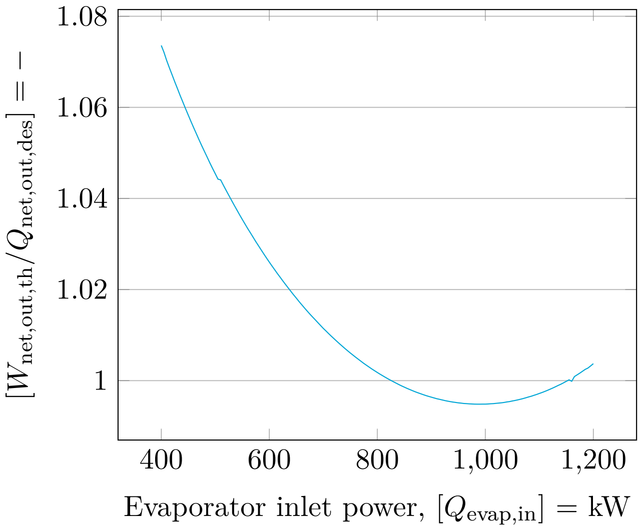

Figure 5-28: Mechanical pumping power necessary

An interesting question is whether the extra pump power which is required to maintain the rotational speed of $n_{\text{opt}} = 475\,\text{Hz}$ is a result of the extra friction of the disc or the extra velocity of the working fluid. The formulas used in 3-3, equations 3-7 and 3-8 are applied both to the new throttle design and the original and the difference is shown in 5-29.

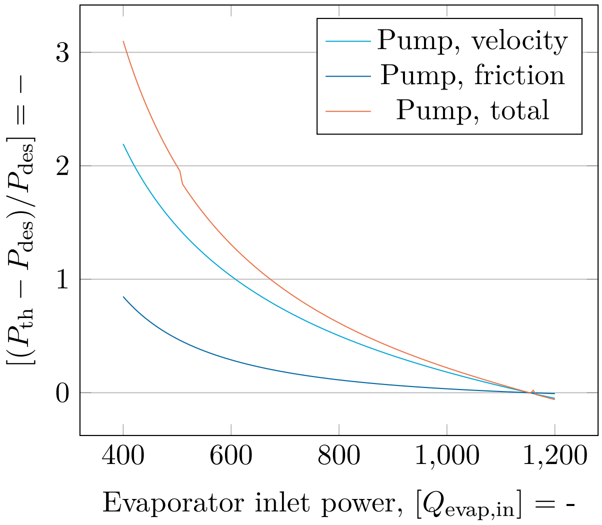

Figure 5-29: Extra pump power relative to design

An important measure for a power cycle is the thermal efficiency. The thermal efficiency is defined as such:

$$\eta_{\text{th}} = \frac{W_{\text{net,out}}}{Q_{\text{in}}} \tag{5-17}$$

The thermal efficiency of both the original design and the system with the throttle valve is shown in figure 5-30. In the graph can be seen that the thermal efficiency increased with $\Delta\eta_{\text{th}} = 2\,\%$. This might seem not quite a lot but relative to the maximum thermal efficiency, this is not negligible amount.

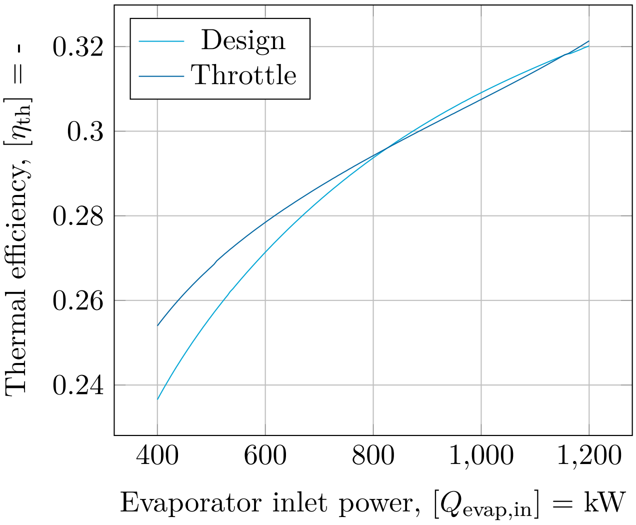

Figure 5-30: Thermal efficiency

In figure 5-31 are the isentropic (or total to static) efficiencies of both turbine and pump for design operations and throttle valve addition shown. It is apparent that the turbine efficiency is increased significant for low evaporator heat input.

The pump efficiency is mainly governed by the rotational speed, the mass flow and the pressure difference. The pump efficiency has shifted to the right. For a small evaporator heat input for the design conditions, the pump has a low rotational speed and a similarly low pressure difference. For this reason, the efficiency is high for low heat inputs.

On the other hand, the efficiency maximum for the throttle valve situation is at an evaporator heat input of $Q_{\mathrm{evap,in}} \approx 900\,\mathrm{kW}$. For this situation, the pump output power is high compared to the pump input. The pressure difference is high and the mass flow is increased with respect to low evaporator heat input.

The pump is designed to have it's highest efficiency at the design operation point $Q_{\mathrm{evap,in}} \approx 1000\,\mathrm{kW}$. It is interesting that from the cycle model, another maximum is found.

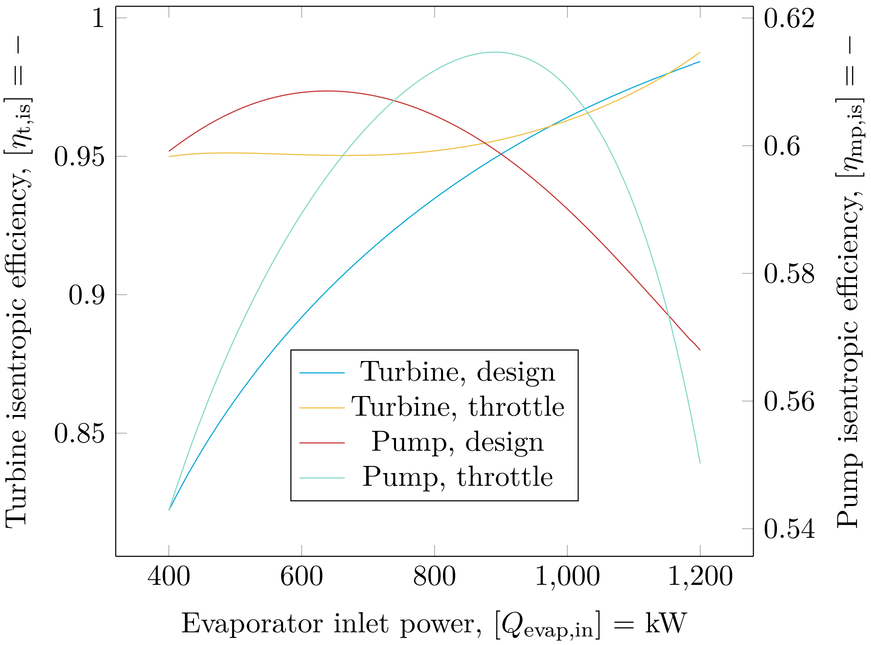

Figure 5-31: Isentropic efficiency

Due to the increase in turbine efficiency, the temperature of the working fluid at the turbine outlet $T_{\mathrm{t,out}}$ is lower. This has to be taken into account because the recuperator duty decreases because of the lower temperature difference between the hot and cold side. This change in recuperator heat transfer is shown in 5-32.

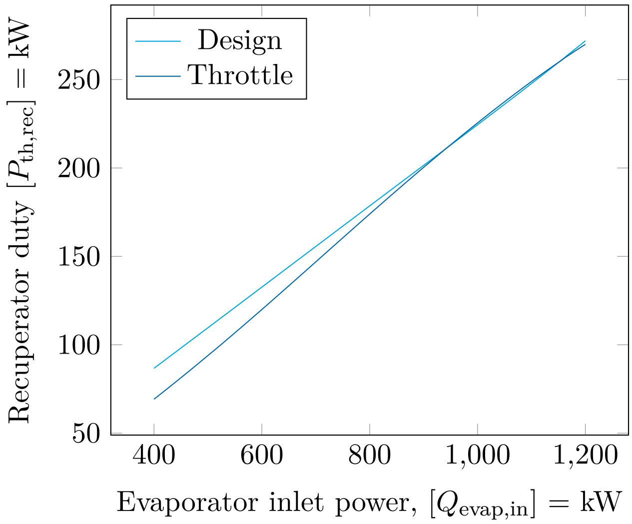

Figure 5-32: Thermal power transferred by the recuperator with different evaporator inlet power

From the graph 5-29 it is clear that at the lowest power input, the application of a throttle valve is most beneficial. It is now interesting to use the comparing cycle model for different high-speed turbo generator (HTG) rotational speed. From figures 5-13 and 5-17 we assumed the optimal rotational speed to be $n_{\text{opt}} \approx 475\,\text{Hz}$ but if it is also the optimal rotational speed of the system is not apparent figured out till this point. The cycle model is modified in order to test for the lowest heat input $Q_{\text{evap,in}} = 400\,\text{kW}$ and a range of rotational speeds for the throttle case of 425 Hz to 500 Hz. The difference in net power output is computed as the ratio $W_{\text{out,net,th}}/W_{\text{out,net,des}}$ and is shown in figure 5-33.

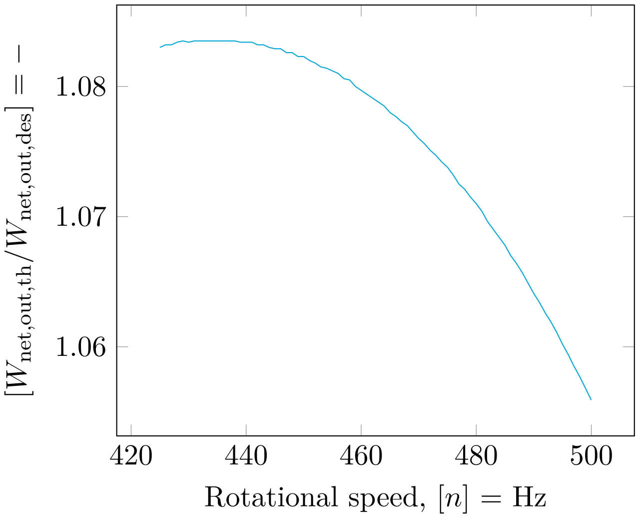

Figure 5-33: Net power ratio for different rotational speeds at a evaporator heat input of $Q_{\text{evap,in}} = 400\,\text{kW}$

As can be seen in the figure is the net power difference greatest at $n \approx 445\,\text{Hz}$. This is due to the decrease in power consumption with respect to the $n_{\text{opt}} \approx 475\,\text{Hz}$. Of course it is a small deviation of the net power output gained but it might be an opportunity to redesign the pump for this

Now the approach to a new system modification is explained in this section, the next section will go into further depth about the control of this new throttle valve.

5-6 Valve control

In the previous section, a novel system adjustment is suggested and some performance indicators are shown. In this section the control of the throttle valve in the system is highlighted.

The control mechanism of the adjusted system is different than that of the original design. The current system controls the cycle by means of a variable speed drive (VSD). In the cycle model of the system, the rotational speed is the actuated value.

In the new situation, the rotational speed of the shaft is kept constant at $n_{\text{opt}} = 475\,\text{Hz}$. The new variable which can be changed in order to achieve the correct turbine inlet pressure $p_{\text{t,in}}$ is the recuperator inlet pressure. The throttle valve can be operated during evaporator heat input changes to keep the system stable. The implementation of the sensor and the actuator is shown in figure 5-25. The pressure controller (PC) takes information from a pressure sensor and processes the data to induce a valve action.

The dynamics of the pump and the turbine are relative fast, that of the heat exchanger slow. A proportional and Integrating (PI) controller might be sufficient to keep the system stable and control fast enough [10].

The pressure ratio over the valve as function of the evaporator heat input is shown in 5-34. When the pressure ratio $\frac{p_{\text{mp,out}}}{p_{\text{rec,in}}} < 1$, the pressure after the throttle valve is higher than the pressure after the main pump. This means physically that the pressure is increasing through the valve, as though the valve mimics a pump. This is not possible, the cycle model of the throttle adjustment demands the pressure after the valve to be higher in order to keep te system stable. This means that after the point of $\frac{p_{\text{mp,out}}}{p_{\text{rec,in}}} < 1$ the rotational speed of the throttle model is lower than that of the original design.

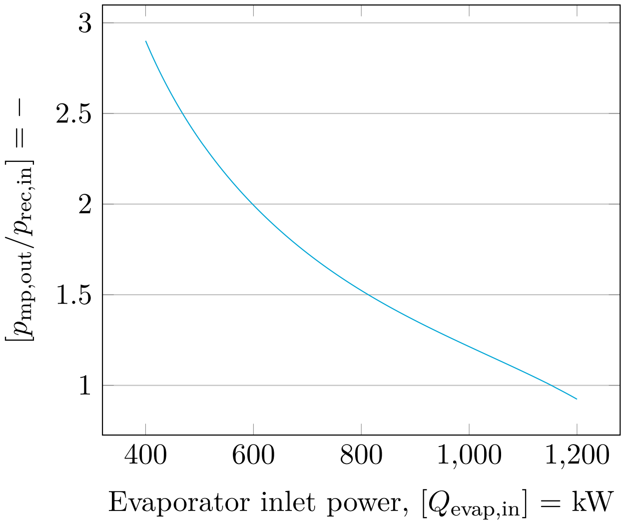

Figure 5-34: Pressure ratio over throttle valve

From the cycle model, the pressure ratio over the main pump is extracted. This pressure ratio during throttling is shown in figure 5-35.

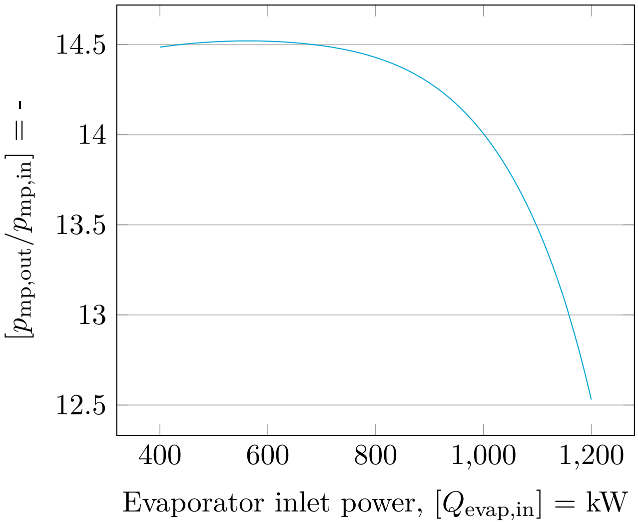

Figure 5-35: Pressure ratio over pump during throttling

This chapter covered all results of the research project. Now that all results are made clear, a conclusion is drawn in the following chapter.

Chapter 6

Conclusion

6-1 Discussion

In order to increase the accuracy of the model, more effort can be put into the modelling of the heat exchangers. The heat exchangers were only modelled as they were "designed" every simulation of the cycle again and again but this is of course not the case. Dimensions and characteristics of the heat exchangers have to be considered. Some experimental results of heat exchangers in the field can be used to model the heat exchangers more accurately.

For simplicity sake, the pre-feed pump is modelled in the cycle model as it has the same isentropic efficiency as the main pump. In reality, this is not the fact because the pump is not driven by the high-speed turbo generator (HTG) and it is a completely different pump type. To increase the completeness of the cycle model and give a more realistic view on the situation, the isentropic efficiency (probably as function of the mass flow) can be taken into account.

During the initialisation of this research, the question raised to to compare the results of the cycle model with experimental data of costumers of Triogen. During the time of this research, it was clear that this assignment was not possible in the planning of this research project. In the future, effort can be put into comparing the outcomes of this project with experimental data.

As described in section 2-2-3, the inlet pressure of the recuperator computed in the cycle model is not an input for the turbine simulations. This means that the outlet pressure of the turbine in the simulations is kept at $p_{\text{turb,out}} = 0.2\,\text{bar}$. The calculations of the diffuser depends on the entropy at the outlet of the turbine $s_{\text{turb,out}}$ and the recuperator inlet pressure $p_{\text{rec,in}}$ but this computation fails if the recuperator inlet pressure is much higher $p_{\text{rec,in}} > p_{\text{turb,out}} = 0.2\,\text{bar}$. So new research can be done in order to connect the cycle model to the outlet pressure of the turbine.

Whether the modification of adding a throttle valve is economically attractive depends heavily on the nature of the heat source which is provided by the client. If the system is a large part of the operation time operated in part load, this option might be a good one. For clients who operate largely on design conditions, the extra costs of adding a throttle might be higher than the benefits.

Because it is not in the scope of this research, technical implementation of the throttle valve is not fully worked out in this research project. The full implementation of a throttle valve means engineering of control, dimension of valve, edit technical drawings and make force balances of the new system. These extra tasks have to be completed in order to fully implement the throttle valve.

As discussed in section 5-5, the isentropic efficiency of the main pump is highly dependent on the evaporator heat input and during part load operation of the throttle system, the pump efficiency decreases rapidly with decrease of heat input. As described in section 5-5, for low heat input $Q_{\text{evap,in}}$, the optimal rotational speed of the system is not equal to that of the turbine because of the required pump power. Therefore it might be interesting to investigate a pump optimisation in order to also reach a higher isentropic efficiency during part load with the throttle modification. Also the pump its optimal efficiency point is found not on the design operation point, discussed in section 5-5. The pump might be redesigned in order to shift this optimum.

In subsection 5-3-6 is discussed that the optimal rotational speed is not a function of the turbine inlet pressure $p_{\text{t,in}}$. A cause of this may be found in the change in mass flow and the change in degree of reaction Λ for different turbine inlet pressures. The proof of this statement is not found in this research project and further research might be necessary to confirm this theory.

6-2 Conclusion

As discussed in section 1-1, changing climate and the increasing CO_2 emissions demands for changes in industry. An organic Rankine cycle (ORC) can be a good solution in order to increase the efficiency of already existing power plants. The system of Triogen is able to ”boost” an industrial engine in the range of 1 MW to 2 MW with about 10 %. In section 1-1 a framework is given of the current hot research topics in the ORC field. Because of the single shaft and the single stage radial inflow cantilever turbine, the Triogen system is quite a unique one in the ORC market. Already a variety of research is done by Triogen in order to increase the effiency but a gap in research is the optimisation of the pump for part load operation. Thus the research topic of this thesis is: Optimisation of pump operation to increase the cycle efficiency of an ORC during part load.

In chapter 2, the outline of a cycle model is given which is used to have a general interpretation of the system and to use this model as computation method to find the results for this research project. One of the important findings is the choked flow condition and a way to cope with it in the cycle model. Because the model is made in MICROSOFT EXCEL , the fluid properties are tabulated to decrease computation time. Chapter 3 and 4 go into further depth about the input for the cycle model respectively the input for the pump and the input for the turbine characteristics.

Chapter 3 discusses the performance analysis of the Barske pump, which is not a very commonly used pump on which not a lot research is done. The relations used are from the original paper which presented the pump. In 3-2, the relation between the volumetric flow and the pressure difference of the pump is shown. These analytical formulas and the relation from literature is used in the model as input for the pressure difference computations. The efficiency, computed in section 5-3-7 is also necessary as input for the model.

The initialisation of the simulations of the turbine wheel is discussed in section 4-2. The boundary conditions of the geometry are written down together with all important properties which are used. The way which led to a great converged simulation is described in sections 4-2-9 and 4-3. One of the important findings is that the simulations for $n = 550\,\text{Hz}$ were not converging, therefore an extra rotational speed is added of $n = 500\,\text{Hz}$. The chapter ends with the implementation of the turbine map into the model.

This report concludes with a presentation of the results in chapter 5. In section 5-2, graphs of the flow according to the turbine wheel simulations are shown. The optimal turbine wheel rotational speed is found in section 5-3-5 and 5-3-6 to be $n_{\text{opt}} \approx 475\,\text{Hz}$. The most cost-efficient and effective solution is found to be the implementation of a throttle valve. In section 5-5, the cycle model presented in chapter 2 is compared with a new cycle model with $n_{\text{opt}} = 475\,\text{Hz}$ as constant rotational speed. The comparison shows that, although the pump power increased due to the increase of the rotational speed for low evaporator heat input $P_{\text{th,evap,in}}$, there is a maximum power output increase of $\approx 8\,\%$ possible for $P_{\text{th,evap,in}} = 400\,\text{kW}$.

The modification to the original design exist of the addition of a throttle valve and a new control strategy in order to keep the rotational speed constant and to stabilise the system. This addition might be economically feasible for costumers which have a heat supply which are fluctuating for long time periods. The costs of a throttle valve are relative low and the control of such equipment is widely applied.

Appendix A

Choked flow

The speed of sound is defined as [36]:

$$a=\sqrt{\left(\frac{\partial p}{\partial \rho}\right)_s} \tag{A-1}$$

Which can be easily computed for an ideal gas,

$$a=\sqrt{\gamma \bar{R} T} \tag{A-2}$$

Appendix B

Logarithmic dependence

In this example we use the entropy to show that the entropy depends logarithmically on the pressure. Most of the derivation is written down by Moran and Shapiro [36] and Hołyst and Poniewierski [24].

The definition of entropy:

$$\mathrm{d}S = \frac{1}{T}\,\text{đ}Q \tag{B-1}$$

$$\text{đ}Q = T\,\mathrm{d}S \tag{B-2}$$

This can be put into the definition of the internal energy

$$\mathrm{d}u = \text{đ}q - p\,\mathrm{d}v \tag{B-3}$$

So the following equation is found

$$\mathrm{d}u = T\,\mathrm{d}s - p\,\mathrm{d}v \tag{B-4}$$

Using $h = u + pv$

$$T\,\mathrm{d}s = \mathrm{d}h - v\,\mathrm{d}p \tag{B-5}$$

for an ideal gas, $\mathrm{d}h = c_p(T)\,\mathrm{d}T$ and $pv = \bar{R}T$

$$\mathrm{d}s = c_p(T)\frac{\mathrm{d}T}{T} - \bar{R}\frac{\mathrm{d}p}{p} \tag{B-6}$$

Integrating,

$$s(T,p)=\int_0^T \frac{c_p(T)}{T}\,\mathrm{d}T - \bar{R}\ln\frac{p}{p_{\text{ref}}} \tag{B-7}$$

This equation shows the logarithmic dependence of the entropy on the pressure. Although this is the relation for an ideal gas and it is not the case which is used in this report, it gives a qualitative relation. The entropy as function of the pressure and temperature according to REFPROP [31], is given in figure B-1. As can be seen in this figure, the dependence on the pressure is high for low pressures. Thus there is chosen for a logarithmic scale in order to handle low pressures.

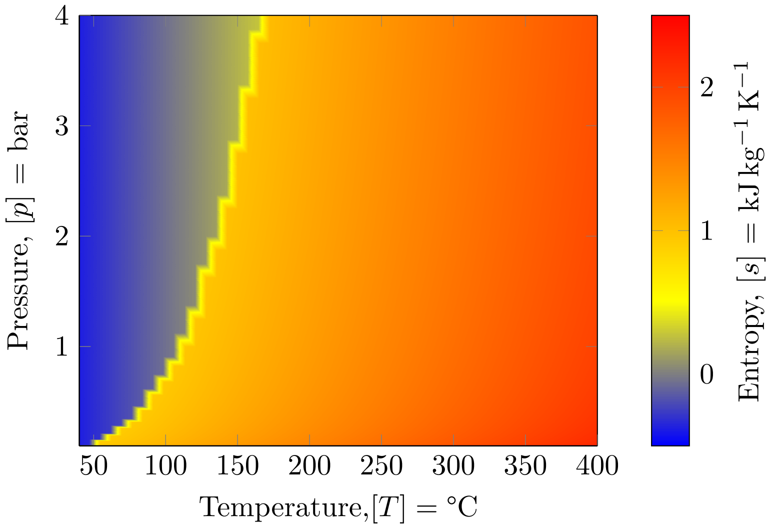

Figure B-1: Entropy as function of pressure and temperature, from Lemmon and Span [31]

Appendix C

Pressure difference

The flow characteristic inside the disc can be described as a solid body rotation [7]. The pressure difference for a solid body rotation can be computed with the simplified form of the Navier Stokes (NS) equations.

To determine if the viscous terms could be safely ignored, the Reynolds number can be utilised:

$$Re = \frac{\text{Momentum forces}}{\text{Viscous forces}} = \frac{DU\rho}{\mu} \tag{C-1}$$

For D we used D_1 from table 3-1. The speed U can be computed as $D_1 n\pi$ and we use the density $\rho \approx 832\,\mathrm{kg \cdot m^{-3}}$. The dynamic viscosity of toluene at the inlet conditions of the pump is $\mu \approx 0.000\,39\,\mathrm{Pa \cdot s}$ [31].

$$Re = \frac{0.015\,\mathrm{m}^2 \cdot \pi \cdot 230\,\mathrm{Hz} \cdot 832.23\,\mathrm{kg \cdot m^{-3}}}{0.000\,39\,\mathrm{Pa \cdot s}} \tag{C-2}$$

$$= 277031 \tag{C-3}$$

This number is assumed high enough in order to neglect viscous forces.

The solution of a solid body rotation is written down by Kundu [28].

The Cauchy equation

$$\rho \frac{\mathrm{D}U_j}{\mathrm{D}t} = \rho g_j + \frac{\partial}{\partial x_i}(\tau_{ij}) \tag{C-4}$$

can be simplified to the Euler equation

$$\rho \frac{\mathrm{D}\mathbf{u}}{\mathrm{D}t} = -\nabla p + \rho \mathbf{g} \tag{C-5}$$

Cancel all zero terms and reduces the equation to

$$-\rho U_\theta^2/r{=}-\frac{\partial p}{\partial r} \tag{C-6}$$

$$0{=}-\frac{\partial p}{\partial z}-\rho g \tag{C-7}$$

With $U_\theta = \frac{\omega r}{2}$

$$p(r,z)-p_0{=}\frac{1}{8}\rho\omega^2(r_2^2-r_1^2)-\rho g z \tag{C-8}$$

With $U_x = \frac{\omega r_x}{2}\Big|_{x=1,2}$ and we ignore any height differences:

$$\Delta p{=}\rho\frac{U_2^2-U_1^2}{2} \tag{C-9}$$

When including the dynamic pressure which is existing at the outlet of the disc:$p_{\text{dyn}} = \rho\frac{U_2^2}{2}$

$$p_{\text{tot}}{=}\rho\left(\frac{U_2^2-U_1^2}{2}+\frac{U_2^2}{2}\right) \tag{C-10}$$

U_1 is the speed of the flow at the inlet of the blade $U_1 = D_1\pi n$, U_2 the speed of the flow at the outlet of the blade $U_2 = D_2\pi n$ and ρ the density of the working fluid.

Bibliography

[1] F. Albergucci, S. Watts, J. Pouponnot, A. Darmedru, and R. Daccord. Pump development for an exhaust heat recovery box on heavy duty trucks. In *5th International Seminar on ORC Power Systems*, volume 5 of *5th International Seminar on ORC Power Systems*, Kluyverweg 1, 2629 HS Delft, The Netherlands, 2019. KCORC: Stichting (Foundation) Knowledge Center on Organic Rankine Cycle Technology.

[2] Louis Albright, Largus Angenent, and Francis Vanek. *Energy Systems Engineering: Evaluation and Implementation, Second Edition.* McGraw-Hill Professional, US, 2012. ISBN 9780071787796. doi: 10.1036/9780071787796. URL `https://mhebooklibrary.com/doi/book/10.1036/9780071787796`.

[3] Dario Alfani, Marco Astolfi, Marco Binotti, Ennio Macchi, and Paolo Silva. Optimization of the part-load operation strategy of sco2 power plants. In *5th International Seminar on ORC Power Systems*, 09 2019.

[4] Nitish Anand, Salvatore Vitale, Matteo Pini, Gustavo J. Otero, and Rene Pecnik. Design Methodology for Supersonic Radial Vanes Operating in Nonideal Flow Conditions. *Journal of Engineering for Gas Turbines and Power*, 141(2), 11 2018. ISSN 0742-4795. doi: 10.1115/1.4040182. URL `https://doi.org/10.1115/1.4040182`. 022601.

[5] Junjiang Bao and Li Zhao. A review of working fluid and expander selections for organic Rankine cycle. *Renewable and Sustainable Energy Reviews*, 24(C):325–342, 2013. doi: 10.1016/j.rser.2013.03.04. URL `https://ideas.repec.org/a/eee/rensus/v24y2013icp325-342.html`.

[6] Dr. Ing. U. M. Barske. Formulae and diagrams for the calculation of open impeller centrigual pumps. Technical report, Rocket propulsion department, Royal aircraft establishment, Farnborough, 1955.

[7] Dr. Ing. U. M. Barske. Development of some unconventional centrifugal pumps. *Proceedings of the Institution of Mechanical Engineers*, 174(1):437–461, 1960. doi: 10.1243/PIME_PROC_1960_174_037_02. URL `https://doi.org/10.1243/PIME_PROC_1960_174_037_02`.

[8] Ian H. Bell, Jorrit Wronski, Sylvain Quoilin, and Vincent Lemort. Pure and pseudo-pure fluid thermophysical property evaluation and the open-source thermophysical property library coolprop. *Industrial & Engineering Chemistry Research*, 53(6):2498–2508, 2014. doi: 10.1021/ie4033999. URL `http://pubs.acs.org/doi/abs/10.1021/ie4033999`.

[9] Aleksandra Borsukiewicz-Gozdur. Pumping work in the organic rankine cycle. *Applied Thermal Engineering*, 51(1):781–786, 2013. ISSN 1359-4311. doi: https://doi.org/10.1016/j.applthermaleng.2012.10.033. URL `https://www.sciencedirect.com/science/article/pii/S1359431112006898`.

[10] Francesco Casella, Tiemo Mathijssen, Piero Colonna, and Jos van Buijtenen. Dynamic Modeling of Organic Rankine Cycle Power Systems. *Journal of Engineering for Gas Turbines and Power*, 135(4), 03 2013. ISSN 0742-4795. doi: 10.1115/1.4023120. URL `https://doi.org/10.1115/1.4023120`. 042310.

[11] G. Cavazzini, Francesco Giacomel, A. Benato, S. Bari, and G. Ardizzon. Influence of the fluid-dynamic properties of organic fluids on pump performance. *5th International Seminar on ORC Power Systems*, pages 1–9, 2020. URL `https://www.research.unipd.it/handle/11577/3309625#.YHg0ZFAiERM.mendeley`.

[12] Piero Colonna, Emiliano Casati, Carsten Trapp, Tiemo Mathijssen, Jaakko Larjola, Teemu Turunen-Saaresti, and Antti Uusitalo. Organic rankine cycle power systems: from the concept to current technology, applications, and an outlook to the future. *Journal of Engineering for Gas Turbines and Power*, 137(10), 2015.

[13] Laura Cozzi, Tim Gould, Stéphanie Bouckaert, Daniel Crow, Tae-Yoon Kim, Christophe McGlade, Paweł Olejarnik, Brent Wanner, and Daniel Wetzel. World energy outlook 2020 – analysis. Technical Report 1, International Energy Agency, 9, rue de la Fédération 75739 Paris Cedex, October 2020. URL `https://www.iea.org/reports/world-energy-outlook-2020`.

[14] F. D'Amico, P. Pallis, A.D. Leontaritis, S. Karellas, N.M. Kakalis, S. Rech, and A. Lazzaretto. Semi-empirical model of a multi-diaphragm pump in an organic rankine cycle (orc) experimental unit. *Energy*, 143:1056–1071, 2018. ISSN 0360-5442. doi: https://doi.org/10.1016/j.energy.2017.10.127. URL `https://www.sciencedirect.com/science/article/pii/S0360544217318327`.

[15] DGP Media b.v. Triogen uit goor begint aan wereldwijde opmars met groene technologie. `https://www.deondernemer.nl/actueel/triogen-uit-goor-begint-aan-wereldwijde-opmars-met-groene-technologie~494647`, 2016.

[16] Hessel Diepeveen. Redesigning the evaporator for the triogen orc (organic rankine cycle) for use in the containerized version of this orc (the so called triogen e-box). Technical Report 1, University of Twente, Drienerlolaan 5, 7522 NB Enschede, june 2018.

[17] Shoulong Dong, Boaz Habib, Bing Li, Wei Yu, and Brent Young. Organic rankine cycle systems design using a case-based reasoning approach. *Industrial & Engineering Chemistry Research*, 58(29):13198–13209, 2019. doi: 10.1021/acs.iecr.9b01150. URL `https://doi.org/10.1021/acs.iecr.9b01150`.

[18] Quirijn Eppinga. personal communication, 2021.

[19] Quirijn Eppinga, Stefano Ganassin, and Jos van Buijtenen. Application and operation of 40+ triogen orc plants. *Energy Procedia*, 129:684 – 691, 2017. ISSN 1876-6102. doi: https://doi.org/10.1016/j.egypro.2017.09.145. URL `http://www.sciencedirect.com/science/article/pii/S1876610217340079`. 4th International Seminar on ORC Power SystemsSeptember 13-15th 2017POLITECNICO DI MILANOBOVISA CAMPUSMILANO, ITALY.

[20] Edward Gravelle. 11 - high speed pumps. In Val S. Lobanoff and Robert R. Ross, editors, *Centrifugal Pumps (Second Edition)*, pages 173–205. Gulf Professional Publishing, Boston, second edition edition, 1992. ISBN 978-0-08-050085-0. doi: https://doi.org/10.1016/B978-0-08-050085-0.50014-X. URL `https://www.sciencedirect.com/science/article/pii/B978008050085050014X`.

[21] Johann Friedrich Gülich. *Centrifugal Pumps*. Springer Berlin Heidelberg, 2010. ISBN 9783642128240. doi: 10.1007/978-3-642-12824-0. URL `https://www-springer-com.tudelft.idm.oclc.org/gp/book/9783642128240`.

[22] John Harinck, Teemu Turunen-Saaresti, Piero Colonna, Stefano Rebay, and Jos van Buijtenen. Computational Study of a High-Expansion Ratio Radial Organic Rankine Cycle Turbine Stator. *Journal of Engineering for Gas Turbines and Power*, 132(5), 03 2010. ISSN 0742-4795. doi: 10.1115/1.3204505. URL `https://doi.org/10.1115/1.3204505`. 054501.

[23] John Harinck, David Pasquale, Rene Pecnik, Jos van Buijtenen, and Piero Colonna. Performance improvement of a radial organic rankine cycle turbine by means of automated computational fluid dynamic design. *Proceedings of the Institution of Mechanical Engineers, Part A: Journal of Power and Energy*, 227(6):637–645, 2013. doi: 10.1177/0957650913499565. URL `https://doi.org/10.1177/0957650913499565`.

[24] Robert Hołyst and Andrzej Poniewierski. *Thermodynamics for Chemists, Physicists and Engineers*. Springer Science+Business Media Dordrecht, 01 2012. ISBN 978-94-007-2998-8. doi: 10.1007/978-94-007-2999-5.

[25] Muhammad Imran, Fredrik Haglind, Muhammad Asim, and Jahan Zeb Alvi. Recent research trends in organic rankine cycle technology: A bibliometric approach. *Renewable and Sustainable Energy Reviews*, 81:552–562, 2018. ISSN 1364-0321. doi: https://doi.org/10.1016/j.rser.2017.08.028. URL `https://www.sciencedirect.com/science/article/pii/S1364032117311723`.

[26] Costante Mario Invernizzi. *Closed Power Cycles*. Springer-Verlag London, 2013. doi: 10.1007/978-1-4471-5140-1. URL `https://www-springer-com.tudelft.idm.oclc.org/gp/book/9781447151395`.

[27] Jacek Kalina, Mateusz Świerzewski, and Marcin Szega. Simulation based performance evaluation of biomass fired cogeneration plant with orc. *Energy Procedia*, 129:660–667, 2017. ISSN 1876-6102. doi: https://doi.org/10.1016/j.egypro.2017.09.137. URL `https://www.sciencedirect.com/science/article/pii/S1876610217339991`. 4th International Seminar on ORC Power SystemsSeptember 13-15th 2017POLITECNICO DI MILANOBOVISA CAMPUSMILANO, ITALY.

[28] Pijush K. Kundu. *Fluid mechanics*. Academic Press, London, sixth edition. edition, 2016 - 2016.

[29] Arnaud Landelle, Nicolas Tauveron, Philippe Haberschill, Rémi Revellin, and Stéphane Colasson. Organic rankine cycle design and performance comparison based on experimental database. *Applied Energy*, 204:1172–1187, 2017. ISSN 0306-2619. doi: https://doi.org/10.1016/j.apenergy.2017.04.012. URL https://www.sciencedirect.com/science/article/pii/S0306261917303884.

[30] Biao Lei, Jing-Fu Wang, Yu-Ting Wu, Chong-Fang Ma, Wei Wang, Lei Zhang, and Jing-Yan Li. Experimental study and theoretical analysis of a roto-jet pump in small scale organic rankine cycles. *Energy Conversion and Management*, 111:198–204, 2016. ISSN 0196-8904. doi: https://doi.org/10.1016/j.enconman.2015.12.062. URL https://www.sciencedirect.com/science/article/pii/S0196890415011711.

[31] Eric W. Lemmon and Roland Span. Short fundamental equations of state for 20 industrial fluids. *Journal of Chemical & Engineering Data*, 51(3):785–850, 2006. doi: 10.1021/je050186n. URL https://doi.org/10.1021/je050186n.

[32] Wenguang Li, Andrew Mckeown, and Zhibin Yu. Correction of cavitation with thermodynamic effect for a diaphragm pump in organic rankine cycle systems. *Energy Reports*, 6:2956–2972, 2020. ISSN 2352-4847. doi: https://doi.org/10.1016/j.egyr.2020.10.013. URL https://www.sciencedirect.com/science/article/pii/S2352484720313664.

[33] Bernard Looney. Statistical review of world energy. Technical Report 1, BP p.l.c., 1 St James's Square London SW1Y 4PD UK, June 2020. URL https://www.bp.com/content/dam/bp/business-sites/en/global/corporate/pdfs/energy-economics/statistical-review/bp-stats-review-2020-full-report.pdf.

[34] Fanxiao Meng, Hongguang Zhang, Fubin Yang, Xiaochen Hou, Biao Lei, Lei Zhang, Yuting Wu, Jingfu Wang, and Zhicheng Shi. Study of efficiency of a multistage centrifugal pump used in engine waste heat recovery application. *Applied Thermal Engineering*, 110:779–786, 2017. ISSN 1359-4311. doi: https://doi.org/10.1016/j.applthermaleng.2016.08.226. URL https://www.sciencedirect.com/science/article/pii/S1359431116315861.

[35] Andrea Meroni, Matthias Geiselhart, Wei Ba, and Fredrik Haglind. Preliminary design of radial-inflow turbines for organic rankine cycle power systems considering performance and manufacturability aspects. In Sotirios Karellas and Emmanuel Kakaras, editors, *Proceedings of the 5th International Seminar on ORC Power Systems*. National Technical University of Athens, 2019. 5th International Seminar on ORC Power Systems ; Conference date: 09-09-2019 Through 11-09-2019.

[36] Michael Moran and Howard Shapiro. *Fundamentals of engineering thermodynamics*, volume 18. Wiley, 01 1992. doi: 10.1080/03043799308928176.

[37] Ali Naseri, Stuart Norris, and Alison Subiantoro. Performance analysis of a revolving vane expander in an organic rankine cycle with hydrofluoroolefins (hfos) in place of r134a. In *5th International Seminar on ORC Power Systems*, 09 2019.

[38] Chunwee Ng, Ivan Tam, and Dawei Wu. Study of a waste heat driven organic rankine cycle using free piston linear expander for marine applications. In *5th International Seminar on ORC Power Systems*, 09 2019.

[39] Frans T.M. Nieuwstadt, Jerry Westerweel, and Bendiks J. Boersma. *Turbulence*. Springer International Publishing, 2016. doi: 10.1007/978-3-319-31599-7. URL https://doi.org/10.1007%2F978-3-319-31599-7.

[40] Gustavo J. Otero R, Stephan H.H.J. Smit, and Rene Pecnik. Three-dimensional unsteady stator-rotor interactions in high-expansion organic rankine cycle turbines. *Energy*, 217: 119339, 2021. ISSN 0360-5442. doi: https://doi.org/10.1016/j.energy.2020.119339. URL https://www.sciencedirect.com/science/article/pii/S0360544220324464.

[41] Byung-Sik Park, Muhammad Usman, Muhammad Imran, and Apostolos Pesyridis. Review of organic rankine cycle experimental data trends. *Energy Conversion and Management*, 173:679–691, 2018. ISSN 0196-8904. doi: https://doi.org/10.1016/j.enconman.2018.07.097. URL https://www.sciencedirect.com/science/article/pii/S0196890418308379.

[42] Mario Petrollese, Daniele Cocco, and Giorgio Cau. Small-scale csp plant coupled with an orc system for providing dispatchable power: the ottana solar facility. *Energy Procedia*, 129:708–715, 2017. ISSN 1876-6102. doi: https://doi.org/10.1016/j.egypro.2017.09.101. URL https://www.sciencedirect.com/science/article/pii/S1876610217339590. 4th International Seminar on ORC Power SystemsSeptember 13-15th 2017POLITECNICO DI MILANOBOVISA CAMPUSMILANO, ITALY.

[43] Roberto Pili, Alessandro Romagnoli, Hartmut Spliethoff, and Christoph Wieland. Techno-economic analysis of waste heat recovery with orc from fluctuating industrial sources. *Energy Procedia*, 129:503–510, 2017. ISSN 1876-6102. doi: https://doi.org/10.1016/j.egypro.2017.09.170. URL https://www.sciencedirect.com/science/article/pii/S1876610217340821. 4th International Seminar on ORC Power SystemsSeptember 13-15th 2017POLITECNICO DI MILANOBOVISA CAMPUSMILANO, ITALY.

[44] Roberto Pili, Nikolaos Siamisiis, Roberto Agromayor, Lars Nord, Christoph Wieland, and Spliethoff Hartmut. Efficiency correlations for off-design performance prediction of orc axial-flow turbines. In *5th International Seminar on ORC Power Systems*, 09 2019.

[45] Roberta Quadrelli, Francesco Mattion, Pouya Taghavi-Moharamli, and Faidon Papadimoulis. Co2 emissions from fuel combustion: Overview. Technical Report 1, Energy Data Centre, 9, rue de la Fédération 75739 Paris Cedex, July 2020. URL https://webstore.iea.org/download/direct/4036?fileName=CO2_Emissions_from_Fuel_Combustion_Overview_2020_edition.pdf.

[46] E.S. Richardson. Thermodynamic performance of new thermofluidic feed pumps for organic rankine cycle applications. *Applied Energy*, 161:75–84, 2016. ISSN 0306-2619. doi: https://doi.org/10.1016/j.apenergy.2015.10.004. URL https://www.sciencedirect.com/science/article/pii/S0306261915012313.

[47] Jelmer Rijpkema, Fredrik Ekström, Karin Munch, and Sven Andersson. Experimental results of a waste heat recovery system with ethanol using exhaust gases of a light-duty engine. In *5th International Seminar on ORC Power Systems*, 09 2019.

[48] Tryfon C. Roumpedakis, George Loumpardis, Evropi Monokrousou, Konstantinos Braimakis, Antonios Charalampidis, and Sotirios Karellas. Exergetic and economic analysis of a solar driven small scale orc. *Renewable Energy*, 157:1008–1024, 2020. ISSN 0960-1481. doi: https://doi.org/10.1016/j.renene.2020.05.016. URL `https://www.sciencedirect.com/science/article/pii/S096014812030714X`.

[49] Aldo Serafino, Benoit Obert, Léa Vergé, and Paola Cinnella. Robust optimization of an organic rankine cycle for geothermal application. *Renewable Energy*, 161:1120–1129, 2020. ISSN 0960-1481. doi: https://doi.org/10.1016/j.renene.2020.07.052. URL `https://www.sciencedirect.com/science/article/pii/S0960148120311289`.

[50] Stephan H.H.J. Smit, Quirijn Eppinga, Gustavo J. Otero, and Rene Pecnik. Optimization of a high expansion orc turbine using a genetic algorithm. In *Proceedings of the 5th International Seminar on ORC Power Systems*. Technical University Delft, 2019. 5th International Seminar on ORC Power Systems ; Conference date: 09-09-2019 Through 11-09-2019.

[51] Lorenzo Talluri, Olivier Dumont, Giampaolo Manfrida, Vincent Lemort, and Daniele Fiaschi. Geometry definition and performance assessment of tesla turbines for orc. *Energy*, 211:118570, 2020. ISSN 0360-5442. doi: https://doi.org/10.1016/j.energy.2020.118570. URL `https://www.sciencedirect.com/science/article/pii/S0360544220316789`.

[52] Thomas Tartière and Marco Astolfi. A world overview of the organic rankine cycle market. *Energy Procedia*, 129:2–9, 2017. ISSN 1876-6102. doi: https://doi.org/10.1016/j.egypro.2017.09.159. URL `https://www.sciencedirect.com/science/article/pii/S1876610217340286`. 4th International Seminar on ORC Power SystemsSeptember 13-15th 2017POLITECNICO DI MILANOBOVISA CAMPUSMILANO, ITALY.

[53] Jiyuan Tu, Guan-Heng Yeoh, and Chaoqun Liu. Chapter 6 - practical guidelines for cfd simulation and analysis. In Jiyuan Tu, Guan-Heng Yeoh, and Chaoqun Liu, editors, *Computational Fluid Dynamics (Second Edition)*, pages 219–273. Butterworth-Heinemann, second edition edition, 2013. ISBN 978-0-08-098243-4. doi: https://doi.org/10.1016/B978-0-08-098243-4.00006-8. URL `https://www.sciencedirect.com/science/article/pii/B9780080982434000068`.

[54] P. Valdimarsson. 10 - radial inflow turbines for organic rankine cycle systems. In Ennio Macchi and Marco Astolfi, editors, *Organic Rankine Cycle (ORC) Power Systems*, pages 321–334. Woodhead Publishing, 2017. ISBN 978-0-08-100510-1. doi: https://doi.org/10.1016/B978-0-08-100510-1.00010-7. URL `https://www.sciencedirect.com/science/article/pii/B9780081005101000107`.

[55] Jos P. van Buijtenen and Stefano Ganassin. Small scale solid biomass fuelled orc plants for combined heat and power. *Proceedings of the 3rd International Seminar on ORC Power Systems, Brussels, Belgium*, 3(59):1081–1089, 2015. URL `http://asme-orc2015.fyper.com/online/proceedings/documents/59.pdf`.

[56] L.M. Vonk. Working fluid selection for a diesel engine waste heat recovery orc module. Technical Report 1, Delft University of Technology, Mekelweg 2, 2628 CD Delft, June 2018. URL `https://repository.tudelft.nl/islandora/object/uuid:a391c469-e74e-4cb2-a329-ce8fbf79e339/datastream/OBJ/download`.

[57] C Vuik, PCW van Beek, FJ Vermolen, and JJIM van Kan. *Numerical Methods for Ordinary Differential Equations*. VSSD, 2007. ISBN 90-6562-156-3.

[58] Xin Wang, Yong-qiang Feng, Tzu-Chen Hung, Zhi-xia He, Chih-Hung Lin, and Muhammad Sultan. Investigating the system behaviors of a 10 kw organic rankine cycle (orc) prototype using plunger pump and centrifugal pump. *Energies*, 13(5), 2020. ISSN 1996-1073. doi: 10.3390/en13051141. URL `https://www.mdpi.com/1996-1073/13/5/1141`.

[59] Xuan Wang, Gequn Shu, Hua Tian, Wei Feng, Peng Liu, and Xiaoya Li. Effect factors of part-load performance for various organic rankine cycles using in engine waste heat recovery. *Energy Conversion and Management*, 174:504–515, 2018. ISSN 0196-8904. doi: https://doi.org/10.1016/j.enconman.2018.08.024. URL `https://www.sciencedirect.com/science/article/pii/S0196890418308720`.

[60] Andreas P. Weiß, Tobias Popp, Jonas Müller, Josef Hauer, Dieter Brüggemann, and Markus Preißinger. Experimental characterization and comparison of an axial and a cantilever micro-turbine for small-scale organic rankine cycle. *Applied Thermal Engineering*, 140:235–244, 2018. ISSN 1359-4311. doi: https://doi.org/10.1016/j.applthermaleng.2018.05.033. URL `https://www.sciencedirect.com/science/article/pii/S1359431118302035`.

[61] Zhe Wu, Zhiwei Yuan, Long Chen, and Jianzhao Li. Operating characteristics of working fluid pump in a 315 kw organic rankine cycle system. In *5th International Seminar on ORC Power Systems*, 09 2019.

[62] Weicong Xu, Jianyuan Zhang, Li Zhao, Shuai Deng, and Ying Zhang. Novel experimental research on the compression process in organic rankine cycle (orc). *Energy Conversion and Management*, 137:1–11, 2017. ISSN 0196-8904. doi: https://doi.org/10.1016/j.enconman.2017.01.025. URL `https://www.sciencedirect.com/science/article/pii/S0196890417300249`.

[63] Yuxin Yang, Hongguang Zhang, Yonghong Xu, Rui Zhao, Xiaochen Hou, and Yi Liu. Experimental study and performance analysis of a hydraulic diaphragm metering pump used in organic rankine cycle system. *Applied Thermal Engineering*, 132:605–612, 2018. ISSN 1359-4311. doi: https://doi.org/10.1016/j.applthermaleng.2018.01.001. URL `https://www.sciencedirect.com/science/article/pii/S1359431117358945`.

[64] Yuxin Yang, Hongguang Zhang, Guohong Tian, Yonghong Xu, Chongyao Wang, and Jianbing Gao. Performance analysis of a multistage centrifugal pump used in an organic rankine cycle (orc) system under various condensation conditions. *Journal of Thermal Science*, 28(4):621–634, 2019. doi: 10.1007/s11630-019-1069-9. URL `https://doi.org/10.1007/s11630-019-1069-9`.

[65] Mateusz Świerzewski and Jacek Kalina. Optimisation of biomass-fired cogeneration plants using orc technology. *Renewable Energy*, 159:195–214, 2020. ISSN 0960-1481. doi: https://doi.org/10.1016/j.renene.2020.05.155. URL `https://www.sciencedirect.com/science/article/pii/S0960148120308600`.